National Technical University of Athens
Department of Naval Architecture and Marine Engineering
Laboratory of Ship and Marine Hydrodynamics

Diploma Thesis

Numerical modelling of regular and irregular breaking waves using a coupled artificial compressibility method

---

Athanasios Dermatis

Thesis Supervisor: Assistant Professor G. Papadakis
Committee Member: Professor K. Belibassakis
Committee Member: Professor G. Grigoropoulos

February 26, 2022

Abstract

This thesis aims at investigating wave breaking using *MaPFlow*, a RANS numerical model coupled with an artificial compressibility method. To this end, several turbulence modelling approaches are used and evaluated for their ability to capture the turbulent regime of breaking waves. The model is validated for a spilling and a plunging wave over a sloping bottom, against the experimental results of Ting & Kirby (1994). For all simulations, the numerical wave tank concept is considered, the parameters of which are thoroughly analyzed at the beginning of the thesis, through the simple test case of a steep regular wave propagating over a flat bottom.

Moreover, a framework for the generation and propagation of irregular waves is developed by employing the Airy Wave theory, and is validated using *MaPFlow*. Following, this model is implemented to investigate the spectral evolution of irregular waves over a breaker bar and the results are compared with the experimental work of Beji & Battjes (1993). Finally, the Free Surface Reconstruction Algorithm (Grilli et al., 2011) is used in order to reproduce the incident wave pattern of the experiment of Adytia (2018) and examine the wave transformation over the same bathymetry.

Περίληψη

Η παρούσα διπλωματική εργασία αποσκοπεί στην διερεύνηση των θραυόμενων κυματισμών χρησιμοποιώντας το *MaPFlow*, έναν επιλύτη των RANS, συζευγμένο με τη μέθοδο της ψευδοσυμπιεστότητας. Σε αυτό το πλαίσιο, χρησιμοποιήθηκαν ορισμένες προσεγγίσεις για την μοντελοποίηση της τύρβης και αξιολογήθηκαν βάσει του βαθμού, στον οποίο είναι κατάλληλες να αποδώσουν το τυρβώδες καθεστώς της θραύσης των κυματισμών. Το αριθμητικό μοντέλο επικυρώθηκε για ένα κυλιούμενο και ένα καταδυόμενο μονοχρωματικό κύμα σε βαθυμετρία με πυθμένα σταθερής κλίσης, συγκριτικά με τα πειραματικά αποτελέσματα των Ting & Kirby (1994). Για όλες τις προσομοιώσεις, αξιοποιήθηκε η τεχνική της αριθμητικής κυματικής δεξαμενής, οι παράμετροι της οποίας αναλύονται διεξοδικά στο πρώτο κεφάλαιο αποτελεσμάτων της διπλωματικής εργασίας, μέσω της μελέτης ενός απότομου κανονικού κυματισμού που διαδίδεται άνωθεν επίπεδου πυθμένα.

Επιπλέον, αναπτύχθηκε το γενικό πλαίσιο για την παραγωγή και διάδοση πολυχρωματικών κυματισμών, με χρήση της κυματικής θεωρίας του Airy και επικυρώθηκε με τον επιλύτη *MaPFlow*. Ακολούθως, το συγκεκριμένο μοντέλο αξιοποιήθηκε για την διερεύνηση της φασματικής εξέλιξης μη-κανονικών κυματισμών κατά τη διάδοση τους άνωθεν πλάκας θραύσης κυμάτων και τα αποτελέσματα υποβλήθηκαν σε σύγκριση με την πειραματική εργασία των Beji & Battjes (1993). Τέλος, ο Αλγόριθμος Ανακατασκευής της Ελεύθερης Επιφάνειας (Grilli et al., 2011) χρησιμοποιήθηκε για την αναπαραγωγή της αλληλουχίας κυματισμών του πειράματος του Adytia (2018) και για την εξέταση της μεταβολής των κυματισμών στην συγκεκριμένη βαθυμετρία.

Aknowledgements

This thesis marks the end of my studies at the School of Naval Architecture and Marine Engineering and I would like to give credit to several people for their contribution towards its completion.

First of all, I would like to sincerely thank my supervisor, Professor G. Papadakis, for his guidance throughout the past year and for our cooperation, which was very beneficial for me and ignited my interest for research. I also owe special thanks to PhD candidate Dimitris Ntouras for his valuable comments, as well as for the insight he provided me into the field of CFD.

Following, I would like to thank Kostas and Giorgos, with whom we shared the same office and had insightful and endless discussions regarding our theses subjects. Special mention also goes to Myrsini, Stelios, Fotis, Kostas and Christina for their support throughout all the years of our studies in NTUA, as well as to Panos, Dimitris, Giannis, Loukas and Antigoni that accompany me during the last years of my life and whose indirect support and encouragement is priceless. Finally, I would like to deeply thank my family for supporting my every decision and providing me everything I needed to reach this point.

Contents

Chapter 1

Introduction

1.1 Background and State-of-the-Art

A distinguishing feature of marine hydrodynamics in comparison with other fields of fluid mechanics is the importance of surface gravity waves and their effects on fixed or floating offshore structures. Another particularly interesting aspect is the waves generated by surface piercing bodies in otherwise calm water. Detailed prediction of their characteristics is of crucial importance, since it allows a more accurate estimation of the wave loads, resistance, as well as the dynamic response of marine structures. All the aforementioned phenomena and their dynamics become quite more interesting and complex when they occur in the coastal zone, where they are strongly influenced by the geometry of the seabed. In this region, wave phenomena such as refraction, diffraction and shoaling are present, as well as the non linear interaction between wave components, that results in a reallocation of the waves' energy in the frequency spectrum. Among these events, one of the most complex and challenging to analyze is the wave breaking and especially its effects and accurate prediction, when fluid-structure interaction is considered.

Experiments constitute a very important tool for the investigation of wave breaking and breaking forces, however the significant growth of Computational Fluid Dynamics (CFD) and the parallel decrease in computational costs in recent years, have rendered them a useful tool for that purpose. Reynolds-Averaged Navier Stokes equations, constitute a good numerical approach for the modelling of the wave transformation over sloping seabeds, since classical potential flow theory formulations disregard the influence of viscosity and turbulence production,which plays a vital role in the investigation of surfzone dynamics, thus require the coupling with semi-empirical viscosity models.

During the last couple of decades, significant research has been conducted about the investigation of wave breaking using RANS and several fundamental challenges have emerged in that context. In particular, Lin & Liu [1] simulated spilling breakers using a single-phase algebraic $k - \epsilon$ turbulence model and the VOF method. One of their major findings was the sensitivity of the simulated wave profile and the respective turbulent kinetic energy

for different turbulence modelling approaches and they were the first to address the issue of turbulence overestimation in the surfzone. Moreover, Bradford [2] used $k-\epsilon$ and Re-Normalization Group (RNG) $k-\epsilon$ models to simulate spilling and plunging waves and identified the limitations of VOF in capturing the overturning of a plunging breaker, which according to the author's opinion might also be due to the unphysically large dissipation of the turbulence models. Following, Mayer & Madsen [3] used an ad-hoc modification of the TKE production for $k-\omega$ model, by using the mean flow vorticity instead of the mean velocity gradient. Under this scope, the overproduction of TKE and the excessive wave damping in the potential flow pre-breaking regions was eliminated and the agreement with the experimental results was significantly ameliorated. More recently, Chella [4] has implemented the Level Set Method (LSM) with a $k-\omega$ turbulence model to investigate the wave breaking over a seabed. Brown et al. [5] conducted an evaluation of different RANS turbulence closure models and compared their accuracy and efficiency regarding the capturing of wave breaking and showed that the most suitable are the Nonlinear $k-\epsilon$, the $k-\omega$ SST and the Reynolds Stress Model. Furthermore, Devolder et al. [6] identified the issue of the inherent damping of non breaking waves in the vicinity of the free-surface and developed a Buoyancy Modified $k-\omega$ and $k-\omega$ SST model to address this issue. The essence of this approach is the transition to a laminar regime in the region where the wave propagates without deforming and the recovery of the turbulence model in the surf zone, where large horizontal density gradients are present. Although the results showed an improved agreement with experiments, the author highlighted that the problem of turbulent kinetic energy over-prediction remains unresolved. Larsen & Fuhrman [7] showed that all the turbulence models in literature were subject to irrepressible growth of the turbulent kinetic energy, as well as the eddy viscosity and thus were unconditionally unstable. Liu et al. [8] have implemented the modified VOF method with free-surface jump conditions to study wave breaking, in order to address the issue of spurious air velocities described by Vukcevic et al. [9].

An alternative approach to RANS of much higher computational costs and need for finer mesh resolutions, termed as Large Eddy Simulation (LES) has also been utilized for the investigation of breaking regular waves. To that end, the large-scale turbulent eddies are calculated directly, whereas the smaller in the energy cascade scale are subject to modelling. Hieu et al. [10], conducted a two-dimensional LES study for breaking waves, providing satisfactory results and found that the air entrainment and the corresponding surface tension plays a significant role in the wave energy dissipation. Moreover, a three-dimensional LES was carried out by Christensen [11], in which both spilling and plunging breakers were simulated and provided good results in the inner surfzone, however the capturing of the breaking point and height, as well as the undertow profiles showed deviation from the experimental results. In this study, the significance of the mesh resolution in this type of simulations was highlighted, since according to the author the aforementioned discrepancies were due to mesh refinement insufficiency.

All the above reviewed literature regards regular waves, whereas for irregular wave breaking investigation using RANS, there is very limited literature available, mostly by Aggarwal et al. [12, 13, 14]. In his work, a model for the irregular wave generation has been

developed and its ability to capture wave transformation, over varying bathymetries was widely tested, followed by the investigation of the fluid-structure interaction in that context. Moreover, Gatin et al. [15] developed a framework for simulation of irregular waves using a RANS model coupled with a Higher Order Spectral (HOS) method, which led to increased computational efficiency.

As a summary, the free-surface modelling approach as well as the employed turbulence closure model are the issues of the most significance regarding the analysis of wave breaking. Thus, the first motive of this study is the implementation of the novel artificial compressibility method for free-surface flows introduced by Ntouras & Papadakis [16] for the investigation of breaking waves. Furthermore, the limited research in the area of irregular breaking waves consituted a significant motive for the attempt to extend the study towards that direction.

1.2 Scope of this Study

- Study of regular wave propagation over an impermeable slope using *MaPFlow* and validation with experimental results.
- Evaluation of several different formulations of the $k-\omega$ SST model and the accompanying production limiters, available in literature that aim at addressing the issue of the turbulence overproduction in breaking wave simulations.
- Development of a framework for the efficient and accurate generation of irregular waves and validation of this model using *MaPFlow*.
- Study of the irregular wave propagation over a submerged bar using the developed model and validation with experimental results.
- Implementation of the Free Surface Reconstruction Algorithm for the investigation of irregular wave patterns, over varying bottom topographies and validation with experimental results.

1.3 Thesis Outline

In Chapter 1 the theoretical background of breaking waves is provided along with the purpose of the present study and the current trends in the use of RANS models for the analysis of wave breaking. Chapter 2 describes the governing equations and the methods implemented by *MaPFlow* for fully stating the problem under consideration. Chapter 3 is an introduction to the concept of the Numerical Wave Tank and the employed methods for wave generation and absorption. Chapter 4 contains a parametric study for the propagation of a steep regular wave over a flat bottom and aims providing an insight about the solver settings to be used for the investigation of wave breaking. In Chapter 5 the test case of breaking regular waves over a slope is considered and the various turbulence models are reviewed.

Following, Chapter 6 describes the development of the methodology for the generation of irregular waves and the validation with analytical data and Chapter 7 considers two test cases of irregular wave propagation over variable bathymetries. Finally, in Chapter 8 the final conclusions of the present work are drawn and some recommendations for future research are provided.

1.4 Breaking Waves

Wave breaking is a widely observed phenomenon in nearshore regions and of great significance for coastal and offshore engineering applications. Its essence is an instability of wave's motion and energy balance, which is recovered by the release of a portion of energy through the breaking process. In particular, when waves propagate from deep water shorewards, their motion is affected by the bathymetry changes, resulting in a reduction of their celerity and wavelength. As a result the velocity field throughout the wave profile becomes inhomogeneous, since the particle velocity at the wave crest, as well as the wave height are generally increased. Eventually, the wave front propagates much faster than the fluid beneath and the wave becomes gradually steeper until breaking [4]. Hence, breaking of waves is an energy dissipation mechanism involving the transformation of their energy, derived from the motion and displacement of fluid particles, to turbulent energy and leading to abrupt deformations of the free surface [17]. It is noteworthy that waves are also prone to breaking in deep water due to hydrodynamic instabilities, however the present section concentrates on the case of breaking due to shoaling.

1.4.1 Breaker Classification

In the case of shoaling breaking waves, the initiation and evolution of the breaking process might differ based on the wave's steepness (H/λ) and the slope of the seabed. Four different types of breakers can be found in literature [18],[19], defined as:

- Spilling: In seabeds of soft slope, small scale turbulence is produced in front of the wave crest, which gradually covers the entire wave front, resulting in air being entrained and riding on this turbulent front.
- Plunging: Occurs for steeper slopes, where the wave becomes very asymmetric and skewed, while the breaking is more violent than the spilling wave, thus releasing more energy. In this type of breakers, the front eventually passes the point where the free surface is vertical and the crest curls over and drops on the neighbouring trough (overturning).
- Surging: In very steep slopes, the wave peaks up, as in the case of plunging breakers, but the fluid region above the trough propagates faster and the wave slides up the slope, with little or no turbulence production.

- Collapsing: This type of waves, lies between plunging and surging waves with the difference that they never fully break, but the wave front becomes steeper and eventually collapses.

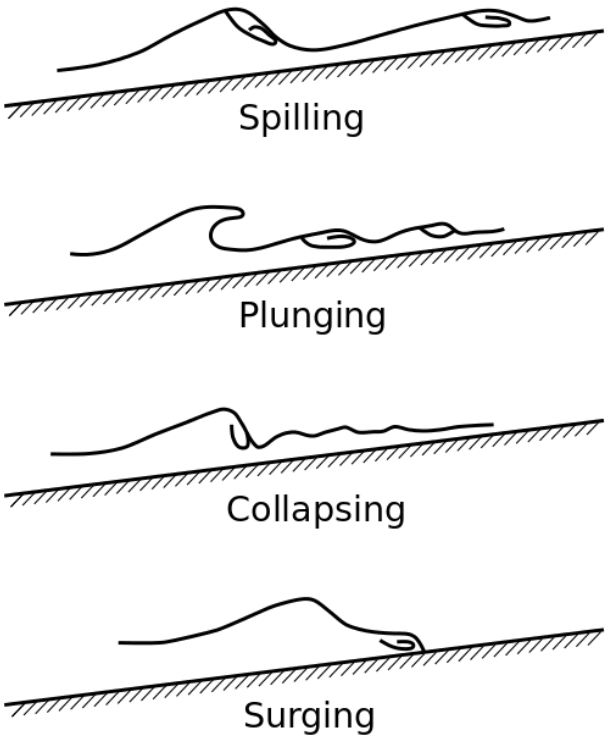

Figure 1.1: Types of breaking waves [20]

An illustration of these types of breakers is shown in Fig. 1.1. The surf-zone, denoting the turbulent region between the breaking onset and the shore is of limited length for the last two types of breakers. The breaking process in these cases, does not evolve entirely, thus the turbulence production is quite limited and occurs mostly as foam. A quantitative approach for classifying these breaker types is the surf similarity parameter or Iribarren number [21], defined as

$$\xi = \frac{m}{\sqrt{H_0/\lambda_0}} \tag{1.1}$$

where m is the seabed slope and H_0, λ_0 denote the incident wave height and length respectively. Battjes [22] suggests the following limits for each type: spilling at $\xi \leq 0.5$, plunging at $0.5 < \xi \leq 3.3$ and surging/collapsing at $\xi \geq 3.3$.

1.4.2 Breaking Criteria

Criteria of various types and nature have been developed in order to predict or identify the wave breaking process. One of the most common geometric criteria, provides that the free surface during breaking will tend to become vertical and the respective slope to become infinite. Another criterion that correlates breaking with the physical properties of the wave identifies the position of breaking as the position where the wave height has its maximum value, or more accurately where the ratio of the wave height to depth is maximum. This ratio has been extensively studied in literature and some of the values proposed are shown in Table 1.1. Moreover, a kinematic equivalent criterion states that the horizontal particle velocity of the wave crest will exceed the wave celerity, while from a dynamic aspect, the downward acceleration exceeds half of the gravitational acceleration [4].

$(H/d)_{max}$	Author
0.73	Boussinesq (1871)
0.78	McCowan (1894)
0.83	Gwyther (1900)
0.83	Davies (1952)
0.85	Fenton (1972)
0.8261	Longuet-Higgins and Fenton (1974)

Table 1.1: Suggested maximum wave height to depth ratio at breaking [17]

Chapter 2

MaPFlow Solver

For the purpose of the present study, the Eulerian solver *MaPFlow* [23], developed by the Laboratory of Ship and Marine Hydrodynamics of NTUA, was used. *MaPFlow* is a multiphase solver, which uses the Finite Volume method to solve the unsteady compressible and incompressible Reynolds-Averaged Navier Stokes equations on unstructured grids.

2.1 Governing Flow Equations

2.1.1 Conservation of Mass and Momentum

The fundamental laws of mechanics, when applied to fluid media, provide the conservation laws of the flow. Assuming an incompressible fluid, the conservation of mass and momentum are sufficient for the present approach and they can be expressed in differential vector form as

$$\nabla \vec{u} = 0 \tag{2.1}$$

$$\frac{\partial \vec{u}}{\partial t} + \vec{u}\nabla\vec{u} = -\frac{1}{\rho}\nabla p + \nabla\vec{\sigma} + \vec{F}_B \tag{2.2}$$

The former of these equations is also known as the Continuity Equation, while the latter is equivalent to Newton's Second Law of Motion for the fluid. In equations (2.1) and (2.2), ρ denotes the fluid density, $\vec{u}$ the velocity vector, p the pressure, $\vec{F}_B$ the source terms and body forces and $\vec{\sigma}$ the stress tensor.

2.1.2 Volume-of-Fluid (VOF) Method

Given that the flows under consideration are unsteady two-phase flows of two fully immiscible fluids, a framework for accounting for the free-surface is necessary. There are several ways through which the physique of the free-surface is introduced to RANS. In the present work, the VOF method [24] is adopted in order to reduce the problem to a single field computation (mono-fluid approach). Hence, the solution procedure requires the use of only single-phase equations, while the interface between the two segregated fluids is treated as a discontinuity of the density and as a transition of the field properties.

The basic principle of this method is the use of an indicator function to denote whether the region is of liquid or gas phase. This function is called the volume fraction and is defined below.

$$\alpha = \frac{\rho_m - \rho_a}{\rho_w - \rho_a} \tag{2.3}$$

where index ρ_w corresponds to the density of water, ρ_a to the density of air and ρ_m to the density of the cell under consideration. It is evident that the volume fraction takes the values 1 and 0 for water and air respectively, while at the free surface, it takes an interim value. In this area, which defines the vicinity of the free surface, the properties of the mixture fluid are redefined according to the volume fraction and follow

$$\rho_m = \alpha\rho_w + (1-\alpha)\rho_a \tag{2.4}$$

$$\mu_m = \alpha\mu_w + (1-\alpha)\mu_a \tag{2.5}$$

Thus, an additional equation is coupled with the conservation of mass and momentum, which is derived from the assumption that the free-surface is a material surface, hence the substantial derivative of the volume fraction will be equal to zero,

$$\frac{D\alpha}{Dt} = \frac{\partial\alpha}{\partial t} + \vec{u}\cdot\nabla\alpha = 0 \tag{2.6}$$

Interface Compression Technique

In the sections of this work that involve the study of wave breaking, a highly accurate depiction of the free-surface and its abrupt changes is necessary, thus a sharp interface is required. This can be provided by the following modification of the VOF equation [25]:

$$\frac{\partial\alpha}{\partial t} + \vec{u}\cdot\nabla\alpha + \vec{u}_r\cdot\nabla\alpha(1-\alpha) = 0 \tag{2.7}$$

where $\vec{u}_r$ is the reference velocity and can be found with multiple expressions in literature.

In *MaPFlow*, considering that the numerical solution involves steady step iterations, $\vec{u}_r$ is defined as an amendment of the expression provided by Vukcevic et al. [9]:

$$\vec{u}_r = c_a \vec{n}_\eta \frac{CFL\vec{d_f}}{\Delta t} \tag{2.8}$$

This additional term is activated only in the vicinity of the free surface where $\alpha(1-\alpha)$ is non-zero and prevents the excessive smearing of the interface, that occurs due to numerical diffusion. The parameter c_a is a constant that regulates the compression scale, $\vec{d_f}$ is the distance between two adjacent cell centers and $\vec{n}_\eta$ is a unit vector normal to the interface.

2.1.3 Artificial Compressibility Method

The RANS equations when applied to an incompressible flow as the present case, are inherently problematic. This is because the continuity and momentum equations are decoupled and a way to link them shall be considered. There are several approaches in literature that address this issue, known as pressure-correction methods, such as the SIMPLE [26] and PISO [27] algorithms. However, in this study an Artificial Compressibility Method is adopted, introduced initially by Chorin [28].

The basic principle of this approach is the implementation of an artificial relation between density and pressure during convergence, that resembles the case of a compressible flow. This resemblance, lies into the following relation, that corresponds to the definition of the speed of sound in a compressible fluid media

$$\frac{\partial p}{\partial \rho} = c^2 \tag{2.9}$$

Although, in the case of an incompressible fluid, this relation is defined as a pseudo-time derivative, corresponding to the numerical procedure until convergence and the sound speed c is substituted by a numerical parameter β that regulates this procedure

$$\left.\frac{\partial \rho}{\partial p}\right|_\tau = \frac{1}{\beta} \tag{2.10}$$

Hence, having that $\frac{\partial \rho}{\partial \tau} = \frac{\partial \rho}{\partial p}\frac{\partial p}{\partial \tau} = \frac{1}{\beta}\frac{\partial p}{\partial \tau}$ an augmented mass equation is formed in a way that

$$\frac{1}{\beta}\frac{\partial p}{\partial \tau} + \rho \nabla \vec{u} = 0 \tag{2.11}$$

Once the numerical solution has converged, the first term equals to zero and the initial equation is recovered for the physical time-stepping.

2.1.4 Derivation of the Conservative Form

Prior to the discretization of the governing equations, the derivation of the conservative (compressible) form is presented. For the mass conservation equation, having under consideration the AC fictitious derivative term it follows

$$\frac{\partial \rho}{\partial t} + \frac{\partial \rho}{\partial \tau} + \nabla \rho \vec{u} = 0 \tag{2.12}$$

Expansion of this equation's terms and omitting the density time derivative and the density gradient as zeros, provides

$$\frac{\partial \rho}{\partial \tau} + \rho \nabla \vec{u} = \frac{1}{\beta}\frac{\partial p}{\partial \tau} + \rho \nabla \vec{u} = 0 \tag{2.13}$$

Under this scope, a fictitious time derivative is also added to the conservative form of the momentum equation providing

$$\frac{\partial (\rho \vec{u})}{\partial t} + \frac{\partial (\rho \vec{u})}{\partial \tau} + \nabla (\rho \vec{u} \cdot \vec{u}) = -\nabla p + \nabla \vec{\sigma} + \vec{F}_B \tag{2.14}$$

Assuming that the density is not constant in time and in the vicinity of the free surface in the case of a two-phase flow, the temporal term may be expanded as follows

$$\begin{aligned} \frac{\partial (\rho \vec{u})}{\partial t} &= \rho \frac{\partial \vec{u}}{\partial t} + \vec{u}\frac{\partial \rho}{\partial t} \\ \Rightarrow \frac{\partial (\rho \vec{u})}{\partial t} &= \rho \frac{\partial \vec{u}}{\partial t} + \vec{u}\frac{\partial}{\partial t}(\alpha \Delta \rho + \rho_\alpha) \\ \Rightarrow \frac{\partial (\rho \vec{u})}{\partial t} &= \rho \frac{\partial \vec{u}}{\partial t} + \vec{u}\Delta \rho \frac{\partial \alpha}{\partial t} \end{aligned} \tag{2.15}$$

where $\Delta\rho$ is the difference of densities between the two fluids.

In a similar way the pseudo-time derivative will follow

$$\frac{\partial (\rho \vec{u})}{\partial \tau} = \rho \frac{\partial \vec{u}}{\partial \tau} + \vec{u}\Delta \rho \frac{\partial \alpha}{\partial \tau} \tag{2.16}$$

Finally, the transport equation for the volume fraction will be

$$\frac{\partial \alpha}{\partial t} + \frac{\partial \alpha}{\partial \tau} + \frac{\alpha}{\rho_m \beta}\frac{\partial p}{\partial \tau} + \nabla (\vec{u}\alpha) = 0 \tag{2.17}$$

The aforementioned equations (2.13),(2.14) and (2.17), constitute a fully coupled system

of non-linear equations, able to describe unsteady two-phase flows. By considering a reference volume Ω and integrating the field quantities over it, this system can be written in the following matrix form

$$\Gamma \int_{\Omega} \frac{\partial \vec{Q}}{\partial \tau} d\Omega + \Gamma_e \int_{\Omega} \frac{\partial \vec{Q}}{\partial t} d\Omega = - \oint_{\partial\Omega} (\vec{F}_c - \vec{F}_v) dS + \int_{\Omega} \vec{S}_q d\Omega \tag{2.18}$$

where, Γ is the preconditioner of Kunz [29], used in order to counteract the problem of stiff matrices that occur when high density ratios appear in the eigenvalues of the system. Vector $\vec{Q}$ is the matrix of primitive variables, whereas $\vec{U}$ are the respective conservative variables. It is worth noticing that the unsteady system of equations is expressed for the conservative variables $\vec{U}$ at each physical timestep, but at each fictitious timestep, a pseudo-steady state problem is solved for the primitive equations $\vec{Q}$. The transformation from the latter to the former is achieved through the Jacobian matrix $\Gamma_e = \frac{\partial \vec{U}}{\partial \vec{Q}}$.

$$\vec{U} = \begin{bmatrix} 0 & \rho\vec{u} & \alpha_l \end{bmatrix}^T \qquad \vec{Q} = \begin{bmatrix} p & \vec{u} & \alpha_l \end{bmatrix}^T \tag{2.19}$$

$$\Gamma = \begin{bmatrix} \frac{1}{\beta\rho_m} & 0 & 0 \\ 0 & \rho_m I & \vec{u}\Delta\rho \\ \frac{\alpha_l}{\beta\rho_m} & 0 & 1 \end{bmatrix} \qquad \Gamma_e = \begin{bmatrix} 0 & 0 & 0 \\ 0 & \rho_m I & \vec{u}\Delta\rho \\ 0 & 0 & 1 \end{bmatrix} \tag{2.20}$$

Moreover, $\vec{F}_c$ and $\vec{F}_v$ denote the inviscid and viscous flluxes respectively, described as

$$\vec{F}_c = \begin{bmatrix} V_n \\ \rho_m u \Delta V + p n_x \\ \rho_m v \Delta V + p n_y \\ \rho_m w \Delta V + p n_z \\ \alpha_l V_n \end{bmatrix} \qquad \vec{F}_v = \begin{bmatrix} 0 \\ \tau_{xx} n_x + \tau_{xy} n_y + \tau_{xz} n_z \\ \tau_{yx} n_x + \tau_{yy} n_y + \tau_{yz} n_z \\ \tau_{zx} n_x + \tau_{zy} n_y + \tau_{zz} n_z \\ 0 \end{bmatrix} \tag{2.21}$$

where $V_n = \vec{u} \cdot \vec{n}$, $V_g = \vec{u}_{vol} \cdot \vec{n}$ and $\Delta V = V_n - V_g$. The velocity $\vec{u}_{vol}$ corresponds to the movement of the control volume and $\vec{n}$ denotes the surface normal of the control volume. It is worth noticing that if the mesh is static, $\vec{u}_{vol} = 0$ and $\Delta V = V_n$.

The viscous stresses τ_{ij}, according to Boussinesq' hypothesis follow

$$\tau_{ij} = (\mu_m + \mu_t)(\frac{\partial u_i}{\partial x_j} + \frac{\partial u_j}{\partial x_i}) - \frac{2}{3}\rho\delta_{ij}k \tag{2.22}$$

where μ_t is the turbulent dynamic viscosity, k is the turbulent kinetic energy and δ_{ij} is the Kronecker delta.

2.2 Spatial Discretization

2.2.1 Finite Volume Scheme

MaPFlow utilizes the Finite Volume Method for the spatial discretization of the equations mentioned above. In the context of this approach the mesh is, divided into cells of arbitrary shape, whose volume Ω_i is bounded by their edges, while the center of their volume coincides with the center of the cells. As discussed later, the field quantities are stored at the cell centers and a suitable interpolation method to the cell faces is required.

Thus, the primitive variables for a control volume Ω_i will be integrated to

$$\overrightarrow{\overline{Q}} = \frac{1}{\Omega_i} \int_{\Omega_i} \vec{Q}(\vec{x}; t) d\Omega \tag{2.23}$$

By gathering the right-hand side terms of Eq. (2.18) in a residual, and following the formulation above considering finite volumes, it will follow that

$$\Gamma_e \frac{\partial(\overrightarrow{\overline{Q}}\Omega)}{\partial t} + \Gamma \frac{\partial(\overrightarrow{\overline{Q}}\Omega)}{\partial \tau} = -\vec{R}_\Omega \tag{2.24}$$

where,

$$\vec{R}_\Omega = \oint_{\partial\Omega_i(t)} (\vec{F}_c - \vec{F}_v) dS - \int_{\Omega_i(t)} \vec{S}_q d\Omega \tag{2.25}$$

Assuming that the surface integral of the residual $\vec{R}_\Omega$ does not vary across different edges of each cell, it can be approximated as a sum of the fluxes evaluated at each face midpoint. In addition, the volume integral of the source term is assumed to be constant throughout each elemental volume. Thus, if N_f is the total number of faces of the corresponding control volume it can be expressed as

$$\vec{R}_{\Omega_i} = \sum_j^{N_f} (\vec{F}_c - \vec{F}_v) dS_i - \overrightarrow{\overline{S}}_q \Omega_i \tag{2.26}$$

For simplification purposes, the averaging operator "—" will be disregarded from now on.

2.2.2 Variable Reconstruction

As briefly discussed in the previous section, *MaPFlow* is a cell centered code, meaning that all field variable values are computed for the center of each element. However, as

shown in equation (2.26), these information need to be defined at the cell faces, in order to calculate the right-hand side residual of equation (2.18). The process of transferring via extrapolation the cell centered value of these variables at the respective edges is called variable reconstruction and there are several suitable schemes for this purpose.

Considering two adjacent cells i, j with control volumes Ω_i, Ω_j respectively, that are in contact over face f, as shown in Fig.2.1. The extrapolated value of a vector $\vec{\phi}_i$ on the left side of f is denoted by $\vec{\phi}_L$, while $\vec{\phi}_R$ is the value on the right side of f, coming from $\vec{\phi}_j$.

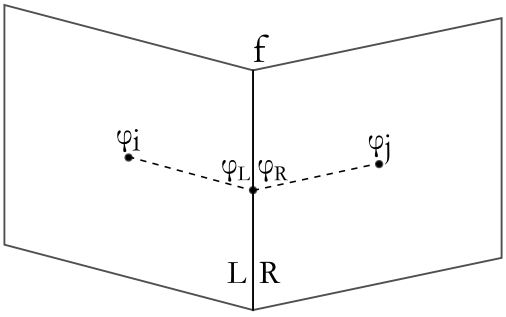

Figure 2.1: Configuration of variable reconstruction

Regarding the various reconstruction schemes available in literature, a careful selection is required for each variable depending on its variations throughout the mesh. In particular, the Piecewise Linear Reconstruction (PLR) can be implemented for the velocity, which is continuous everywhere in the field, as well as for the pressure in one phase flows. In two phase cases, both the pressure gradient and volume fraction present a strong discontinuity in the vicinity of the free surface, due to the density jump and this transitional area must be taken into account appropriately. Regarding the pressure field, a condition of $\left[\frac{\nabla p}{\rho}\right] = 0$ is required, which is treated by the density-based interpolation scheme of Qeuetey et al. [30] near the free-surface. Proceeding with α, which is discontinuous by its definition, special treatment should also be given, in order to preserve the associated interface sharpness and hinder excessive smearing due to numerical diffusion. For this purpose, *MaPFlow* uses the PLR scheme for the volume fraction away from the free surface, while at this region uses one of the more detailed interface capturing schemes presented below.

Piecewise Linear Reconstruction (PLR)

The PLR scheme, assumes that the flow variables are linearly distributed over the control volume, thus

$$\begin{aligned} \vec{\phi}_L &= \vec{\phi}_i + \Psi_i \nabla(\vec{\phi}_i \cdot \vec{r}_i) \\ \vec{\phi}_R &= \vec{\phi}_j + \Psi_j \nabla(\vec{\phi}_j \cdot \vec{r}_j) \end{aligned} \tag{2.27}$$

where Ψ denotes an appropriate limiter in the case of undesired very large gradients. In the present work, the gradients were defined using the Least Squares Method [31] and the

Venkatakrishnan limiter [32] was employed only in the case of the volume fraction. For all the other field variables it was omitted, due to the fact that in incompressible flows, discontinuities are not acceptable.

Interface Capturing Schemes

The basic principle of these schemes is the use of a blending function between a Compressive and a High-Resolution advection scheme, that depends on the angle between the flow direction and the grid lines (Eq. 2.28). This angle may be determined using the gradient of ϕ, the unit vector of which corresponds to the normal vector to the interface, as well as the grid orientation at the face under consideration. Under this scope, both the excessive smearing of the interface, as well as its over-compression, that leads to the suppression of curvature are prevented.

$$\theta_f = arccos\left|\frac{\nabla\phi_f \cdot \vec{n}_{ij}}{\|\nabla\phi_f\|\|\vec{n}_{ij}\|}\right| \tag{2.28}$$

Moreover, a common feature of all these schemes is the use of the Normalized Variable Diagram (NVD) [33], according to which, a normalized variable $\tilde{\phi}$ is introduced in the neighbourhood of a face f, defined as,

$$\tilde{\phi} = \frac{\phi - \phi_U}{\phi_D - \phi_U} \tag{2.29}$$

where U and D denote upwind and downwind respectively and are selected according to the flow direction.

Thus, the general approach is that the normalized value of ϕ at the desired face will be obtained using a blending function $f(\theta_f)$, switching between the aforementioned two extreme schemes as

$$\tilde{\phi}_f = f(\theta_f)\tilde{\phi}_{f(comp)} + \big[1 - f(\theta_f)\big]\tilde{\phi}_{f(HR)} \tag{2.30}$$

Under this approach, each of the examined schemes will differ in terms of the blending function and selected extreme schemes. Several interface capturing reconstruction schemes that were implemented and evaluated in the present work are presented below.

High Resolution Interface Capturing Scheme (HRIC)

The subject scheme was first introduced by Muzaferija [34] and is established on a blending of the Bounded Downwind (BD) and Upwind Differencing (UD) schemes, with $f(\theta_f) = \sqrt{cos(\theta_f)}$ as a blending function. Thus, the terminal expression for the reconstructed normalized variable will follow

$$\tilde{\phi}_{f(HRIC)} = \sqrt{cos(\theta_f)}\tilde{\phi}_{f(BD)} + \left[1 - \sqrt{cos(\theta_f)}\right]\tilde{\phi}_{f(UD)} \tag{2.31}$$

where,

$$\phi_{f(BD)} = \begin{cases} 2\phi_C & 0 < \phi_C \geq 0.5 \\ 1 & 0.5 < \phi_C \geq 1 \\ \phi_C & \text{otherwise} \end{cases} \qquad \tilde{\phi}_{f(UD)} = \tilde{\phi}_C \tag{2.32}$$

Moreover, the scheme is modified with respect to the local CFL number of the edge, which is defined as

$$CFL_f = \frac{\vec{u}_f \cdot \vec{S}_f \Delta t}{V_f} \tag{2.33}$$

In particular, for CFL values below 0.3 the scheme is not subject to any modifications, for values above 0.7, the upwind scheme is used, while for the interim values, it is blended with the upwind scheme as follows

$$\tilde{\phi}_{f(HRIC)} = \tilde{\phi}_f + \left[\tilde{\phi}_f - \tilde{\phi}_{f(UD)}\right] \frac{0.7 - CFL_f}{0.7 - 0.3} \tag{2.34}$$

Compressive Interface Capturing Scheme for Arbitrary Meshes (CICSAM)

The CICSAM scheme was introduced by Ubbink [35] and is constructed under the same philosophy, blending between the HYPER-C scheme [36] and the ULTIMATE-QUICKEST (UQ) scheme [37], which follow

$$\tilde{\phi}_{f(HYPER-C)} = \begin{cases} \min(1, \frac{\tilde{\phi}_C}{CFL}) & 0 < \phi_C \geq 1 \\ \tilde{\phi}_C & \text{otherwise} \end{cases}$$

$$\tilde{\phi}_{f(UQ)} = (CFL)\tilde{\phi}_{f(UD)} + (1 - CFL)\tilde{\phi}_{f(QUICK)} \tag{2.35}$$

where,

$$\tilde{\phi}_{f(QUICK)} = \frac{3}{8} + \frac{3}{4}\tilde{\phi}_C \qquad \tilde{\phi}_{f(UD)} = \tilde{\phi}_C \tag{2.36}$$

Thus, the formulation of the CICSAM scheme will be

$$\tilde{\phi}_{f(CICSAM)} = f(\theta_f)\tilde{\phi}_{f(HYPER-C)} + \left[1 - f(\theta_f)\right]\tilde{\phi}_{f(UQ)} \tag{2.37}$$

where,

$$f(\theta_f) = \min\left(\frac{cos(2\theta_f)+1}{2}, 1\right) \tag{2.38}$$

Switching Technique for Advection and Capturing of Surface (STACS)

In the context of this reconstruction scheme, developed by Darwish & Moukalled [38], the selected compressive scheme is SUPERBEE [36], a bounded form of the downwind scheme and the high resolution scheme is STOIC [39]. The blending between them is regulated by $f(\theta_f) = cos^4(\theta_f)$, while these schemes are defined as

$$\tilde{\phi}_{f(SUPERBEE)} = \begin{cases} \tilde{\phi}_C & \tilde{\phi}_C \leq 0 \\ 1 & 0 < \tilde{\phi}_C < 1 \\ \tilde{\phi}_C & 1 \leq \tilde{\phi}_C \end{cases} \qquad \tilde{\phi}_{f(STOIC)} = \begin{cases} \tilde{\phi}_C & \tilde{\phi}_C \leq 0 \\ \frac{1}{2} + \frac{1}{2}\tilde{\phi}_C & 0 < \tilde{\phi}_C \leq \frac{1}{2} \\ \frac{3}{8} + \frac{3}{4}\tilde{\phi}_C & \frac{1}{2} \leq \tilde{\phi}_C \leq \frac{5}{6} \\ 1 & \frac{5}{6} < \tilde{\phi}_C \leq 1 \end{cases} \tag{2.39}$$

Hence, the terminal expression for the STACS scheme shall be

$$\tilde{\phi}_{f(STACS)} = \tilde{\phi}_{f(SUPERBEE)} cos^4(\theta_f) + \tilde{\phi}_{f(STOIC)} \left[1 - cos^4(\theta_f)\right] \tag{2.40}$$

Blended Interface Capturing Scheme (BICS)

The BICS approach [40] is quite more complex than the previous, as the switching between compression and high resolution occurs in two stages. Firstly, the Inter-Gamma Discretization Scheme (IGDS) [41], an extension of the Gamma Discretization Scheme (GDS) [42] towards the downwind differencing (DDS) is regulated according to the CFL value. Then, the blending between this scheme and the GDS takes place considering a function $f(\theta_f) = \sqrt{\left|cos(\theta_f)\right|}$.

To begin with, the slope p of the linear part of the NVD diagram is defined as

$$p = \alpha_p p_{GDS} + (1 - \alpha_p) p_{IGDS} \tag{2.41}$$

where,

$$\alpha_p = \begin{cases} 1 & CFL \leq 0.3 \\ \frac{CFL-0.3}{e^{(CFL-0.3)}-1} & CFL > 0.3 \end{cases} \tag{2.42}$$

$$p_{GDS} = 0.5 \qquad p_{IGDS} = 0$$

Moreover, a linear dependency of the slope p and the abscissa position β of the matching point is considered in a way that

$$\beta(p) = \alpha_0 + \alpha_1 p \tag{2.43}$$

with,

$$\alpha_1 = \frac{\beta_{GDS} - \beta_{IGDS}}{p_{GDS} - p_{IGDS}} \qquad \alpha_0 = \beta_{IGDS} - \alpha_1 p_{IGDS} \tag{2.44}$$

$$\beta_{GDS} = 0.1 \qquad \beta_{IGDS} = 0.5 \tag{2.45}$$

Hence, the formulation of the transitional scheme has a strong dependency on the NVD diagram and the CFL number and follows

$$\tilde{\phi}_{f*} = \begin{cases} \frac{1-p}{\beta^2}\tilde{\phi}_C^2 + (p + \frac{2-2p}{\beta}\tilde{\phi}_C) & 0 < \tilde{\phi}_C < \beta \\ p\tilde{\phi}_C + (1-p) & \beta \leq \tilde{\phi}_C < 1 \\ \tilde{\phi}_C & \text{otherwise} \end{cases} \tag{2.46}$$

The reconstructed value for the BICS scheme will thus be

$$\tilde{\phi}_{f(BICS)} = \tilde{\phi}_{f*}\sqrt{|cos(\theta_f)|} + \tilde{\phi}_{f(GDS)}\left[1 - \sqrt{|cos(\theta_f)|}\right] \tag{2.47}$$

Modified Gamma Discretization Scheme (MGDS)

The MGDS scheme [30] is quite different from the above, in terms of not using a blending function that depends on the angle between the flow direction and the interface. Instead, the blending occurs between the IGDS scheme and the upwind difference scheme as a function of the CFL number in a way that

$$\tilde{\phi}_f = \begin{cases} \tilde{\phi}_C + (\tilde{\phi}_{f(IGDS)} - \tilde{\phi}_C)\frac{0.7-CFL}{0.7-0.3} & 0.3 \leq CFL \leq 0.7 \\ \tilde{\phi}_C & \text{otherwise} \end{cases} \tag{2.48}$$

where,

$$\tilde{\phi}_{f(IGDS)} = \begin{cases} -2\tilde{\phi}_C^2 + 3\tilde{\phi}_C & 0 < \tilde{\phi}_C < 0.5 \\ 1 & 0.5 \leq \tilde{\phi}_C < 1 \\ \tilde{\phi}_C & \text{otherwise} \end{cases} \tag{2.49}$$

2.2.3 Convective Fluxes

Following the variable reconstruction on the cell faces, the extrapolation of two different values $\vec{Q}_R$ and $\vec{Q}_L$ on the same edge creates a discontinuity, an issue that has been addressed in literature as a Riemann problem. In order to overcome this, the approximate Riemann solver of Roe [43] is used, in combination with the preconditioning matrix Γ. The preconditioned Jacobian matrix that transforms the conservative variables to primitive will be

$$A_c = \frac{\partial \vec{F}_c}{\partial \vec{Q}} = \Gamma\Gamma^{-1}A_c = \Gamma\tilde{A}_c \tag{2.50}$$

$$\tilde{A}_c = \begin{bmatrix} 0 & n_x & n_y & n_z & 0 \\ n_x & \rho_m(n_x u + \Delta V) & \rho_m n_y u & \rho_m n_z & u\Delta V\Delta\rho \\ n_y & \rho_m n_x v & \rho_m(n_y u + \Delta V) & \rho_m n_z & v\Delta V\Delta\rho \\ n_z & \rho_m n_x w & \rho_m n_y w & \rho_m(n_z w + \Delta V) & w\Delta V\Delta\rho \\ 0 & \alpha_l n_x & \alpha_l n_y & \alpha_l n_z & \Delta V \end{bmatrix} \tag{2.51}$$

The aforementioned Riemann solver provides the convective flux on a face f such that

$$\vec{F}_{c,f} = \frac{1}{2}(\vec{F}_c(\vec{Q}_R) + \vec{F}_c(\vec{Q}_L)) - \frac{1}{2}\overline{\Gamma\left|\tilde{A}_c\right|}_f(\vec{Q}_R - \vec{Q}_L) \tag{2.52}$$

where $\overline{\left|\tilde{A}_c\right|}$ is the Roe averaged preconditioned Jacobian defined as

$$\left|\tilde{A}_c\right| = \tilde{R}^{-1}\left|\tilde{\Lambda}\right|\tilde{R} \tag{2.53}$$

and $\tilde{R}, \tilde{R}^{-1}$ and $\tilde{\Lambda}$ are the right, left eigenvectors and the eigenvalues of the preconditioned matrix $\tilde{A}_c$ respectively. The Jacobian in Eq. (2.53) is determined by using the Roe average quantities at the face f, which follow

$$\overline{\vec{u}} = \frac{\sqrt{\rho_R}\vec{u}_R + \sqrt{\rho_L}\vec{u}_L}{\sqrt{\rho_R + \sqrt{\rho_L}}}, \qquad \overline{\rho} = \sqrt{\rho_\alpha \rho_l} \tag{2.54}$$

The eigenvalues of the Jacobian matrix have similar form as in the case of the compressible flow equations, with the difference being that the pseudo-sound speed does not depend on the flow, but only on the artificial compressibility parameter.

$$\begin{aligned} \lambda_{1,2,5} &= V_n - V_g \\ \lambda_3 &= V_n - c - \frac{V_g}{2} \\ \lambda_4 &= V_n + c - \frac{V_g}{2} \end{aligned} \tag{2.55}$$

where c is the artificial sound speed discussed in the Artificial Compressibility subsection and in the case of two phase flows follows that

$$c = \sqrt{\beta + (V_n - \frac{V_g}{2})^2} \tag{2.56}$$

Finally, the right and left eigenvectors will be respectively

$$\tilde{R} = \begin{bmatrix} 0 & 0 & -\rho_m c_m & -\rho_m c_p & 0 \\ x_1 & x_2 & n_x + \frac{u\lambda_3}{\beta} & n_x + \frac{u\lambda_4}{\beta} & 0 \\ y_1 & y_2 & n_y + \frac{v\lambda_3}{\beta} & n_y + \frac{v\lambda_4}{\beta} & 0 \\ z_1 & z_2 & n_z + \frac{w\lambda_3}{\beta} & n_z + \frac{w\lambda_4}{\beta} & 0 \\ 0 & 0 & 0 & 0 & 1 \end{bmatrix} \tag{2.57}$$

$$\tilde{R}^{-1} = \begin{bmatrix} \frac{1}{\rho_m c_g}[n_x(wy_2 - vz_2) + n_y(uz_2 - wx_2) + n_z(vx_2 - uy_2)] & \frac{1}{c_g}[\beta(n_z y_2 - n_y z_2) + \Delta V(wy_2 - vz_2)] & \frac{1}{c_g}[\beta(n_x z_2 - n_z x_2) + \Delta V(uz_2 - wx_2)] & \frac{1}{c_g}[\beta(n_y x_2 - n_x y_2) + \Delta V(vx_2 - uy_2)] & 0 \\ \frac{1}{\rho_m c_g}[n_x(vz_1 - wy_1) + n_y(wx_1 - uz_1) + n_z(uy_1 - vx_1)]] & \frac{1}{c_g}[\beta(n_y z_1 - n_z y_1) + \Delta V(wy_1 - vz_1)] & \frac{1}{c_g}[\beta(n_z x_1 - n_x z_1) + \Delta V(wx_1 - uz_1)] & \frac{1}{c_g}[\beta(n_x y_1 - n_y x_1) + \Delta V(vx_1 - uy_1)] & 0 \\ -\frac{1}{\rho_m 2cc_g}(\beta + \lambda_4 V_n) & \frac{1}{2cc_g}\beta c_p n_x & \frac{1}{2cc_g}\beta c_p n_y & \frac{1}{2cc_g}\beta c_p n_z & 0 \\ -\frac{1}{\rho_m 2cc_g}(\beta + \lambda_3 V_n) & \frac{1}{2cc_g}\beta c_p n_x & \frac{1}{2cc_g}\beta c_p n_y & \frac{1}{2cc_g}\beta c_p n_z & 0 \\ 0 & 0 & 0 & 0 & 1 \end{bmatrix} \tag{2.58}$$

where $\vec{x}_1 = (x_1, y_1, z_1)$ and $\vec{x}_2 = (x_2, y_2, z_2)$ denote the unit vectors and

$$c_m = c - \frac{V_g}{2}, \qquad c_p = c + \frac{V_g}{2}, \qquad c_g = \beta + V_n \Delta V \tag{2.59}$$

2.2.4 Viscous Fluxes

The values of viscous fluxes on a face between two adjacent elements i, j are defined by a simple averaging as

$$\vec{Q}_{ij} = \frac{1}{2}(\vec{Q}_i + \vec{Q}_j) \tag{2.60}$$

Regarding the gradients, the Green-Gauss formula supplemented with a directional derivative is used

$$\nabla\vec{Q}_{ij} = \overline{\nabla\vec{Q}_{ij}} - \left[\overline{\nabla\vec{Q}_{ij}} \cdot \vec{t}_{ij} - (\frac{\partial\vec{Q}}{\partial l})_{ij}\right] \cdot \vec{t}_{ij} \tag{2.61}$$

where, $\overline{\nabla\vec{Q}_{ij}}$ is the mean gradient defined as

$$\overline{\nabla\vec{Q}_{ij}} = \frac{1}{2}(\nabla\vec{Q}_i + \nabla\vec{Q}_j) \tag{2.62}$$

$\vec{t}_{ij}$ is the unit vector pointing from cell center i to cell center j and l_{ij} denotes the distance between them.

2.3 Temporal Discretization

Proceeding with the discretization of the governing equations in the time scale, considering $\vec{Q}^*$ as the flow variables, the constituted implicit formulation will be

$$\Gamma\frac{\partial(\vec{Q}^*\Omega)}{\partial\tau} + \vec{R}^* = 0 \tag{2.63}$$

where $\vec{R}^*$ is the unsteady residual, including the spatial residual (2.25), as well as the unsteady term as per below

$$\vec{R}^* = \vec{R}_\Omega(\vec{Q}^*) + \Gamma_e\frac{\partial(\vec{Q}^*\Omega)}{\partial t} \tag{2.64}$$

Under the scope of dual time-stepping, two indices n and k are introduced to describe the iterations for the physical time and the fictitious time (or internal) respectively. In particular, for every computational step a pseudo-steady problem is solved, starting with $k = 0$ and the flow variables vector is initialized based on the previous convergent solution so that $\vec{Q}_0^{*,n+1} = \vec{Q}_k^n$. During this process, $\vec{Q}^*$ does not satisfy the original equation, whereas upon convergence the term $\Gamma\frac{\partial(\vec{Q}^*\Omega)}{\partial\tau}$ is eliminated and the initial equations are recovered.

A Backward Differentiation Formula (BDF) scheme [44] is employed for the discretization of the unsteady term, providing the following series of successive time levels

$$\frac{\partial(\vec{Q}\Omega_i)}{\partial t} = \frac{1}{\Delta t}\left[\phi_{n+1}(\Omega_i\vec{Q})^{n+1} + \phi_n(\Omega_i\vec{Q})^n + \phi_{n-1}(\Omega_i\vec{Q})^{n-1} + ...\right] \tag{2.65}$$

In the case of dynamic control volumes that change in time, the Geometric Conservation Law (GCL) [45] should be satisfied

$$\frac{d}{dt}\int_{\Omega_i(t)} dD = \oint_{\partial\Omega_i(t)} \vec{u}_{vol}\cdot\vec{n}dS \tag{2.66}$$

If the same BDF approach is applied, the GCL will provide that

$$\vec{R}_{GCL}^{n+1} = \sum_f^{N_f}(V_g\Delta S)_f^{n+1} = \frac{1}{\Delta t}\left[\phi_{n+1}(\Omega_i\vec{Q})^{n+1} + \phi_n(\Omega_i\vec{Q})^n + \phi_{n-1}(\Omega_i\vec{Q})^{n-1} + ...\right] \tag{2.67}$$

The pseudo-time derivative is discretized using a first-order backward diffference scheme as per below

$$\frac{\partial(\vec{Q}^*\Omega)}{\partial\tau} = \Omega_i^{n+1}\frac{\vec{Q}^{*,k+1} - \vec{Q}^{*,k}}{\Delta\tau} \tag{2.68}$$

Finally, the local time stepping technique is used for convergence facilitation purposes, according to which the local/cell-specific fictitious timestep is

$$\Delta\tau_i = CFL\frac{\Omega_i}{\hat{\Lambda}_{c,i}} \tag{2.69}$$

where $\hat{\Lambda}_{c,i}$ denotes the convective spectral radii defined as

$$\hat{\Lambda}_{c,i} = \sum_{j=1}^{N_f}\left(\left|V_n - \frac{V_g}{2}\right| + c\right)_{ij}\Delta S_{ij} \tag{2.70}$$

2.4 Turbulence Modelling

In general, the influence of turbulence on a flow might vary from quite large eddies until their cascade into viscosity scale effects. One approach to solving a fully turbulent flow is the Direct Numerical Simulation (DNS), which attempts a totally accurate numerical solution of the full spectrum of turbulent effects and thus requires significant computational power and fine resolution to capture even the smallest events. Another approach is based on the assumption that the large scale events contain the greater part of turbulent kinetic energy and are highly anisotropic, whereas during their decay, they tend to lose this energy and become more isotropic. Hence, the small scale motion is filtered out of the equations and

is subject to modelling, while the large scale eddies are resolved directly, leading to what is known in literature as the Large Eddy Simulation (LES). However, even the LES technique is too computationally expensive for the majority of practical applications.

The aforementioned methods are highly impractical and have limited applicability in large scale simulations, thus giving ground to the RANS turbulence closure models. The development of these models is based on the Boussinesq hypothesis about the Reynolds Stress tensor and attempt to capture the overall effect of turbulence on the flow by solving one or more transport equations to yield the value for the turbulent kinematic viscosity and determine the turbulent kinetic energy field. In the present study, the $k-\omega$ SST model has been employed in its original form [46], as well as in two more advanced formulations known as the Buoyancy-Modified $k-\omega$ SST [6] and Stabilized $k-\omega$ SST [7]. These alternative forms have been developed for the purpose of addressing the issue of turbulence over-production in breaking wave simulations and will be thoroughly described below.

2.4.1 The $k-\omega$ SST Model

The $k-\omega$ Shear Stress Transport model, is a two equation eddy-viscosity model and constitutes a blending technique between the traditional $k-\omega$ model near the domain's wall boundaries and the $k-\epsilon$ model in the free-stream region. Through this approach, the excellent behaviour of the former in near wall treatment, separation flows and adverse pressure gradients is combined with the superiority of the latter in handling inlet free-stream turbulence properties, while the need for damping functions is surpassed.

The advection-diffusion equations for the turbulent kinetic energy k and the specific dissipation rate ω are

$$\begin{aligned} &\frac{\partial(\rho k)}{\partial t} + \nabla(\vec{u}\rho k) = \nabla\big[(\mu + \sigma_k \mu_t)\nabla k\big] + \rho P_k - \beta^* \rho\omega k \\ &\frac{\partial(\rho\omega)}{\partial t} + \nabla(\vec{u}\rho\omega) = \nabla\big[(\mu + \sigma_\omega \mu_t)\nabla\omega\big] + \alpha\rho S^2 - \beta\rho\omega^2 + 2(1-F_1)\frac{\rho\sigma_{\omega 2}}{\omega}\nabla k \cdot (\nabla\omega)^T \end{aligned} \tag{2.71}$$

where $P_k = \min(\mu_t(\nabla\times\vec{u})(\nabla\times\vec{u})^T, 10\beta^*\rho k\omega)$ is the production term of turbulent kinetic energy, μ_t is the turbulent dynamic viscosity (or eddy viscosity) and $S = \sqrt{2S_{ij}S_{ij}}$ is the mean strain rate. Moreover, F_1 and F_2 are switching functions between the two aforementioned turbulence models and for $F_1 = 1$ the set of $k-\omega$ equations is solved, while the $k-\epsilon$ is activated when $F_1 = 0$. These functions are defined as

$$F_1 = tanh\left\{\left\{\min\left[\max\left(\frac{\sqrt{k}}{\beta^*\omega y}, \frac{500v}{y^2\omega}\right), \frac{4\rho\sigma_{\omega 2}k}{CD_{k\omega}y^2}\right]\right\}^4\right\} \tag{2.72}$$

$$F_2 = tanh\left\{\left[\max\left(\frac{2\sqrt{k}}{\beta^*\omega y}, \frac{500v}{y^2\omega}\right]^2\right\}\right. \tag{2.73}$$

$$CD_{k\omega} = \max\left(2\frac{\rho\sigma_{\omega 2}}{\omega}\nabla k \cdot (\nabla\omega)^T, 10^{-10}\right) \tag{2.74}$$

The constants for this model are: $\beta^* = 0.09$, $\alpha_1 = 5/9$, $\beta_1 = 0.075$, $\sigma_{k1} = 0.85$, $\sigma_{\omega 1} = 0.5$, $\alpha_2 = 0.44$, $\beta_2 = 0.0828$, $\sigma_{k2} = 1.0$ and $\sigma_{\omega 2} = 0.856$. These parameters are also subject to blending as per below

$$\phi = F_1\phi_1 + (1 - F_1)\phi_2 \tag{2.75}$$

Finally, a limiter is also imposed to the dynamic viscosity providing

$$\mu_t = \frac{\rho\alpha_1 k}{\max\big(\alpha_1\omega, SF_2\big)} \tag{2.76}$$

2.4.2 The Buoyancy Modified $k-\omega$ SST Model

The subject turbulent model, has been developed by Devolder [6] and has been successfully validated for studying breaking wave phenomena [47]. Its development has been based on the observation of inherent damping of non-breaking propagating waves of high-steepness, that is induced by the non-physical increase of the turbulent kinetic energy and the turbulent viscosity in the vicinity of the free-surface.

In order to address this issue, the following buoyancy term is added to the transport equation of k and it is treated implicitly

$$G_b = -\frac{\nu_t}{0.85}\frac{\partial\rho}{\partial x_i}g_i \tag{2.77}$$

This term is deliberately designed to serve a twofold purpose and is tailor-made for the study of wave shoaling and breaking. In particular, it suppresses the level of turbulence, by setting a laminar regime in the zone where the interface is horizontal and the density gradient is very large, driving μ_t to zero. Apart from that, when the wave front becomes vertical and the wave breaking occurs G_b is deactivated, providing a fully tubulent solution of the flow field.

2.4.3 The Stabilized $k-\omega$ SST Model

This turbulence closure model, has been developed by Larsen & Fuhrman [7], who identified all the past turbulence models to be unconditionally unstable in regions of nearly

potential flow with finite strain. This argument was backed up by an extension of the analysis of Mayer & Madsen [3], that proved an asymptotic exponential rate of increase of turbulence production in the aforementioned regions. Hence, according to them, the root cause of the irrepressible growth of the turbulent kinetic energy and the eddy viscosity in surface non-breaking waves, is the instability of the standard models in the bulk region below their free surface, where the mean rotation rate tensor $\Omega_{ij} = \frac{1}{2}\left(\frac{\partial u_i}{\partial x_j} - \frac{\partial u_j}{\partial x_i}\right)$ takes near zero values.

The stabilization approach for the $k-\omega$ SST model is the preservation of the buoyancy term of Devolder [6] and also, the addition of an extra term in the denominator of the eddy viscosity as follows

$$\mu_t = \frac{\rho\alpha_1 k}{\max\left(\alpha_1\omega, SF_2, \alpha_1\lambda_2\frac{\beta}{\beta^*\alpha}\frac{P_0}{P_\Omega}\omega\right)} \tag{2.78}$$

where $P_0 = 2S_{ij}S_{ij}$, $P_\Omega = 2\Omega_{ij}\Omega_{ij}$ and λ_2 is a constant that denotes the upper limit for the model to be formally stable, considering that $P_\Omega/P_0 \leq \lambda_2$. It is worth noticing that the new term will only be activated when the flow is nearly potential due to its insignificant rotation, while the initial Buoyancy Modified model will be recovered in shear regions.

Chapter 3

Numerical Wave Tank

3.1 Overview

The CFD-based numerical wave tank (NWT) is a numerical tool that emulates a physical wave tank (PWT) and due to its continuous optimization and diminishing computational cost, is widely used for the conduction of various two-phase flow simulations. Such cases might be complex free surface flows, like wave shoaling and breaking, as well as wave interaction with marine and offshore structures or floating bodies. In this type of flumes, waves are generated in the one end and absorbed by the other end, while the intermediate region is the domain of interest. The requirement of the generation zone is to properly and efficiently construct the desired wave, while the damping zone is dedicated to the effective absorption of reflections, induced either by the boundary or an interfering structure. In Fig. 3.1 a generic layout of a two-dimensional NWT is depicted.

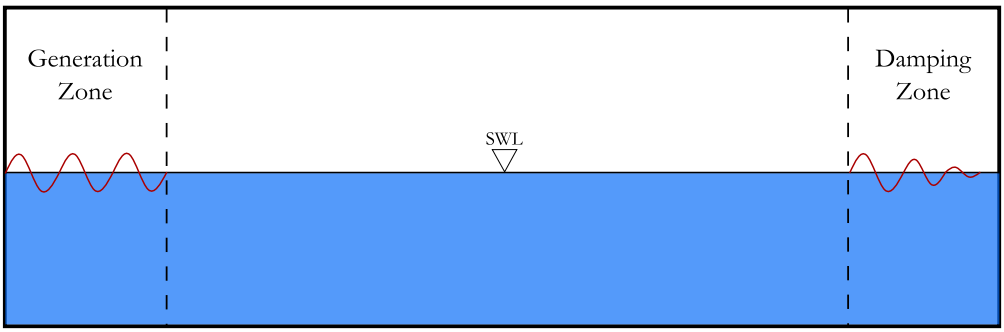

Figure 3.1: Setup of a generic numerical wave tank

3.2 Wave Generation and Absorption

Due to the high necessity for efficient and accurate wave generation, several different approaches have been developed in recent years, which are termed as numerical wave-makers. Some of these methods are: Relaxation Zone Method, Static and Dynamic Boundaries and Impulse Source Method. The same practices, along with the Numerical Beach and the Cell Stretching Method can be implemented also for the artificial damping of the waves. More details, as well as a general overview and assessment of the aforementioned methods for wave generation and absorption can be found in [48] and [49].

In the present work, a modified Relaxation Zone Method [50] has been adopted for both wave generation and absorption, termed as the Forcing Zone Method. In particular, the numerical solution inside the generation zone is forced to implicitly converge to a wave profile outlined by a suitable wave theory, while in the damping zone it is artificially damped in the same way. Damping of the numerical solution is strongly required, in order to prevent any physical disturbance to reach the outlet boundary, as the boundary conditions assume a uniform field. Both of these procedures are achieved by adding an appropriate source term to the momentum equation, the general form of which is

$$\vec{S}_{nwt} = C_{nwt}\rho_m(\vec{\phi} - \vec{\phi}_{tar}) \tag{3.1}$$

In the above equation, the term $\vec{\phi}$ stands for variables such as the velocity vector $\vec{u}$, the volume fraction a or the scalar pressure p, whereas $\vec{\phi}_{tar}$ is the value towards which $\vec{\phi}$ is driven. The choice of the variables which are included is case dependent and is correlated with the geometry and the physics of the computational domain. Moreover, the effect of the source term is controlled by the term C_{nwt} which requires special treatment and is provided by the following equation

$$C_{nwt} = \alpha\frac{e^{x_r^n} - 1}{e - 1} \qquad x_r = \frac{x_s - x}{x_s - x_e} \tag{3.2}$$

where x_r is a non-dimensional normalized space variable and ranges between the starting and ending position of the forcing zone. Parameter α regulates the maximum value of the forcing function, while parameter n regulates its spatial distribution. The values of these two constants should be selected properly and a case-specific study is generally suggested, as large values of α may lead to numerical instabilities and hinder convergence, whereas small values of it may not be sufficient for driving the solution to the desired form. The function takes its maximum values in the internal boundaries of the computational domain with the zones and reaches zero at the other end of each zone. Different forcing functions for two sets of parameters α and n are shown in Fig. 3.2.

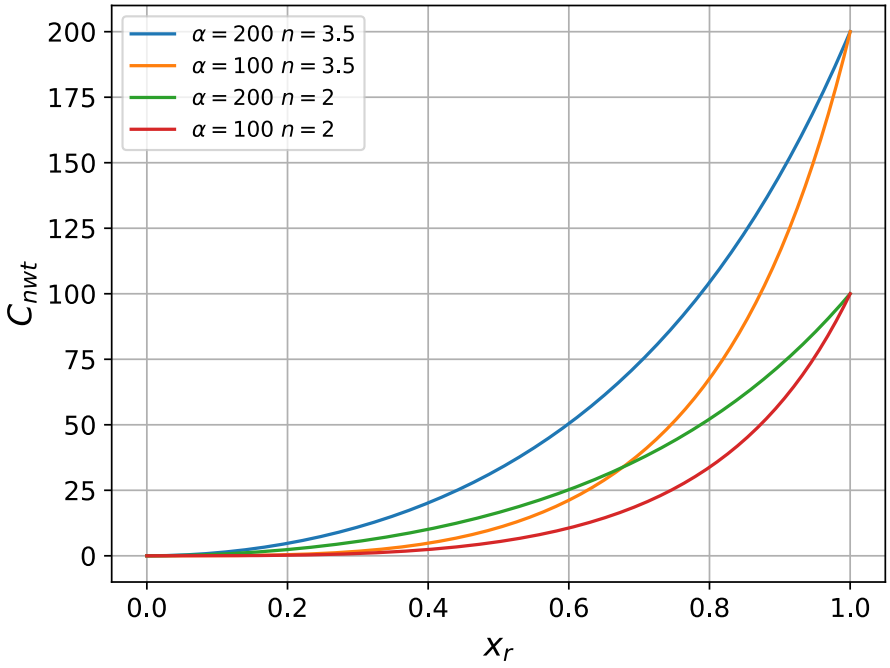

Figure 3.2: Effect of the coeffients α and n on the forcing zone function

3.3 Wave Theories

The wave features towards which the numerical solution is forced inside the generation zone are derived from a range of several suitable wave theories, some of which are discussed in the current section. In order to extract the desired formulations for the free surface profile, the velocity components, as well as the pressure, the simple problem of two-dimensional plane wave propagation over a flat impermeable bed is considered. The wave propagates in the horizontal direction and the fluid domain is bounded by a free surface at $z = \eta(x, t)$. The mean surface elevation is at level $z = 0$, whereas $z = -h$ corresponds to the flat seabed.

3.3.1 Airy Wave Theory

In the context of this theory also known as the Linear Wave Theory, or Infitesimal Wave Theory [51], the flow is assumed to be incompressible, inviscid and irrotational. Hence, the fluid velocity can be expressed as the gradient of a velocity potential $\vec{u} = \nabla\phi$, which transforms the continuity equation to a Laplace equation (Eq. 3.3) and the effect of the free surface is introduced by an appropriate kinematic and dynamic condition.

$$\nabla\vec{u} = 0 \Rightarrow \Delta\phi = \frac{\partial^2\phi}{\partial x^2} + \frac{\partial^2\phi}{\partial z^2} = 0 \tag{3.3}$$

Starting with the kinematic condition, it is required that the substantial derivative of the fluid and the free surface must be equal for $z = \eta$, which is translated into

$$\frac{D\eta}{dt} - \frac{Dz}{dt} = \frac{\partial \eta}{\partial t} + \frac{\partial \phi}{\partial x}\frac{\partial \eta}{\partial x} + \frac{\partial \phi}{\partial z}\frac{\partial \eta}{\partial z} - \frac{\partial \phi}{\partial z} = 0 \tag{3.4}$$

Under the assumption that the wave elevation is sufficiently small, $\frac{\partial \eta}{\partial x}$ and $\frac{\partial \eta}{\partial z}$ will be similarly small, thus the second order terms can be ignored, giving that

$$\frac{\partial \eta}{\partial t} = \frac{\partial \phi}{\partial z} \tag{3.5}$$

The dynamic condition can be derived from the Bernoulli equation, when considering the pressure gradient at $z = \eta$ to be equal with the atmoshperic. By substituting the free surface expression η instead of z and solving in respect to it the expression is

$$\eta = \frac{1}{g}(\frac{\partial \phi}{\partial t} + \frac{1}{2}\nabla\phi\nabla\phi) \tag{3.6}$$

Again, by ignoring the second order terms, the previous equation is simplified further to

$$\eta = \frac{1}{g}\frac{\partial \phi}{\partial t} \tag{3.7}$$

Finally, the interpermeable bed requires the following kinematic bed condition to be imposed at $z = -h$,

$$\frac{\partial \phi}{\partial z} = 0 \tag{3.8}$$

Considering the simplest solution of the aforementioned problem to be the plane progressive wave, the free surface will have the general form

$$\eta(x,t) = Acos(kx - \omega t + \epsilon) \tag{3.9}$$

where A is the wave amplitude, $\omega = \frac{2\pi}{T}$ is the radial frequency, T is the wave period, $k = \frac{2\pi}{\lambda}$ is the wavenumber, λ is the wavelength and ϵ is an arbitrary phase angle.

The velocity potential for that finite depth case after solving this Laplace equation and applying all the boundary conditions will be:

$$\phi(x,z,t) = \frac{gA}{\omega}\frac{cosh[k(z+h)}{cosh(kh)}sin(kx - \omega t + \epsilon) \tag{3.10}$$

Moreover, the corresponding dispersion relation that connects the wavenumber with the radial frequency is given as:

$$\omega^2 = gktanh(kh) \tag{3.11}$$

Hence the phase velocity follows that:

$$c = \frac{\omega}{k} = [(g/k)tanh(kh)]^{1/2} \tag{3.12}$$

The velocity components of the fluid follow that:

$$u(x,z,t) = \frac{\partial u}{\partial x} = A\omega\frac{cosh[k(z+h)]}{sinh(kh)}cos(kx - \omega t + \epsilon) \tag{3.13}$$

$$w(x,z,t) = \frac{\partial u}{\partial z} = A\omega\frac{sinh[k(z+h)]}{sinh(kh)}sin(kx - \omega t + \epsilon) \tag{3.14}$$

Finally, the pressure will be

$$p(x,z,t) = \rho gA\frac{cosh[k(z+h)]}{cosh(kh)}cos(kx - \omega t + \epsilon) \tag{3.15}$$

3.3.2 Stream Function Theory

The approach described in the present section follows the formulation first introduced by Fenton and Rienecker [52],[53]. Considering that the fluid is incompressible, a stream function ψ exists such that the velocity components are $u = \frac{\partial \psi}{\partial z}$ and $w = -\frac{\partial \psi}{\partial z}$. Under the assumption that the flow is irrotational, this stream function satisfies the Laplace equation throughout the field.

$$\Delta\psi = \frac{\partial^2 \psi}{\partial x^2} + \frac{\partial^2 \psi}{\partial z^2} = 0 \tag{3.16}$$

The boundary conditions that the fluid is subject to are:

$$\psi(x, -h) = 0 \tag{3.17}$$

$$\psi(x, \eta(x,t)) = -Q \tag{3.18}$$

where Q is a positive constant that corresponds to the total volumetric flow rate below the steady wave per unit length in a direction normal to the x, z plane.

Application of the Bernoulli equation on the free surface, where the pressure is constant provides,

$$\frac{1}{2}(\frac{\partial^2 \psi}{\partial x^2} + \frac{\partial^2 \psi}{\partial z^2}) + \eta = R \tag{3.19}$$

where R is a pressure-dependent constant.

In the equations used above, all parameters have been non-dimensionalized with respect to the average free surface elevation $\bar{\eta}$ and gravitational acceleration g, such that the coordinates x, z denote $(x/\bar{\eta})$ and $(z/\bar{\eta})$ respectively. In a similar manner, the free surface elevation η corresponds to $(\eta/\bar{\eta})$, ψ to $\psi/(g\bar{\eta}^3)^{\frac{1}{2}}$, Q to $Q/(g\bar{\eta}^3)^{\frac{1}{2}}$ and R to $R/g\bar{\eta}$.

By exploiting the symmetry of the wave about the crest, the series of $\psi(x, z)$ is

$$\psi(x,z) = B_0 z + \sum_{j=1}^{N} B_j \frac{sinh(jk\eta)}{cosh(jkh)} cos[jk(x - ct)] \tag{3.20}$$

Hence, the non-dimensional velocity components follow

$$u(x,z) = B_0 + k\sum_{j=1}^{N} jB_j \frac{cosh(jk\eta)}{cosh(jkh)} cos[jk(x - ct)] \tag{3.21}$$

$$w(x,z) = k\sum_{j=1}^{N} jB_j \frac{sinh(jk\eta)}{cosh(jkh)} sin[jk(x-ct)] \tag{3.22}$$

So far, equations (3.18) and (3.19) constitute a system of $2N+2$ equations for $2N+5$ variables η_j, B_j, k, Q and R. If the values of Q and R are defined, one more equation is needed in order to obtain a solution. This remaining equation is provided by the non-dimensional free surface elevation

$$\frac{1}{2N}[\eta_0 + \eta_N + 2\sum_{j=1}^{N-1} \eta_j] - 1 = 0 \tag{3.23}$$

where η_0 denotes the free surface elevation at the crest and η_N at the trough of the wave.

In the case that Q and R are not specified, the wave speed $c = \frac{\omega}{k} = \frac{\lambda}{T}$ needs to be introduced and three more equations are required which are:

$$\eta_0 - \eta_N = H \tag{3.24}$$

$$c - c_E + B_0 = 0 \tag{3.25}$$

$$c - c_s - Q = 0 \tag{3.26}$$

where c_E denotes the time mean Eulerian current velocity and c_s the mean particle drift velocity or alternatively the vertically integrated mass transport velocity. Both of these parameters are constant and depend on the case under consideration.

Thus, a system of 2N+6 equations for the unknown variables η_j, B_j, k, c, Q and R is constituted and may be solved using the Newton-Raphson Method, setting the initial values as the equivalent quantities from the Airy Theory. Upon convergence of the method, the discrete Fourier transform of the free surface elevation shall be

$$Y_j = \frac{2}{N}\sum_{m=0}^{N} k\eta_m cos[jk(x-ct)] \tag{3.27}$$

The free surface elevation in a dimensional form will be

$$\eta = \frac{1}{k}\sum_{j=1}^{N} Y_j cos[jk(x-ct)] \tag{3.28}$$

Transition from the non-dimensional field quantities to dimensional ones may occur as

follows

$$u(x,z) = (g/k)^{\frac{1}{2}}[B_0 + k\sum_{j=1}^{N} jB_j \frac{cosh(jk\eta)}{cosh(jkh)} cos[jk(x-ct)]] \tag{3.29}$$

$$w(x,z) = (g/k)^{\frac{1}{2}}[k\sum_{j=1}^{N} jB_j \frac{sinh(jk\eta)}{cosh(jkh)} sin([jk(x-ct)]] \tag{3.30}$$

Finally, the corresponding pressure will be

$$p(x,z) = \rho(R - gh) - \frac{1}{2}\rho[(u-c)^2 + v^2] \tag{3.31}$$

Chapter 4

Regular Wave Propagation Over Flat Bottom

Solver *MaPFlow* has been already tested for the accurate generation and propagation of regular water waves both on constant and variable bathymetry and the numerical results were in very good agreement with the experimental [16]. In this chapter, a parametric study is carried out as a preparatory stage of the analysis of breaking waves, in order to determine several solver and NWT settings and extend their applicability to the next case study. Hence, the propagation of the spilling wave of the next chapter is investigated, so as to explore the influence of the wave generation and damping, the artificial compressibility coefficient, as well as the employed reconstruction scheme on the numerical results. First, a grid and timestep independence study is conducted and afterwards the impact of all the aforementioned parameters is isolated and examined.

4.1 Numerical Setup

The wave under consideration is a Stokes 2^{nd} order wave, with a height of $H = 0.125$ m and a period $T = 2$ s. For the purposes of this study, a 10 wavelength long numerical wave tank was created ($L = 38.43$ m), assigning one wavelength to the generation zone and two to the damping zone, inside which only the vertical velocity component is subject to damping. Usually, the damping zone shall be limited to one wavelength, however the wave under consideration is of large steepness and thus large velocities are induced, which lead to the need for stronger damping. Fig. 4.1 shows the numerical wave tank, as well as the wave gauges that were placed in targeted locations. One gauge was placed right outside the generation zone at $x_{WG1} = 4$ m in order to evaluate the generated wave. Another gauge was put at the intermediate part of the domain at $x_{WG2} = 20$ m, in order to have insight about the propagation of the wave. Finally, the last gauge was placed right before the damping zone at $x_{WG3} = 30.7$ m in order to account for reflections.

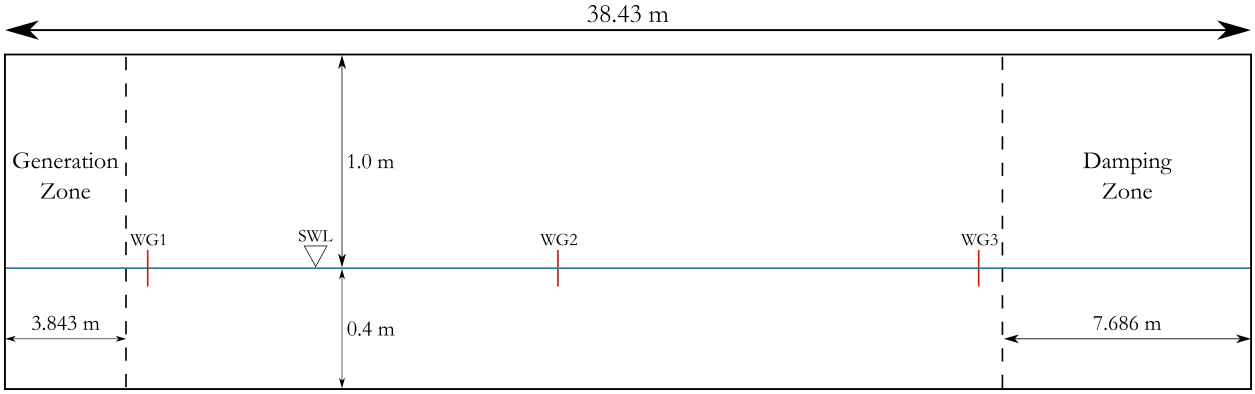

Figure 4.1: Configuration of the numerical wave tank for the regular wave propagation case

The numerical model was tested for the three grid resolutions of ascending number of cells, shown in Table 4.1 with a timestep of $dt = T/800$, derived from the results of Ntouras and Papadakis [16] for a cnoidal wave. Each mesh is uniform in the horizontal direction, whereas in the vertical direction the mesh is denser in the vicinity of the free surface and gradually coarsens towards the upper boundary, while it is also dense near the bottom, in order to capture the boundary layer.

	Nodes	Cells per H	Cells per λ
G1	20000	8	50
G2	130000	28	120
G3	210000	40	151

Table 4.1: Grid resolutions for the regular wave propagation case

Moreover, the simulation for $G2$ was carried out again for a timestep of $dt = T/400$ and $dt = T/1600$. The results for the grid and timestep sensitivity study are presented in Fig. 4.2. From this analysis, it is concluded that $dt = T/800$ s for the grid $G2$ show a good agreement with the analytical data and is computationally affordable, thus the parametric study was conducted for this setup. In all figures presented next, the 25^{th} wave is illustrated. As default solver settings, $\beta = 5$ was chosen and the BICS reconstruction scheme was employed for the volume fraction. It is also worth noticing that when the present simulation was conducted without a turbulence model, several deformations were observed in the vicinity of the free-surface, so the Buoyancy Modified $k - \omega$ SST Model was employed to close the RANS equations.

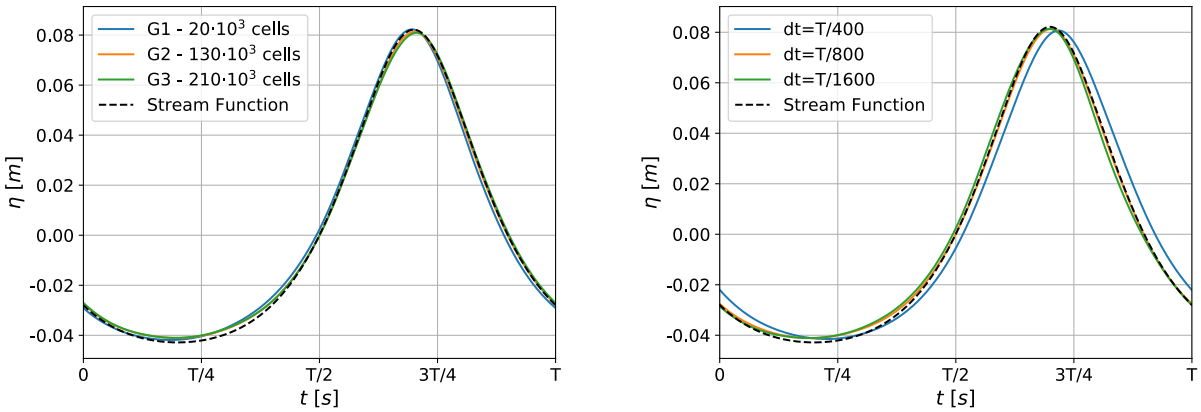

(a) Simulated and analytical wave profile for $G1, G2, G3$

(b) Simulated and analytical wave profile for $dt = T/400, T/800$ and $T/1600$

Figure 4.2: Grid sensitivity study for plunging breaking wave

4.2 Parametric Study

4.2.1 Generation Zone Coefficients

As a first step, the simulation was carried out for different sets of parameters α and n in order to provide an insight about the way these coefficients regulate wave generation. In Fig. 4.3, the influence of α and n on the wave profile at WG1 is shown by keeping the other parameter constant each time. A remark that can be drawn is that for a quite small value of n and thus, a quite steep forcing function, the wave generation is more accurate and effective, while α is a less sensitive parameter.

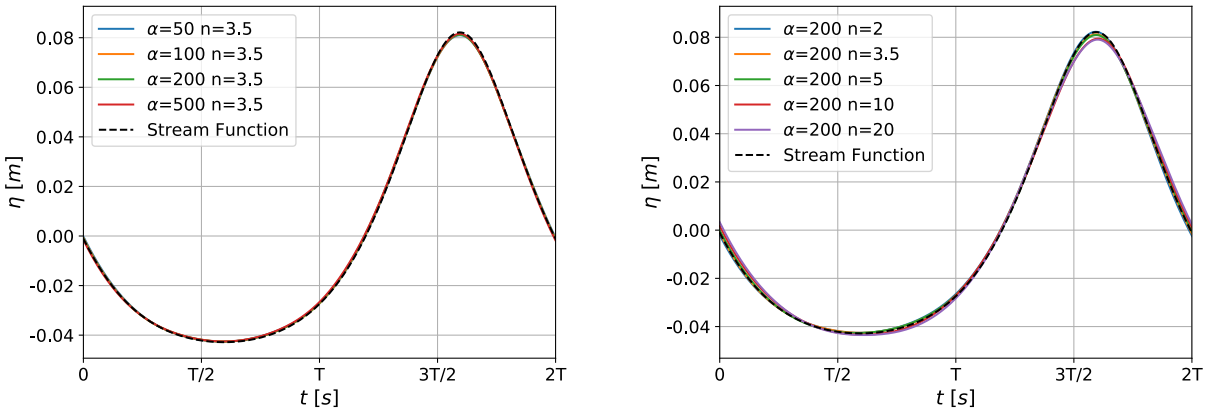

Figure 4.3: Effect of parameter α (left) and n (right) on wave generation (H=0.125 m, T=2 s)

4.2.2 Damping Zone Coefficients

Following, $\alpha = 200$ and $n = 3.5$ were retained for the generation zone and the influence of the wave damping on the solution was isolated, as different values of α for the damping function were tested. In Fig. 4.4 the wave profile at WG3 is shown for the examined parameter. Reflections seem to be caused for $\alpha = 500$, since there is a quite large phase angle difference with the rest, which cannot be credited to generation or dispersion, since all the rest solver settings were kept the same.

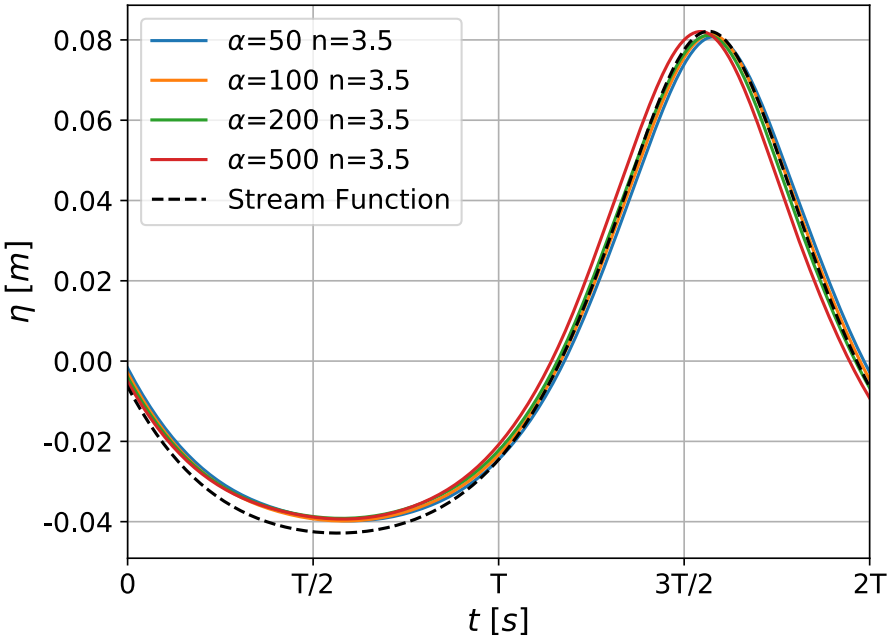

Figure 4.4: Effect of parameter a on wave damping (H=0.125 m, T=2 s)

4.2.3 Artificial Compressibility

Next, the influence of the artificial compressibility β was investigated, which proved to be the most sensitive parameter among all considered in this case study. According to Ntouras and Papadakis [16] values of β between 10 and 100 for a cnoidal wave of $H = 0.05\ m$, $T = 5\ s$ and a depth of $0.5\ m$, seem to provide results that agree well with the Stream Function results. However, it is evident from Fig. 4.5, that this deduction cannot be universalized for all types of waves, as for this Stokes 2^{nd} order wave, the range of accuracy is much more narrow and the results agree with the Stream Function Theory only for $\beta = 5$ and $\beta = 10$. An explanation to this, might be the wave steepness, which caused very high velocities near the wave crest, but further research is suggested.

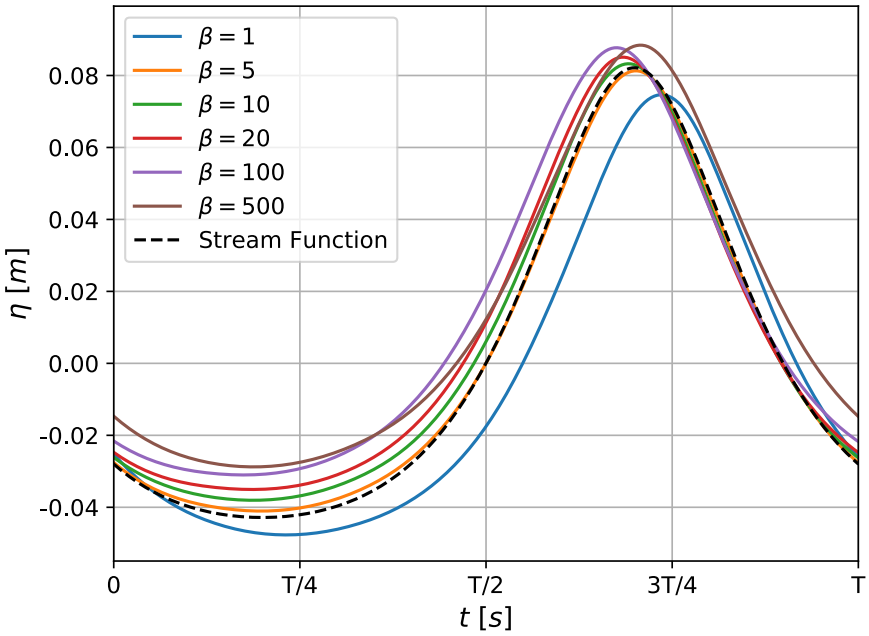

Figure 4.5: Effect of artificial compressibility on wave propagation (H=0.125 m, T=2 s)

4.2.4 Reconstruction Scheme

Finally, different reconstruction schemes were implemented for the volume fraction α in the interface between the two fluids. All, the Interface Capturing Schemes discussed in Section 2 are investigated, along with PLR in order to highlight the defect of this scheme in reconstructing α. As shown in Fig. 4.7, apart from CICSAM and MGDS, all the other reconstruction schemes provide very similar free surface elevation profiles and can be used for the propagation of plane-progressing waves. However, as illustrated in the snapshots of Fig. 4.6 the proper selection of the reconstruction scheme influences directly the success or failure of the VOF method to capture the interface between the two phases. In these terms, HRIC and BICS are the most accurate and of little difference in the level of compression. Next, STACS seem to reconstruct a thicker free-surface, while CICSAM is over-compressing, resulting in small deformations of the interface. Finally, MGDS seems to be also quite accurate but is subject to very large numerical diffusion, which renders it impractical for the present work.

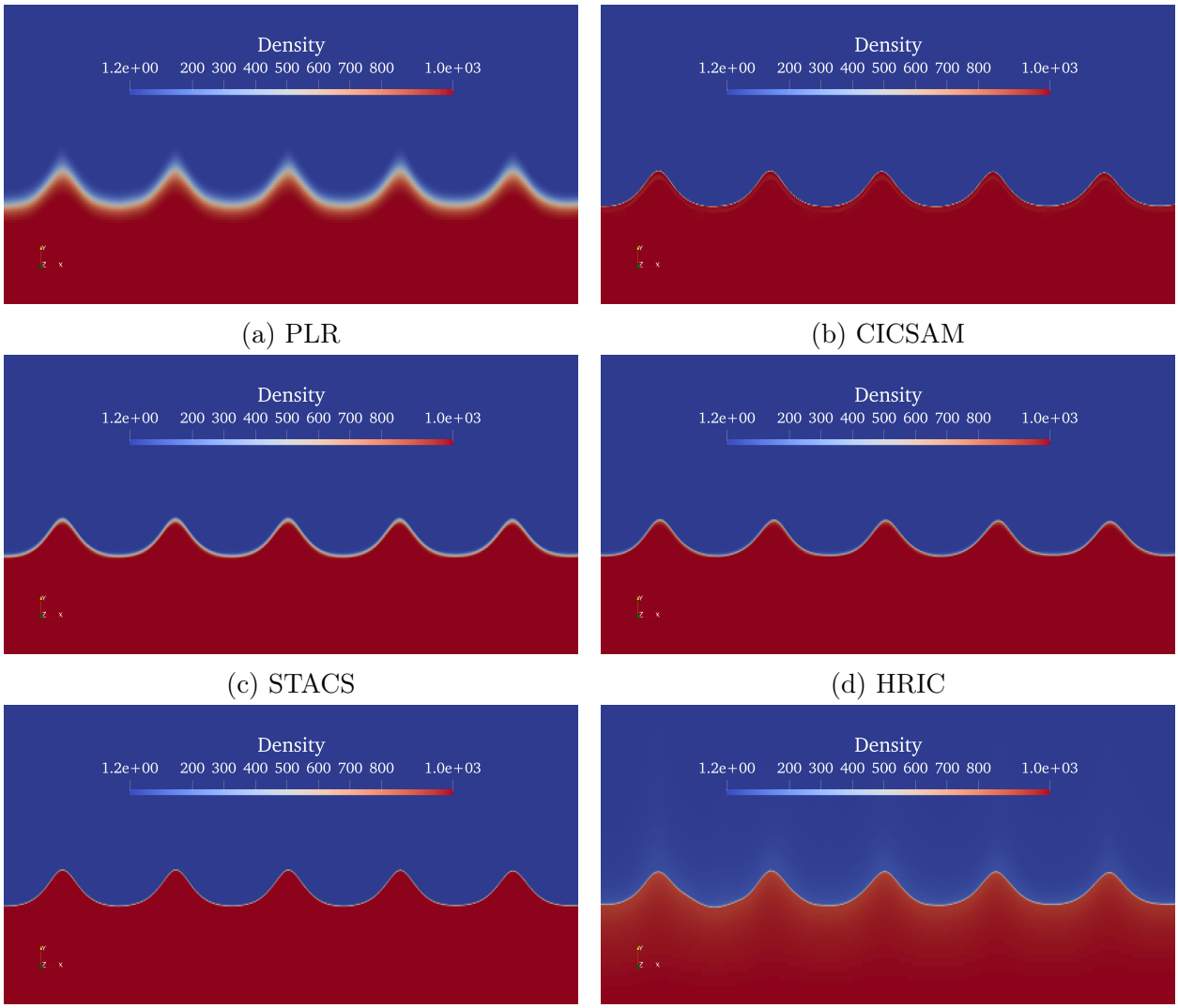

(a) PLR (b) CICSAM

(c) STACS (d) HRIC

(e) BICS (f) MGDS

Figure 4.6: Effect of reconstruction schemes on free-surface capturing (H=0.125 m, T=2 s)

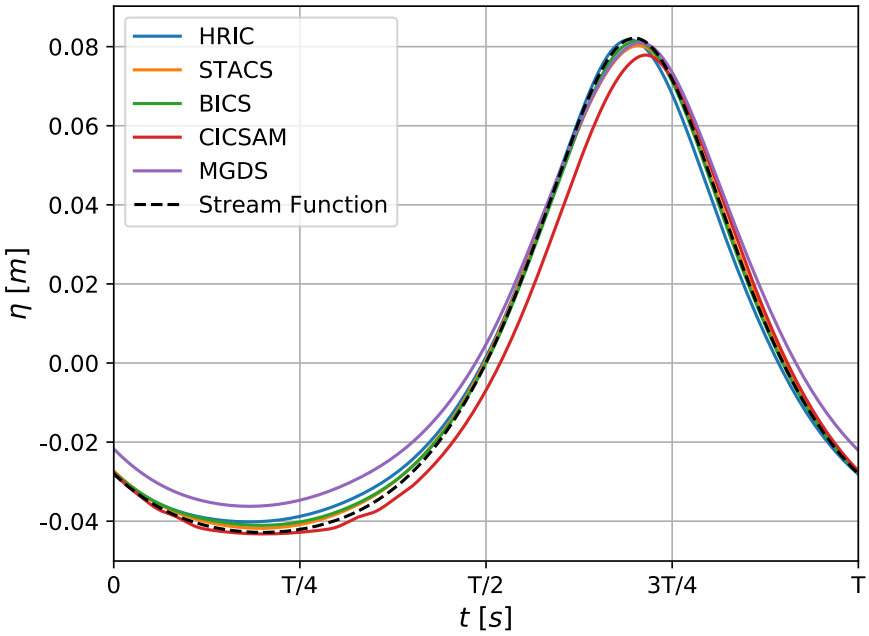

Figure 4.7: Effect of reconstruction schemes on wave propagation (H=0.125 m, T=2 s)

Chapter 5

Breaking Regular Wave Propagation Over Slope

In this Chapter, the extent to which *MaPFlow* is capable of capturing the complex phenomenon of wave breaking is investigated. For this purpose, the experimental study of Ting & Kirby [54] is considered, which includes the analysis for a plunging cnoidal wave and a spilling Stokes 2^{nd} order wave. A first insight for the generation and propagation of the incident waves can be derived from the work of Ntouras & Papadakis [16] and Chapter 4, in which a thorough parametric study about the basic solver and NWT setting was carried out. Moreover, a comparison and evaluation of the following turbulence modelling cases is conducted:

- No Turbulence Modelling
- Standard $k-\omega$ SST
- Buoyancy Modified $k-\omega$ SST
- Stabilized $k-\omega$ SST

5.1 Numerical Setup

The main features of the waves under investigation are shown in Table 5.1. For the context of this study, a two-dimensional numerical wave tank identical with the physical wave tank of the experiment was considered, which is shown in Figure 5.1. The depth at the flat bottom region is 0.4 m, while at $x = 0$, an impermeable sloped beach of $m = 1/35$ begins with a beach toe of $m = 1:1$ placed at $x = -0.02$ m. In the case of the plunging wave, one wavelength λ was assigned to the generation zone and 0.75λ to the damping zone, whereas in the case of the spilling wave these zones were of 3λ and 2.25λ respectively. In

this study, apart from the vertical velocity components, also the horizontal velocity and the volume fraction were artificially damped, in order to avoid reflections from the sloped bed.

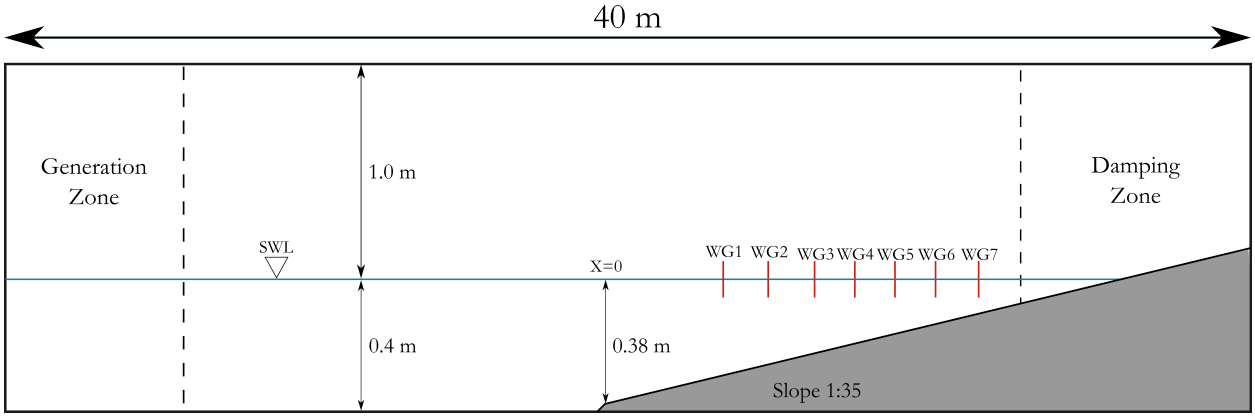

Figure 5.1: Configuration of the numerical wave tank for the breaking regular wave case

Wave	$H\ (m)$	T (s)	$\lambda\ (m)$
Spilling	0.125	2	3.843
Plunging	0.128	5	10.656

Table 5.1: Wave characteristics in Ting & Kirby experiments [54]

For the measurement of the horizontal velocity and turbulent kinetic energy inside the domain, several numerical wave gauges were placed, which differ between the two wave cases and are presented in Table 5.2.

	WG1 (m)	WG2 (m)	WG3 (m)	WG4 (m)	WG5 (m)	WG6 (m)	WG7 (m)
Spilling	5.945	6.665	7.275	7.885	8.495	9.110	9.725
Plunging	7.295	7.795	8.345	8.795	9.295	9.795	10.395

Table 5.2: Wave gauge positions for spilling and plunging breaker

First, a grid and timestep independence study was conducted for the plunging wave, which is the most complex of the two. A timestep of $dt = T/2000$ and the Buoyancy Modified $k-\omega$ SST model were set as default and it was tested for the three mesh resolutions shown in Table 5.3, where 'Cells per λ' refer to the region where the breaking occurs.

The criterion for selecting a grid resolution was decided to be the physical properties of the wave at the breaking onset, meaning the $20T$ average horizontal position where it occurs, as well as the wave height at this particular point. The discrepancies between the numerical point of breaking x_{bn} and wave height at breaking h_{bn}, from the experimental $x_{be} = 7.795\ m$ and $h_{be} = 0.19\ m$ are presented in Fig. 5.2

	Nodes	Cells per H	Cells per λ
G1	56000	14	225
G2	167000	22	470
G3	278000	30	710
G4	374000	36	825

Table 5.3: Grid resolutions for regular breaking wave case

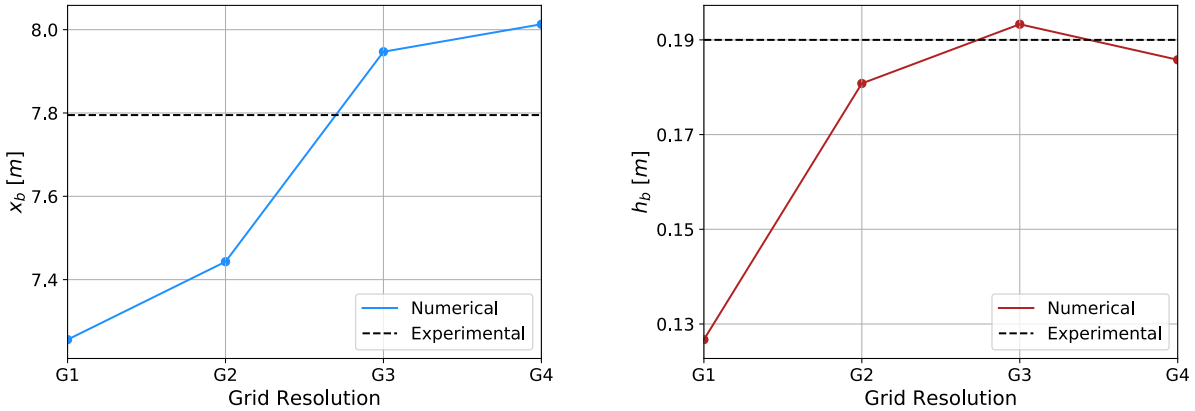

(a) Breaking position deviation

(b) Breaking height deviation

Figure 5.2: Grid sensitivity study for plunging breaking wave

Then the simulation was conducted again for grid resolution G3 with a timestep of $dt = T/1000, T/2000$ and $T/4000$, retaining the same criterion for the breaking state properties.

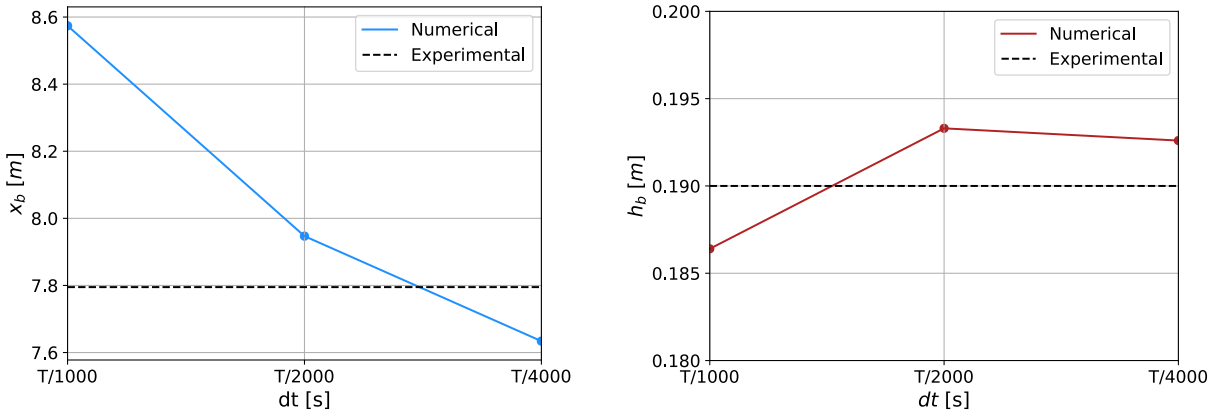

(a) Breaking position deviation

(b) Breaking height deviation

Figure 5.3: Timestep sensitivity study for plunging breaking wave

5.2 Results and Discussion

Time-averaged free surface elevations

In Fig. 5.4 and 5.8 the numerical and experimental time averaged free surface elevations are presented, where the three solid blue lines represent the maximum, average and minimum elevations (from top to bottom), over the last 20 periods of the simulation. The horizontal axis coincides with the horizontal axis of the domain in the region where experimental results were available, while vertical corresponds to the surface elevations.

An observation that was made in both the plunging and the spilling wave is that in the case of no turbulence model employed, where the whole flowfield was considered laminar, the wave is not damped properly by the breaking process, since the transported mechanical energy cannot be converted to turbulent kinetic energy, thus the damping occurs only through viscous dissipation and due to interaction with the seabed. However, for the same reason the wave height near the breaking position for this case is larger compared with the turbulence model cases. Also some disturbances of the free-surface were observed, which are depicted in the form of wiggles in the minimum elevation curve of this case.

Regarding all the other cases where a turbulence model was implemented, the minimum and average free surface elevations do not seem to be affected much by the choice of the turbulence model, so the analysis was focused on the maximum elevations. In particular, the offset of the $k-\omega$ SST maximum elevation curve towards the positive x, denotes a delay in the prediction of breaking in that model for both the spilling and the plunging breaker. The Buoyancy Modified $k-\omega$ SST model has a very good agreement with the experimenta data for both waves and gives the most accurate overall results in the context of free surface elevations. Finally, the Stabilized model has the same effect as the Buoyancy Modified, regarding the free-surface elevation profiles. An interesting detail about the use of this model is regarding the parameter λ_2 that regulates the activation of the limiter, according to the extent of the potential flow. In particular, it was selected as $\lambda_2 = 0.05$ for the plunging breaker, a value that was also indicated by Larsen & Fuhrman [7], while for the spilling breaker the value that gave the most accurate results was for $\lambda_2 = 0.005$. Of course, this can be explained by the less turbulent nature of the breaking of spilling waves, when compared to plunging, thus resulting in a larger region of nearly potential flow.

Finally, several authors such as Liu et al. [8] have found that regardless the choice of turbulence model, early prediction of the breaking position was observed due to disturbances from spurious air velocities. These disturbances occur because in the context of pressure-correction algorithms (such as PIMPLE, SIMPLE etc.) the equations are segregated, meaning that they are solved in sequence. Their proposal for eliminating these velocities was the implementation of jump free-surface conditions as introduced by Vukcevic et al. [9]. In the present study, the coupling of the RANS equations with the method of artificial compressibility, forms a single system of equations, which are solved in a non-segregated manner and hereby, resolves this problem.

Time-averaged horizontal velocity profiles

In Fig. 5.5 and 5.9 the numerical and experimental results of the time averaged horizontal velocities at the stations of Table 5.2 and over the last 20 periods of the simulation are presented. The horizontal axis corresponds to the velocity values, while the vertical axis coincides with the y axis of the domain near the free-surface. Moreover, in every figure, the RMSE of the numerical results with respect to the experimental data is shown, for quantitative comparison between the turbulence model cases. All simulations seem to predict well the qualitative behaviour of the undertow, with the horizontal velocity being negative beneath the free surface, while it obtains positive values in that area. However, apart from the well captured transition, a slight overprediction of the horizontal velocities is observed in all turbulence models, which is caused by the large turbulent velocity components and is mitigated when the Buoyoancy Modified or the Stabilized model are employed. In addition to that, the aforementioned over-prediction is intensified while moving towards the inner surfzone due to strong three-dimensional effects that lead to a spanwise velocity comparable to the the other two dimensions [8].

Time-averaged turbulent kinetic energy profiles

In Fig. 5.6 and 5.10 the numerical and experimental results of the time averaged turbulent kinetic energy profiles at the stations of Table 5.2 and over the last 20 periods of the simulation are depicted. The horizontal axis corresponds to the $\overline{k}$ values, while the vertical axis coincides with the y axis of the domain near the free-surface. It should be highlighted that the over-estimation of this quantity that can be shown in the case of the $k-\omega$ SST model is the main motivation of the development of the next two, so the investigation of their effect is of crucial importance. According to Devolder [47] the main reason of this problem is that the traditional turbulence models were not designed to account for the existence of the free surface and also, the flow interactions in the spanwise direction are not solved, due to consideration of a two-dimensional numerical wave tank.

For the first two probes, no experimental data were available, since Ting & Kirby [54] were not anticipating the existence of turbulence at these positions. On what concerns the rest of the gauges, it is evident that the $k-\omega$ SST model case follows the experimental $\overline{k}$ quite accurately, until the discontinuity of the free-surface, where an irrepressible growth is observed. In the case of the Buoyancy Modified $k-\omega$ SST model, the aforementioned growth of the turbulent kinetic energy is contained in the vicinity of the free-surface, where the artificial laminar regime is imposed, however the augmentation right above that point is still not prevented. Moreover, while moving towards the inner surfzone where the density gradients are not vertical anymore, the effect of the buoyancy term fades, thus leading to the reappearance of the turbulence overproduction problem. On the contrary, the Stabilized $k-\omega$ SST model leads to only a local augmentation of $\overline{k}$ on the free-surface, while it tends to obtain near-zero values above this area. Moreover, this effect is not eliminated when proceeding to the inner surfzone, thus rendering it the most accurate turbulence model in the present aspect.

Eddy Viscosity

In order to provide a deeper insight on the turbulent behaviour of wave breaking, the contour plots of the turbulent viscosity during breaking is presented in Fig. 5.7 and 5.11. The snapshots have been taken during the last period under examination, so the unconditional instability of the $k-\omega$ SST and the Buoyancy Modified $k-\omega$ SST, that Larsen & Fuhrman [7] refer to are evident. From a qualitative aspect, a generation of turbulence on the wave front is anticipated and then the gradual spreading throughout the neighboring region, through the convection and diffusion terms. For both the spilling and the plunging wave, the $k-\omega$ SST model presents turbulent kinematic viscosity greater than the laminar ($\approx 10^{-6}$) by several magnitudes. This unphysical trend is limited in the vicinity of the free-surface and in the region prior to breaking by including the buoyancy term in the equations, however turbulence overproduction is still present in the propagating wave. Finally,the implementation of the Stabilized $k-\omega$ SST model seems to provide better qualitative configuration of the turbulent regime, since the viscosity is maintained low until the breaking point and then grows inside the surfzone.

5.2.1 Spilling Breaker

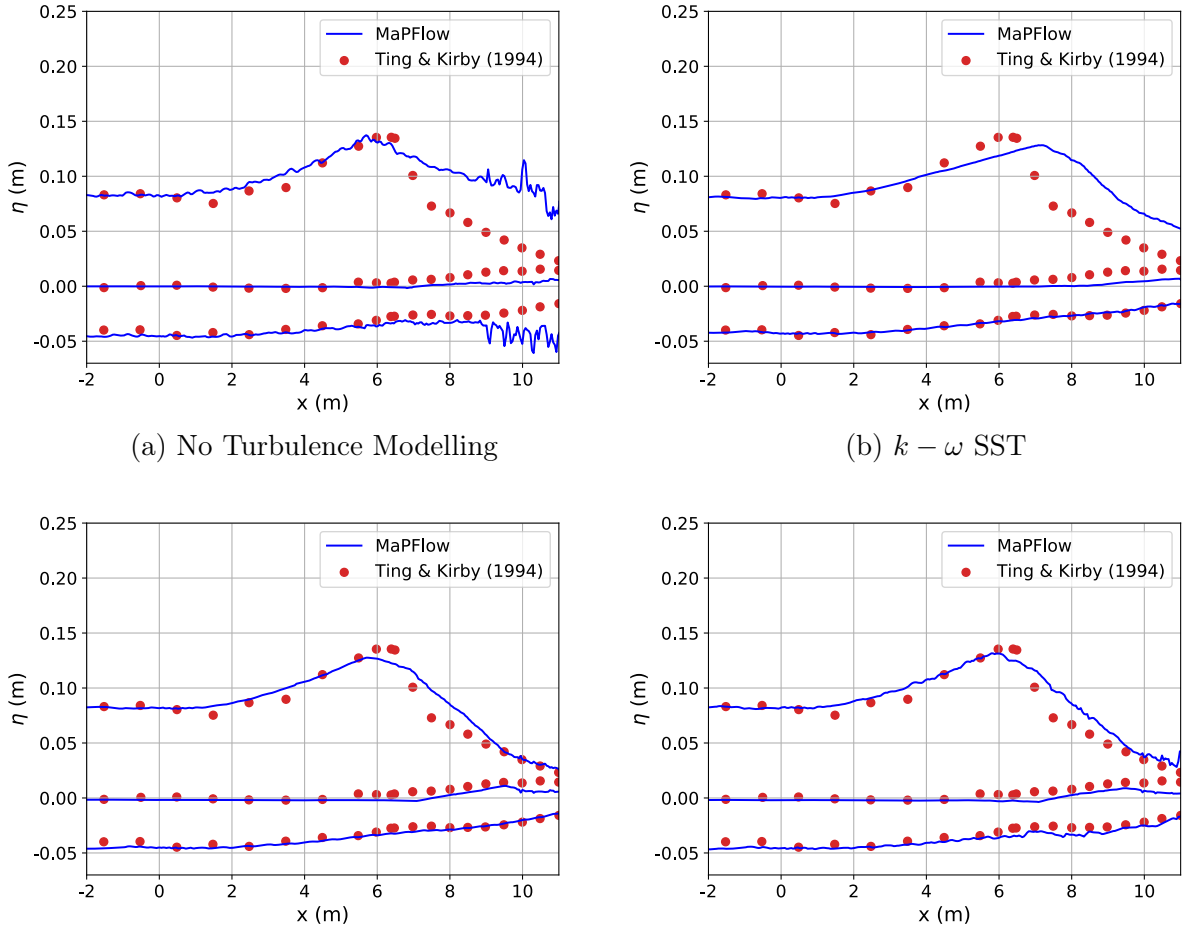

(a) No Turbulence Modelling

(b) $k-\omega$ SST

(c) Buoyancy Modified $k-\omega$ SST

(d) Stabilized $k-\omega$ SST

Figure 5.4: Time-averaged mean, maximum and minimum free surface elevations against the experimental data of Ting & Kirby for the spilling wave

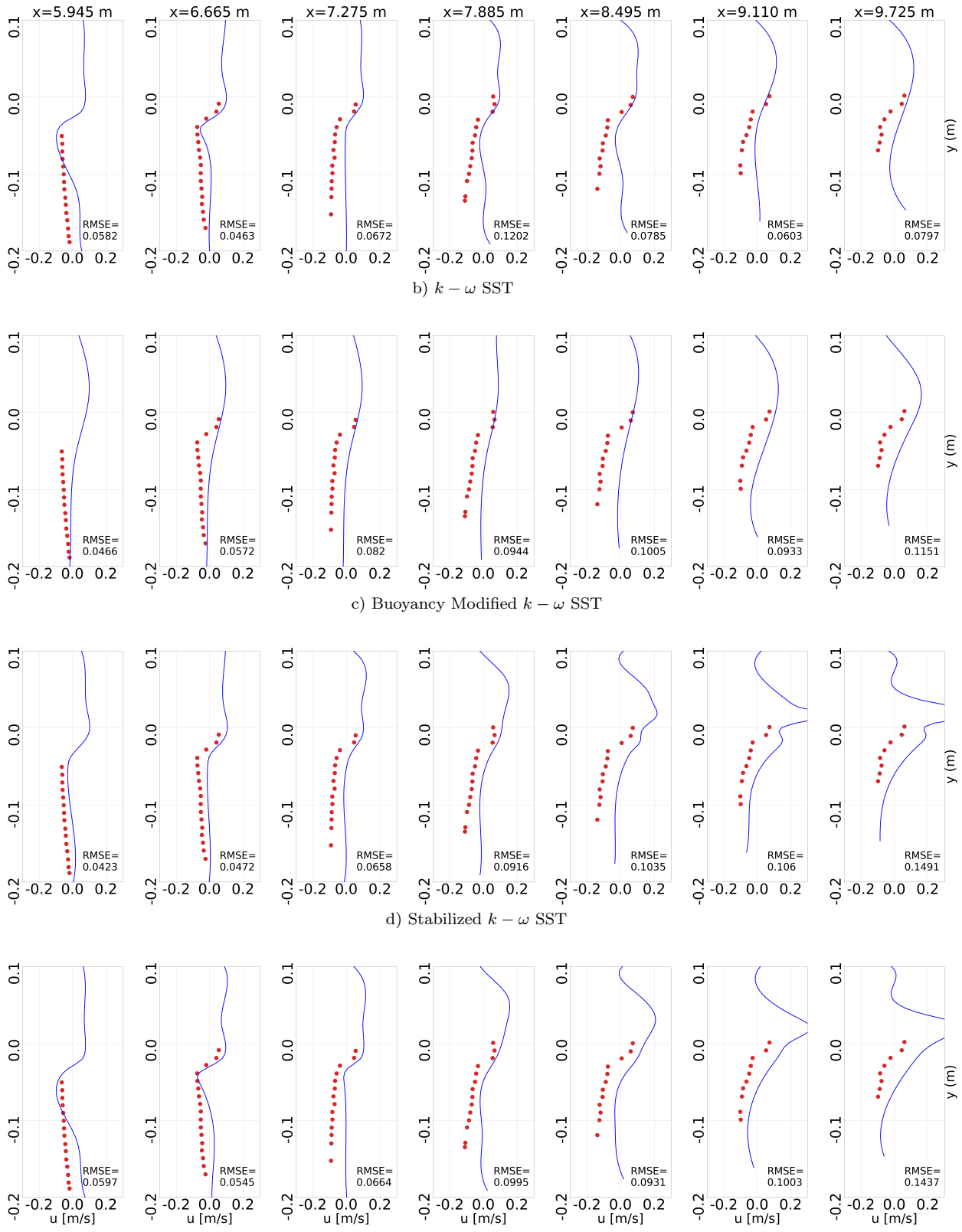

Figure 5.5: Time-averaged horizontal velocity profiles against the experimental data of Ting & Kirby for the spilling wave

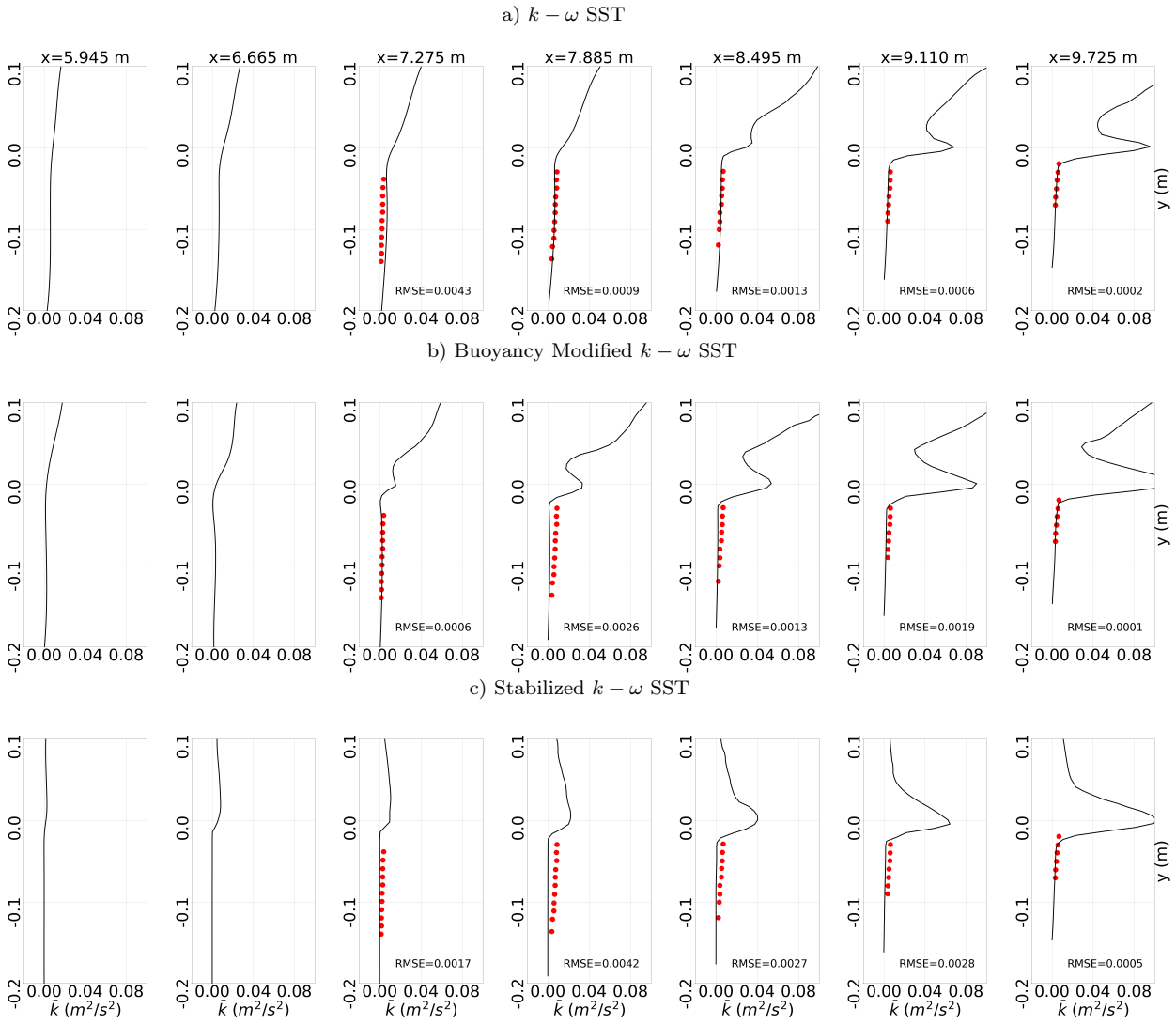

Figure 5.6: Time-averaged turbulent kinetic energy profiles against the experimental data of Ting & Kirby for the spilling wave

(a) $k - \omega$ SST

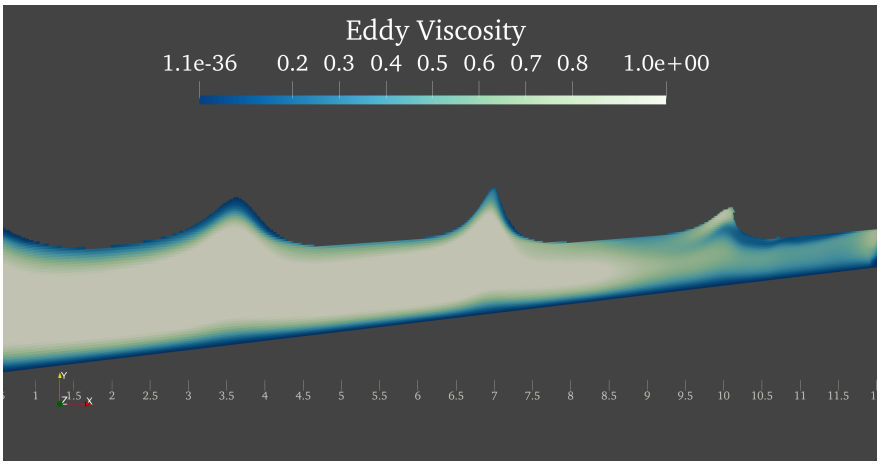

(b) Buoyancy Modified $k - \omega$ SST

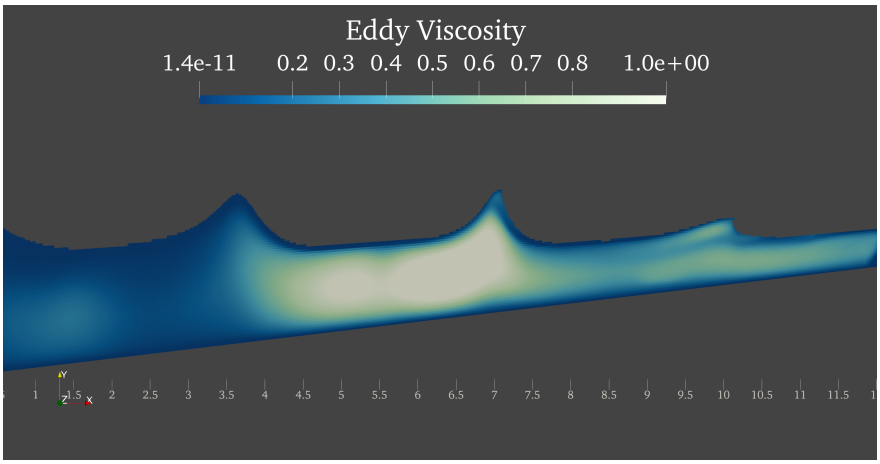

(c) Stabilized $k - \omega$ SST

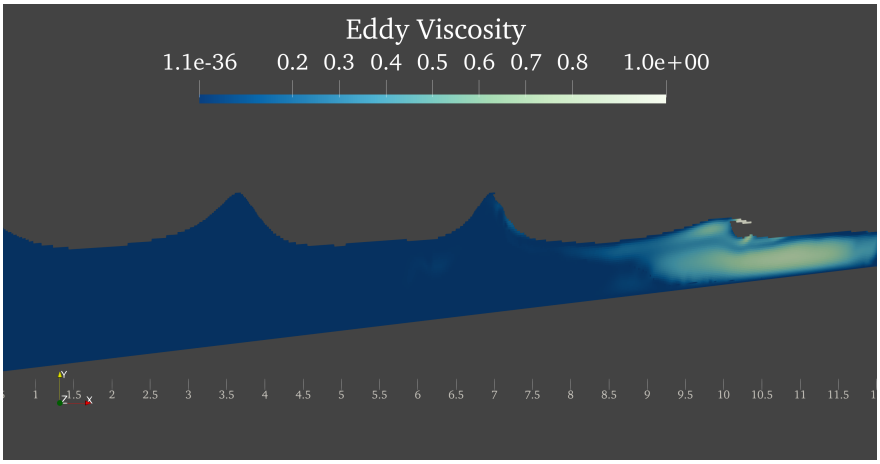

Figure 5.7: Snapshots of the eddy viscosity for the spilling wave and for the three different turbulence modelling cases

5.2.2 Plunging Breaker

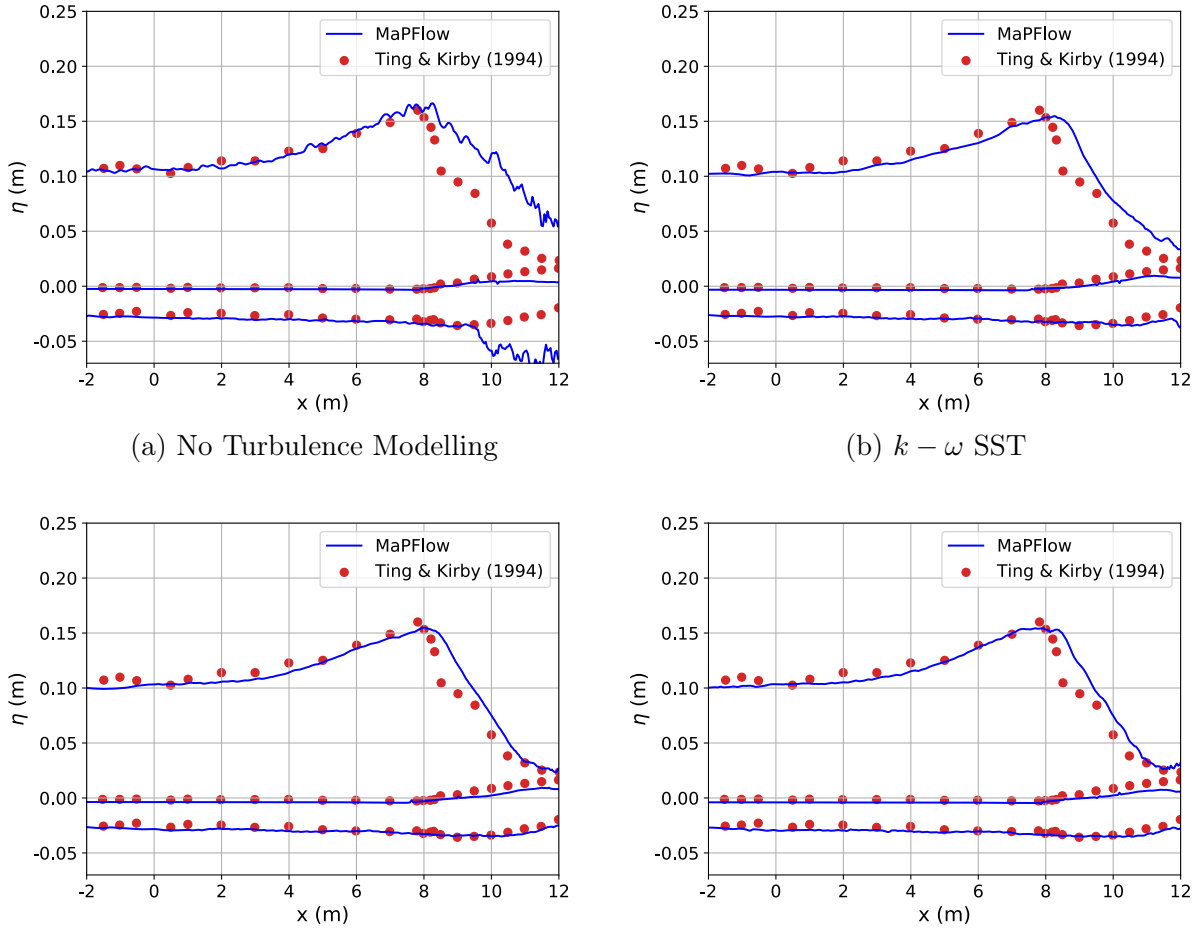

(a) No Turbulence Modelling

(b) $k-\omega$ SST

(c) Buoyancy Modified $k-\omega$ SST

(d) Stabilized $k-\omega$ SST

Figure 5.8: Time-averaged mean, maximum and minimum free surface elevations against the experimental data of Ting & Kirby for the plunging wave

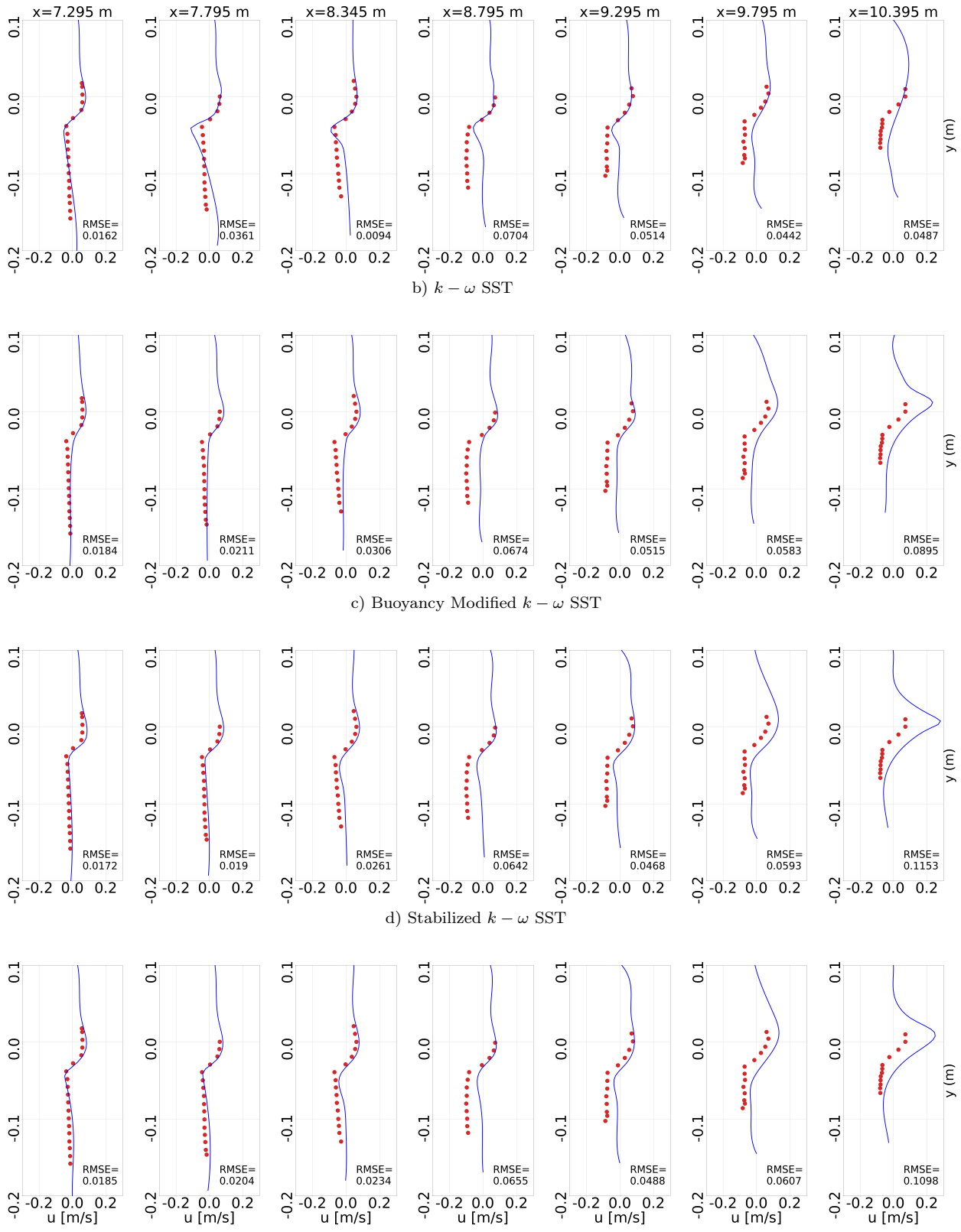

Figure 5.9: Time-averaged horizontal velocity profiles against the experimental data of Ting & Kirby for the plunging wave

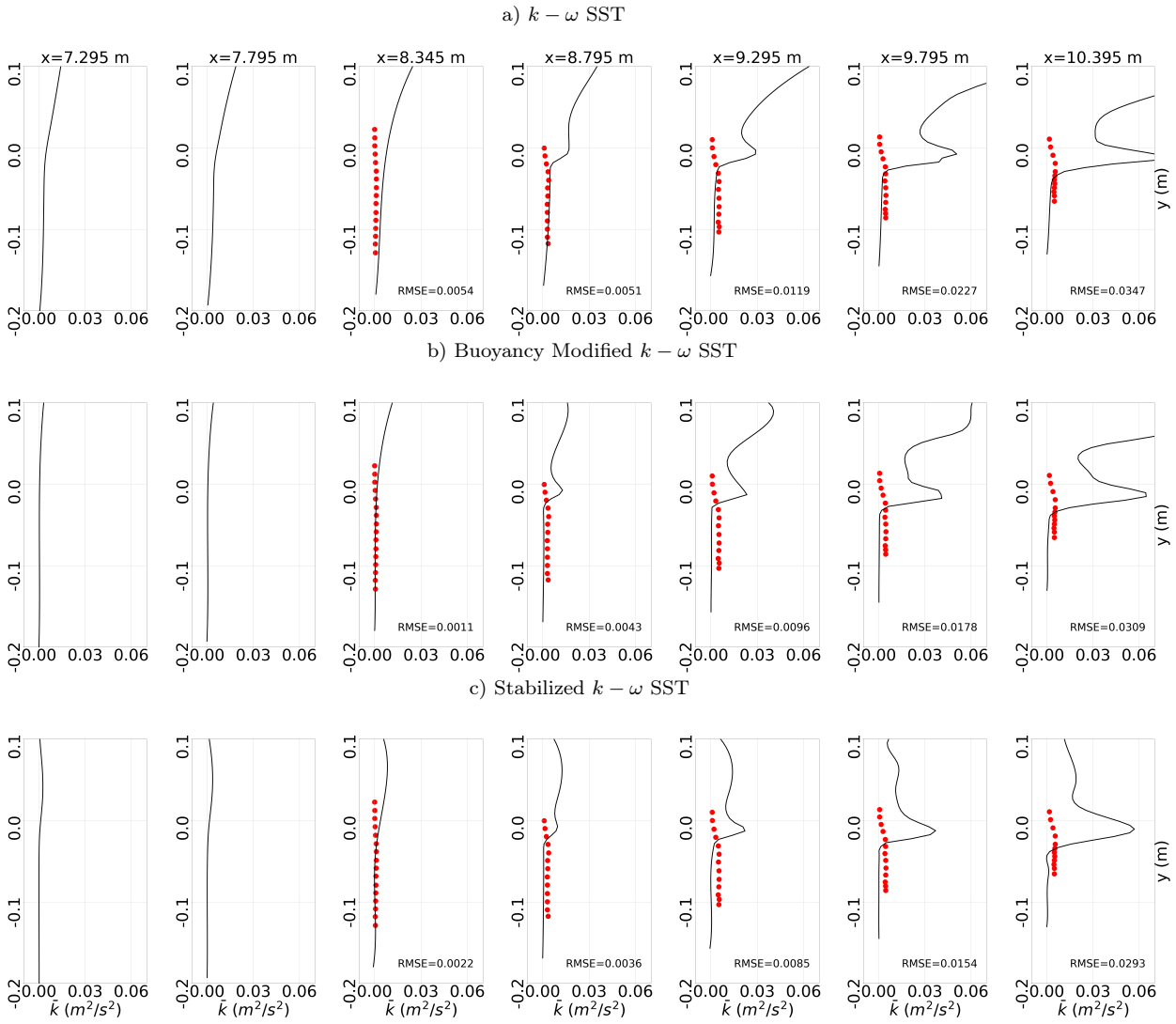

Figure 5.10: Time-averaged turbulent kinetic energy profiles agains the experimental data of Ting & Kirby for the plunging wave

(a) $k - \omega$ SST

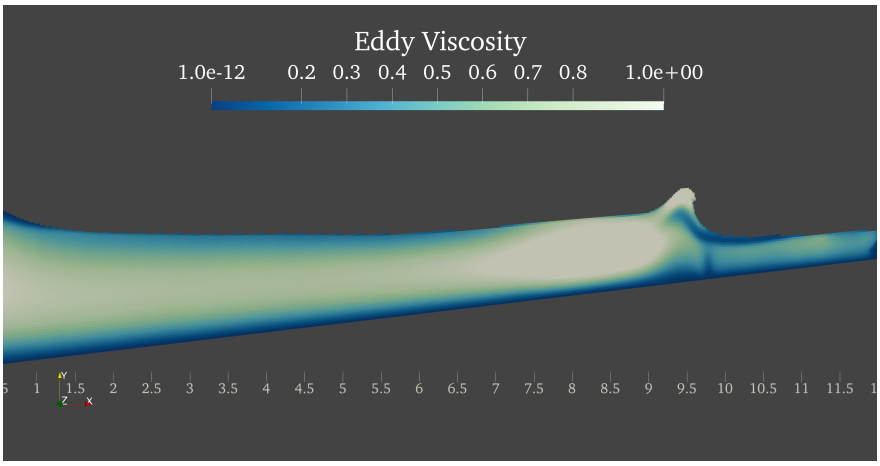

(b) Buoyancy Modified $k - \omega$ SST

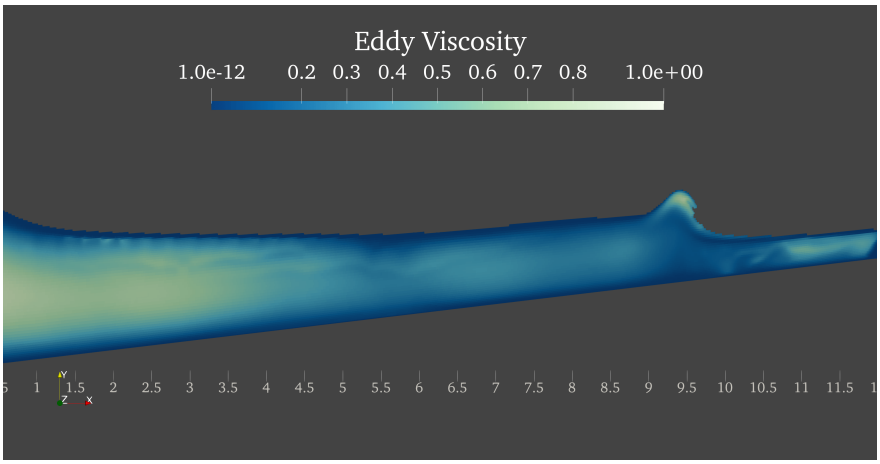

(c) Stabilized $k - \omega$ SST

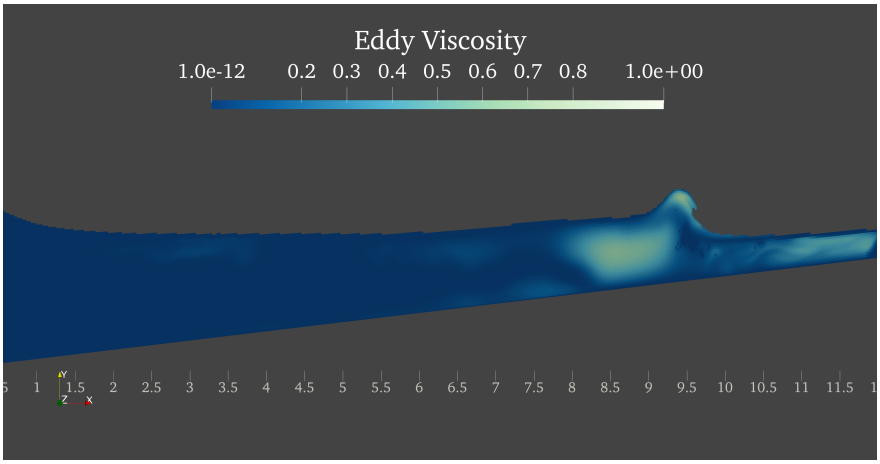

Figure 5.11: Snapshots of the eddy viscosity for the plunging wave and for the three different turbulence modelling cases

Chapter 6

Framework for Irregular Wave Generation

6.1 Irregular Waves

When studying water waves, the consideration of a wave motion that consists of components of the same frequency and height might provide significant results, but is quite idealistic and of limited practical utility. Ocean wave patterns tend to continuously change with time and space in an unrepeatable non-deterministic manner and can be either uni-directional (long-crested), where all the components are headed towards the same direction, or multi-directional (short-crested) [51]. The shape of the free surface will resemble the sinusoidal form of regular waves but each oscillation will have different height, period and thus, length. Despite this random nature of irregular sea states, their short-term variations can be described by taking the average parameters, which can be considered stationary in time, constituting a probabilistic approach to the aforementioned problem.

6.1.1 Statistical Properties

Significant representation of an irregular wave train can be provided by the simple statistical parameters of the mean and the standard deviation, derived from time series observations. It is noteworthy that the description of the sea state by statistics is quite indirect, thus there are several parameters that correspond to similar quantities. For instance, the significant wave height H_s denotes the average height of the one third of the largest wave components and is expressed as

$$H_s = \frac{1}{N/3} \sum_{j=1}^{N/3} H_j \tag{6.1}$$

where H_j is the height of the j-th component and N is the total number of waves examined [55]. However, the root mean square wave height is also defined as per below,

$$H_{rms} = \sqrt{\frac{1}{N}\sum_{j=1}^{N} H_j^2} \tag{6.2}$$

At that point, it shall be clarified that the selection of the suitable parameter to describe an irregular sea state, depends on the scope of the application. On what concerns the above pair of parameters, the root mean square height is correlated with wave energy which is also proportionate to the square of the wave height, while the significant wave height corresponds to an approximate visual estimation of the representative wave heights.

Proceeding with the period representation of irregular waves, the term is used obliquely to describe the time between two successive downward or upward zero crossings of the free-surface. The mean quantity of these is the known as the mean zero-crossing wave period and follows that

$$T_0 = \frac{1}{N}\sum_{j=1}^{N} T_j \tag{6.3}$$

Of more practical utility is the peak period and the respective mean peak period that is measured between successive peaks and in a similar manner with zero-crossing period [55].

Gaussian Water Level Distribution

The free-surface elevation field has been found to fit a Gaussian distribution [19], which, provided that the mean value of the elevations equals to zero, is given by the following expression

$$f(\eta) = \frac{1}{\sqrt{2\pi\sigma^2}} e^{-\frac{\eta^2}{2\sigma^2}} \tag{6.4}$$

where $\sigma = \sqrt{\frac{1}{N-1}\sum_{n=1}^{N}\eta_n^2}$ denotes the standard deviation of the water level $\eta(t)$.

Rayleigh Wave Amplitude Distribution

Under the conditions that the frequency range of the waves is narrow, which will be defined later as a narrow banded spectrum and the water surface elevation follows the Gaussian distribution, the wave amplitude statistics will follow a Rayleigh distribution [19] given by

$$f(A) = \frac{A}{\sigma^2} e^{-\frac{A^2}{2\sigma^2}} \tag{6.5}$$

Hence, the propability that the wave amplitude A exceeds a chosen threshold value a

can be determined as

$$P\{A > a\} = \int_a^\infty f(A)dA = e^{-\frac{a^2}{2\sigma^2}} \tag{6.6}$$

This can be also expressed in terms of wave height H as

$$P\{H > h\} = \int_h^\infty f(H)dH = e^{-2\frac{h^2}{H_s^2}} \tag{6.7}$$

In this expression, the significant wave height has been considered as $H_s = 4\sigma$ which is an important property of narrow-banded spectra and is generally satisfied quite well by sea or swell waves.

6.1.2 Wave Energy Spectrum

A fundamental approach for the analysis of irregular waves is the use of the energy spectrum in the frequency domain. The essence of this approach is based on the hypothesis that an irregular sea state can be considered as a linear superposition of each wave component that constitutes the irregular pattern. Hence, each of these components will contribute to the total energy of the wave train, in a manner that a frequency distribution of this energy will be graphically represented as the energy or the energy density spectrum. The spectral density $S(\omega_i)$ for the i-th frequency component is defined in a discrete form as

$$S(\omega_i)\Delta\omega = \frac{1}{2}A_i^2 \tag{6.8}$$

which can be multiplied by ρg to provide the energy per unit area of the waves in the frequency interval $\Delta\omega$ [51].

It is worth noticing that in the case of treating free surface displacement η as a random variable, the spectral density and autocorrelation function of η constitute a Fourier transform pair, resulting in the following relationships, widely known as the Wiener-Khintchine theorem [19]

$$\begin{aligned} S(\omega) &= \frac{2}{\pi}\int_0^\infty R(\tau)cos(\omega\tau)d\tau \\ R(\tau) &= \int_0^\infty S(\omega)cos(\omega\tau)d\omega \end{aligned} \tag{6.9}$$

Moreover, an energy density spectrum can be defined for the frequency f instead of the angular frequency ω in a way that

$$S(\omega)d\omega = S(f)df \Rightarrow 2\pi S(\omega) = S(f) \tag{6.10}$$

An important aspect of irregular wave analysis is that both measurements with respect to the time history of the free-surface elevations, as well as the energy spectrum approach are able to provide the same information about the wave pattern. The standard deviation or variance of the water surface time history is a very significant quantity in the context of this analysis, as it is a measure of the elevation's statistical spread, while it also contains information about the wave energy due to its proportionality to the square of the wave amplitude. Taking under consideration that the variance for one harmonic component is equal to $\frac{1}{2}A^2$, the area under the spectrum with respect to frequency will be equal to the variance of the sum of wave components [55] so that

$$m_0 = \sigma^2 = \int_0^\infty S(\omega) d\omega \tag{6.11}$$

In a similar fashion, spectral moments of higher order m_n can be defined so that

$$m_n = \int_0^\infty \omega^n S(\omega) d\omega \tag{6.12}$$

Hence, the mean zero-crossing and mean peak period can be reevaluated so that they follow

$$\begin{aligned} T_p &= 2\pi\sqrt{\frac{m_2}{m_4}} \\ T_0 &= 2\pi\sqrt{\frac{m_0}{m_2}} \end{aligned} \tag{6.13}$$

Another significant parameter for spectral analysis is the spectrum bandwidth, which describes the relative width of the wave energy spectrum compared to its height. To this end, wave spectra are discriminated to narrow banded and broad banded. The former type, corresponds to spectra where wave energy is concentrated in a limited range of frequencies, graphically represented by a sharp peak of the spectral density, while the latter corresponds to a flatter curve, covering a larger range of frequencies and the wave energy is spread in a more uniform manner [55]. Information about the extent of the bandwidth can be provided by the ratio of the average peak period to the average zero-crossing period, resulting in what is known in literature as the bandwidth parameter

$$\epsilon = \sqrt{1 - \frac{T_p^2}{T_0^2}} = \sqrt{1 - \frac{m_2^2}{m_0 m_4}} \tag{6.14}$$

Values near to $\epsilon \approx 0$ correspond to very narrow-banded spectra and mean that $T_p \approx T_0$, while $\epsilon \approx 1$ corresponds to wide banded spectra. The spectrum bandwidth is of major importance, since it is a measure of the irregularity of the wave pattern. In particular, a narrow-banded spectrum means that the frequency of all the wave components converge

towards a single frequency, meaning that the wave pattern is nearly regular.

JONSWAP Wave Spectra

Several parametric wave spectra can be found in literature, which have a standardized formulation depending only on specific parameters. One of the most commonly used spectra is the JONSWAP (Joint North Sea Wave Project) developed during the homonymous international research program by Hasselman [56]. This bi-parametric model is used to describe uni-directional partially developed and fetch limited sea states and is defined as

$$S(\omega) = \frac{5}{16} H_s^2 \omega_p^4 \omega^{-5} e^{-\frac{5}{4}(\frac{\omega}{\omega_p})^{-4}} \gamma^{e^{\frac{-(\omega-\omega_p)^2}{2\sigma^2\omega_p^2}}} A_\gamma \tag{6.15}$$

where ω is the angular frequency over which the spectral density $S(\omega)$ is distributed, H_s is the significant wave height, $\omega_p = \frac{2\pi}{T}$ is the peak angular frequency, $\gamma = 3.3$ is the peak enhancement factor, $A_\gamma = 1 - 0.287\ln\gamma$ and $\sigma = 0.07$ for $\omega < \omega_p$ or $\sigma = 0.09$ for $\omega > \omega_p$.

6.1.3 Welch's Method for Spectral Density Estimation

A prerequisite of the spectral analysis described above is the conversion of the acquired time series data to the equivalent spectrum. In the present work this process is carried out using the Welch's Method [57], an extension of Fast Fourier Transform (FFT), that eliminates noise and provides more smooth frequency spectrum than the raw FFT output, with the exchange of frequency resolution reduction. The Welch algorithm is a nonparametric method for the estimation of the spectral density and is an improvement of the standard periodogram method and Bartlett's method. In the context of this approach, the signal's time domain is separated in windows of equal length and this windowing process leads to cutting off the harmonics with period larger than the extend of the window. Each window overlaps the adjacent ones by a certain factor, which may reach 50% of the window's size and in that way the loss of information due to tapering of the signal at the interval's edges is reduced. The main feature of this process is that it eliminates sharp transitions, that cause disturbances and thus, provides a smoother spectrum representation.

Considering a discrete time signal s which is constituted by N samples will be

$$s = x[1], x[2], ..., x[N] \tag{6.16}$$

This signal can be further discretized in K intervals with length M and overlapping V. Under this scope, the windows s_i will be expressed as per below

$$
\begin{aligned}
s_1 &= x[1], x[2], ..., x[M] \\
s_2 &= x[M-V+1], x[M-V+2], ..., x[2M-V] \\
s_K &= x[(K-1)M-(K-1)V+1], ..., x[KM-(K-1)V]
\end{aligned} \tag{6.17}
$$

The DFT will provide for each window

$$
S_i[v] = \sum_{m=1}^{M} s_i[m] w[m] e^{-\frac{2\pi j m v}{N_F}}, \qquad 1 \leq v \leq N_F \tag{6.18}
$$

where $w = \{w[1], w[2], ..., w[M]\}$ is the windowing vector, N_F is the DFT size and $S_i = \{S_i[1], S_i[2], ..., S_i[N_F]\}$ is the frequency samples' vector for the i-th window. Following, the periodogram values will be

$$
P_i[v] = \frac{1}{C} \left| S_i[v] \right|^2, \qquad 1 \leq v \leq N_F \tag{6.19}
$$

where $C = \sum_{m=1}^{M} w^2[m]$ being the normalization factor. These periodogram values from different windows are averaged and the spectral density is estimated as

$$
SD(v) = \frac{1}{K} \sum_{i=1}^{K} P_i[v], \qquad 1 \leq v \leq N_F \tag{6.20}
$$

6.2 Irregular Wave Generation Method

The general principle of the irregular wave generation in *MaPFlow* is the implementation of a reverse spectral analysis process and the construction of the corresponding time histories by adding a large number of wave components. For the representation of these components, the Airy Wave Theory is used, considering that the free surface elevation is a linear superposition of the regular wave components such that

$$
\eta(x,t) = \sum_{i=1}^{N} A_i cos(k_i x - \omega_i t + \epsilon_i) \tag{6.21}
$$

where index i denotes each wave component in a way that its frequency ω_i is the i-th frequency of the discretized energy spectrum. Its wavenumber $k_i = \frac{2\pi}{\lambda_i}$, is determined by solving the dispersion equation, whereas its amplitude, according to the definition of the energy spectrum follows

$$
A_i = \sqrt{2 S_i(\omega) \Delta\omega} \tag{6.22}
$$

where the term S_i denotes the spectral density of the wave component and corresponds to the i-th component of the discretized spectrum, similarly with the frequency. It is important to consider that two generated irregular wave patterns, derived from the same spectrum, that have a different distribution of phase angles will have a different free-surface elevation field but will contain the same amount of energy.

Thus, the horizontal and vertical velocity will be respectively

$$u(x,z,t) = \sum_{i=1}^{N} A_i \omega_i \frac{cosh[k_i(z+h)]}{sinh(k_i h)} cos(k_i x - \omega_i t + \epsilon_i) \tag{6.23}$$

$$w(x,z,t) = \sum_{i=1}^{N} A_i \omega_i \frac{sinh[k_i(z+h)]}{sinh(k_i h)} sin(k_i x - \omega_i t + \epsilon_i) \tag{6.24}$$

Also, the corresponding pressure field will follow

$$p(x,z,t) = \sum_{i=1}^{N} \rho g A_i \frac{cosh[k_i(z+h)]}{cosh(k_i h)} cos(k_i x - \omega_i t + \epsilon_i) \tag{6.25}$$

6.3 Free Surface Reconstruction Algorithm (FSRA)

As mentioned in the previous section, irregular wave patterns that have been derived from the same spectrum, but have difference phase angles over their frequency components, will lead to different time histories, although they will have the same amount of wave energy. In order to be able to reproduce a free surface elevation profile, as accurately as possible, the Free Surface Reconstruction Algorithm in its linear formulation, as developed by Grilli et al. [58] has been implemented and is presented below.

Considering that the irregular free surface $\eta(x,t)$ is the superposition of the elevations of N linear wave components and substituting the Fourier coefficients $a_n = A_n cos\phi_n$, $b_n = A_n sin\phi_n$ the expression will be

$$\eta_N(x,t) = \sum_{n=1}^{N} a_n cos\Psi_n + b_n sin\Psi_n \tag{6.26}$$

where $\Psi_n = k_n x - \omega_n t$ are the harmonic phases

In order to minimize the difference between the reproduced η_N and the desired η_l, a Least Square Method is applied through a cost function

$$C = \frac{1}{N}(\eta_N(x,t) - \eta_l)^2 \tag{6.27}$$

To reach an extremum of this function, the following condition shall be satisfied

$$\frac{\partial C}{\partial a_n} = 0 \qquad \frac{\partial C}{\partial b_n} = 0 \tag{6.28}$$

This results to a system of equations as per below

$$\begin{aligned} \sum_{l=1}^{L}\sum_{n=1}^{N} a_n cos\Psi_{nl} cos\Psi_{nl} + b_n cos\Psi_{nl} sin\Psi_{nl} &= \sum_{l=1}^{L} \eta_l cos\Psi_{nl} \\ \sum_{l=1}^{L}\sum_{n=1}^{N} a_n sin\Psi_{nl} cos\Psi_{nl} + b_n sin\Psi_{nl} sin\Psi_{nl} &= \sum_{l=1}^{L} \eta_l sin\Psi_{nl} \end{aligned} \tag{6.29}$$

This system of $2N$ equations with $2N$ unknown variables can be rewritten in matrix form

$$A_{nn} X_n = B_n \tag{6.30}$$

where $X_n = [a_1, ..., a_N, b_1, ..., b_N]$ is the $2N$ vector of unknown variables and B_n is

$$B_n = \begin{cases} \sum_{l=1}^{L} \eta_l cos\Psi_{nl}, & 1 < n \leq N \\ \sum_{l=1}^{L} \eta_l sin\Psi_{nl}, & N+1 \leq n \leq 2N \end{cases} \tag{6.31}$$

Moreover, A_{nn} is the $2N \times 2N$ matrix where,

$$\begin{aligned} A_{n,n} &= \sum_{l=1}^{L} cos\Psi_{nl} cos\Psi_{nl} \\ A_{n,n+N} &= \sum_{l=1}^{L} cos\Psi_{nl} sin\Psi_{nl} \\ A_{n+N,n} &= \sum_{l=1}^{L} sin\Psi_{nl} cos\Psi_{nl} \\ A_{n+N,n+N} &= \sum_{l=1}^{L} sin\Psi_{nl} sin\Psi_{nl} \end{aligned} \tag{6.32}$$

Solution of the aforementioned system provides a set of parameters a_n, b_n which can fully reproduce the free-surface time history under consideration. At this point, it should be mentioned that the method is also applicable for reconstruction of elevation profiles with

respect to spatial coordinates, but in the present study only the water surface elevation with respect to time has been examined.

6.4 Model Validation

6.4.1 Numerical Setup

In this section, the framework for the generation of irregular waves described above, is validated through the generation and propagation of waves derived from a JONSWAP-type spectrum over a flat bed. To this end, the numerical wave tank shown in Fig. 6.1 was constructed and a spectrum of peak period $T_p = 2\ s$ and significant height $H_s = 0.018\ m$ was considered. This choice was based on the need for small free-surface elevations, so that the non-linearity of the wave pattern is weak and the comparison with the analytical results is feasible. Moreover, the determination of the exact spectrum and the wave components that will be imported in the numerical wave tank at a pre-processing stage, allows an estimation of the characteristics of these waves. Thus, the extent of the generation and damping zone was chosen to coincide with the largest wavelength, among the generated wave components. For the evaluation of the model, 4 stations were placed inside the tank in the following positions: $x_{WG1} = 5\ m$, $x_{WG2} = 10\ m$, $x_{WG3} = 15\ m$, $x_{WG4} = 20\ m$. The first gauge is placed inside the generation zone, in order to provide an insight on whether the irregular wave is generated accurately. The reason of setting multiple gauges in the domain is to assess the amount of spectral energy that is lost due to numerical diffusion, with respect to the x coordinate.

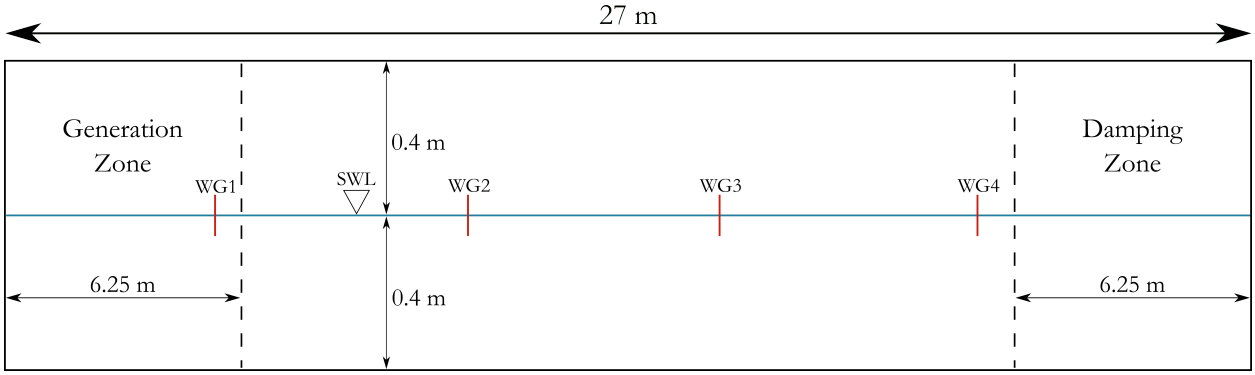

Figure 6.1: Configuration of the numerical wave tank for the irregular wave propagation case

Three grid resolutions of ascending order were considered, the features of which, as well as their correlation with the generated waves is shown in Table 6.1. The term λ_p denotes the wavelength of the wave which has a period of $T = T_p$ and amplitude of $A = \sqrt{2S(\omega_p)\Delta\omega}$. It is chosen as a benchmark, since most of the generated waves that contain a significant amount of energy, have similar characteristics.

	Nodes	dx (m)	Cells per H_s	Cells per λ_p
G1	49000	0.040	7	470
G2	105000	0.030	12	647
G3	226000	0.015	18	1177

Table 6.1: Grid resolutions for irregular wave propagation case

The grid sensitivity study was carried out with a timestep of $dt = T_p/800$, as an extension of the conclusion of Chapter 4 about the timestep of regular waves and considering that most of the generated wave components are concentrated at this area at the frequency spectrum. Moreover, the duration of the simulation was set to $150T_p = 375\ s$ and the number of wave components, to which the frequency spectrum was divided and were superposed to provide the irregular pattern was $N = 100$. Regarding the effect of the grid resolution, the time histories of the free-surface elevation at the four wave gauges are presented in Fig. 6.2 and the corresponding spectrum representations in Fig. 6.3. It may be concluded that the free-surface profiles for the three grids are quite similar and they are in a very good agreement with the analytical elevations, as they are predicted from the Linear Theory. The effect of numerical diffusion is clear in gauges $WG3$ and $WG4$, where deviations are observed in the crests and troughs of the wave and they are more widespread than $WG1$ and $WG2$, where these deviations exist due to non-linear effects.

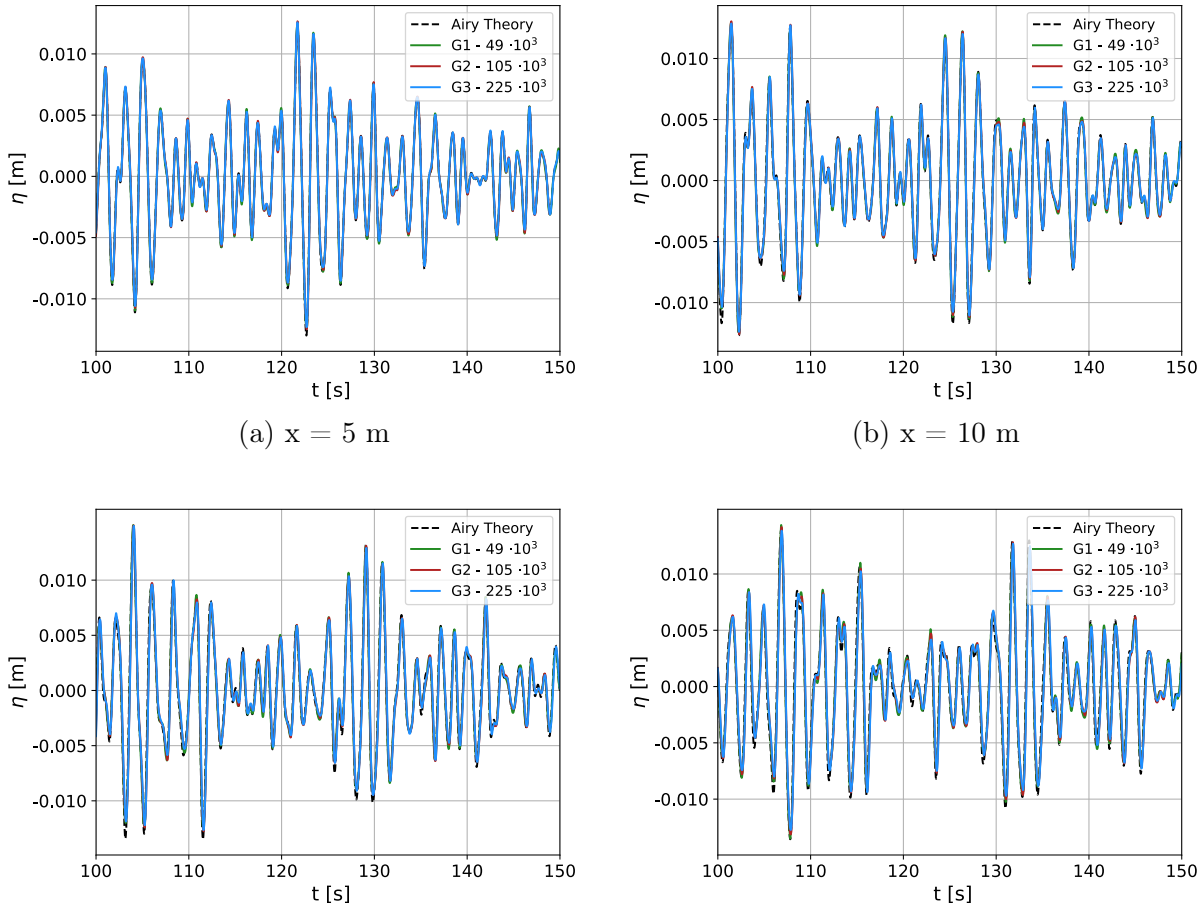

(a) x = 5 m

(b) x = 10 m

(c) x = 15 m

(d) x = 20 m

Figure 6.2: Free surface elevation profiles for grid resolutions $G1, G2, G3$ against the analytical solution from Linear Wave Theory

On what concerns the comparison of the spectrum, that was obtained by applying the Welch method to the time histories of the aforementioned wave gauges, the impact of grid resolution is greater. Surprisingly, the coarser mesh $G1$ captures quite well the area of maximum spectral densities in comparison with the others, but shows larger deviation of the simulated peak period with the imported. For the grid of medium resolution $G2$, the peak period also diverges from the target and seems to overestimate the spectral density of frequencies slightly higher than the peak's. Finally, $G3$ seems to capture quite well the distribution of spectral energy to the imported frequency range, with the exception of the peak frequency area.

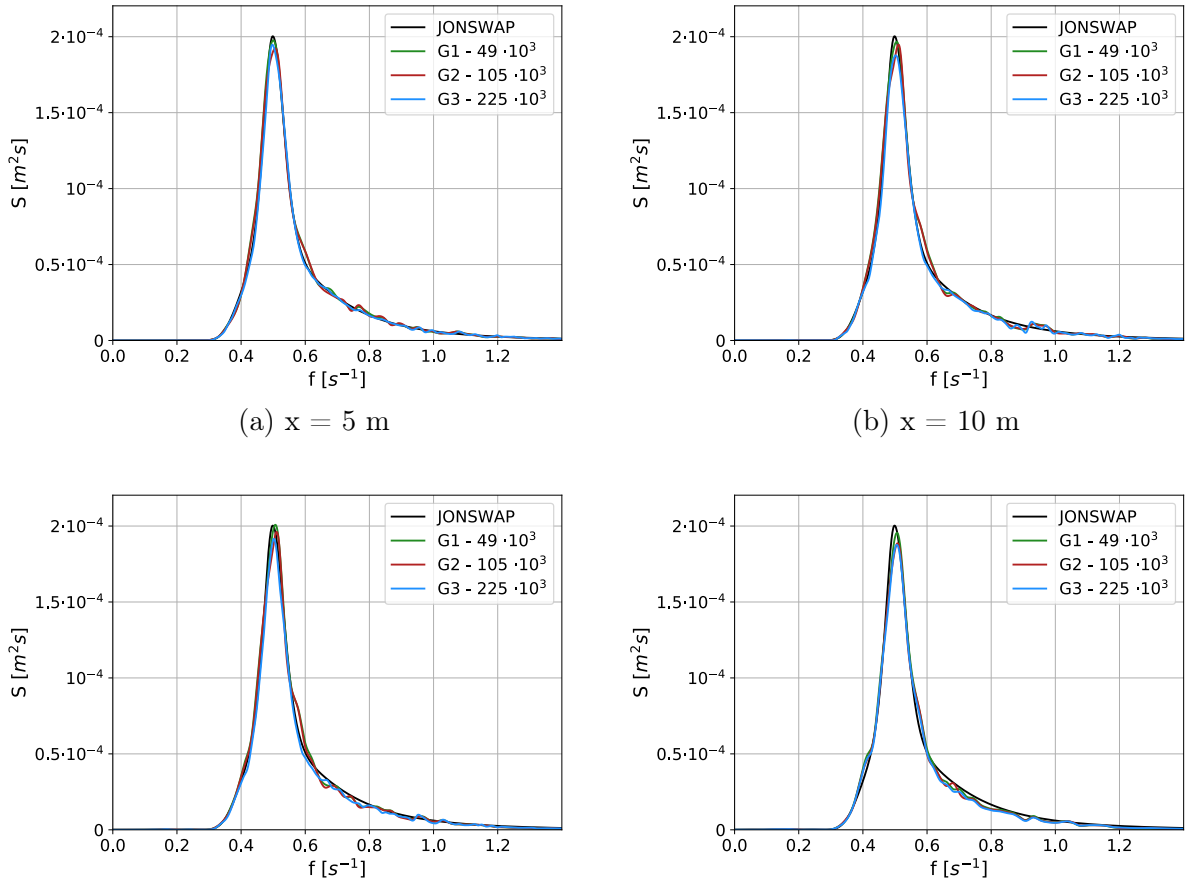

(a) x = 5 m

(b) x = 10 m

(c) x = 15 m

(d) x = 20 m

Figure 6.3: Wave energy density spectra for grid resolutions $G1, G2, G3$ against JONSWAP

The mesh $G3$ was considered to provide the best results for the representation of the irregular wave both in the time and the frequency domain. Hence, the simulation was conducted again for that grid and for $dt = T_p/400$ and $dt = T_p/1600$, in order to assess the influence of the timestep selection in correlation with the spectrum's main parameters. In Fig. 6.4 and 6.5 the free surface elevations and frequency spectra for the timestep sensitivity study respectively are presented. Regarding the elevation profiles, the largest timestep of $T_p/400$ fails to capture dispersive phenomena of the irregular wave, resulting in a gradual offset of the elevation against the analytical solution. Between, the other two examined timesteps, the differences are negligible and they can be considered of equivalent accuracy.

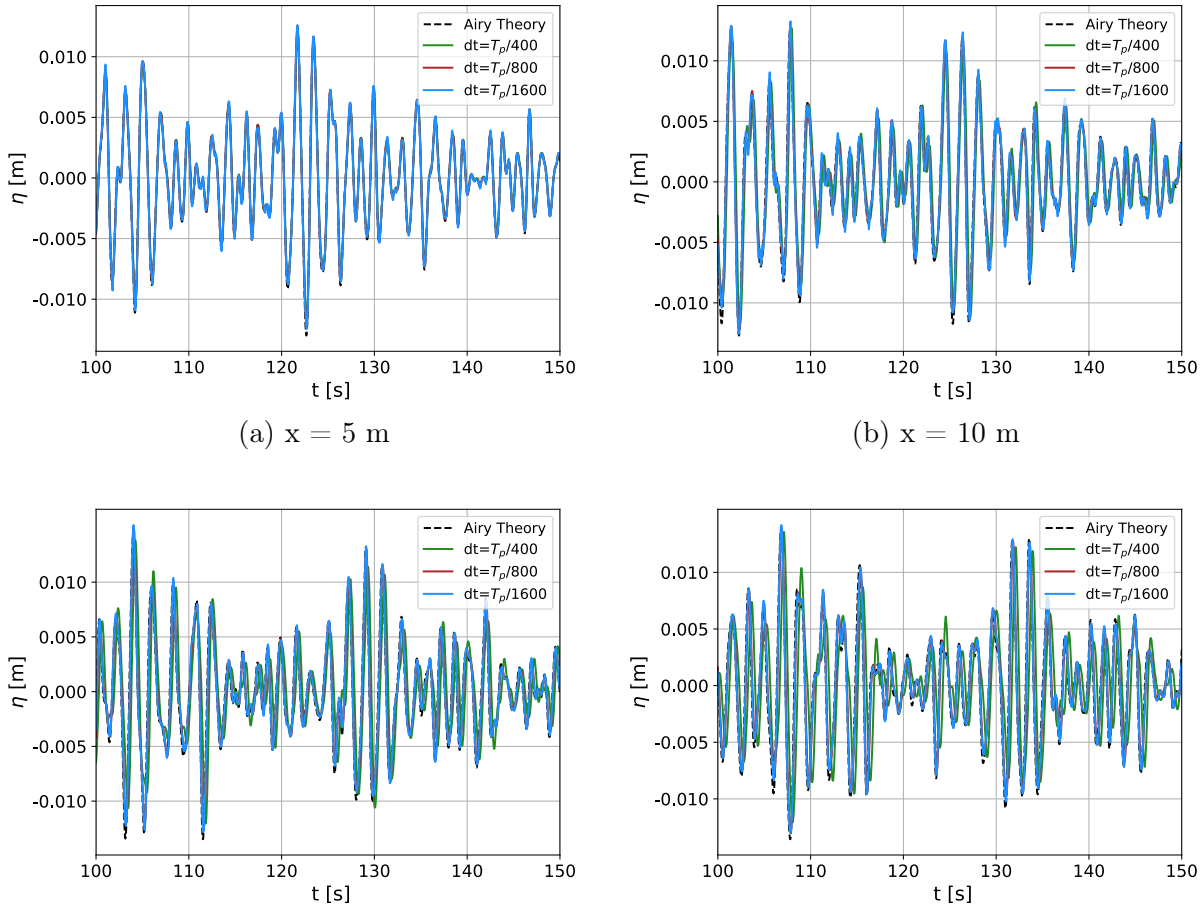

(a) x = 5 m

(b) x = 10 m

(c) x = 15 m

(d) x = 20 m

Figure 6.4: Free surface elevation profiles for timesteps $dt = T_p/400, T_p/800, T_p/1600$ against the analytical solution from Linear Wave Theory

Proceeding to the spectral evolution of the wave during its propagation, the inadequacy of $dt = T_p/400$ is evident, since it provides far less accurate results than the others. Regarding the other two cases, their difference in the quality of results in the frequency domain is again of little importance, with the denser time discretization providing a slightly more accurate spectral representation in the area of the peak frequency.

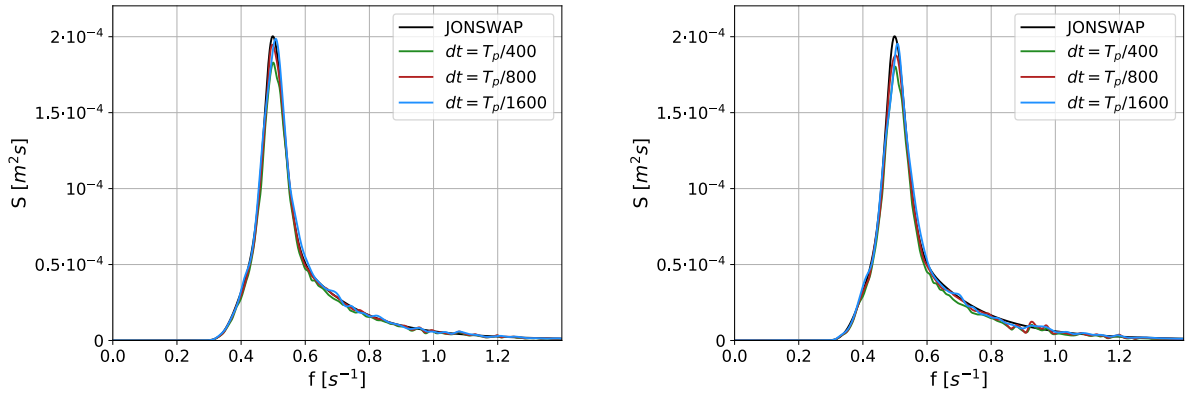

(a) x = 5 m (b) x = 10 m

(c) x = 15 m (d) x = 20 m

Figure 6.5: Wave energy density spectra for timesteps $dt = T_p/400, T_p/800, T_p/1600$ against JONSWAP

From the preceding analysis, the selected numerical setup to continue the analysis, is selected to be for the mesh resolution $G3$ and a timestep of $dt = T_p/800$. In the next subsections, the influence of parameters such as the number of wave components to which the imported frequency spectrum is divided, as well as the length of the simulation, is investigated. These parameters might not be directly correlated with the numerical model by itself, but are of crucial importance on what concerns the transition from the time to frequency domain through Welch method. For this reason, several cases are considered with a wave components' number of ascending order and then for $N = 100$ the spectral representations, derived from simulations of different length are compared.

6.4.2 Effect of number of wave components

In Fig. 6.6, 6.8, 6.10 and 6.12 the spectral representations, at the different stations of the numerical wave tank and for $N = 25, 50, 100$ and 200 respectively are illustrated. The deviation between the simulated significant wave height, calculated as $H_s = 4\sqrt{m_0} = 4\sqrt{\sum_{i=0}^{N} S(\omega_i)\Delta\omega}$ and the imported, as well as the corresponding peak period values are presented in Fig. 6.7, 6.9, 6.11 and 6.13 for the aforementioned wave component numbers.

It can be noticed that for $N = 25$, the deviations at the peak frequency are significantly intensified as the wave propagates, a problem which is eliminated for $N = 50$ and $N = 100$. These two cases, present both very good agreement with the imported spectrum, while for $N = 200$ disturbances are caused to the spectral representation, even after applying the Welch's method. This problem, was not solved for various windowing length values and might be caused by the existence of a lot of independent frequencies, which is difficult to capture and filter effectively, as well as of several components with a period slightly lower than the windowing length, that cause those disturbances. Moreover, the evolution of the numerical wave height and peak period show relatively small discrepancies with the JONSWAP's values and as expected, there is a general tendency for these discrepancies to increase along with the increase of the propagated distance.

For the spectral estimation, it occurred that the optimal window length depends strongly on the number of propagating wave components and was found to be proportional of it. Hence in order to obtain a smooth spectrum, when having a large number of N, an also large window will be necessary. As it will be discussed in the next subsection, this length is influenced strongly by the length of the simulation apart from this parameter. It should be also noted that the increase in number of generated waves causes an appreciable increase in the computational cost, for which quantitative data can be found in Table 6.2.

N	Duration (h)
25	17.7
50	21.1
100	26.8
200	39.0

Table 6.2: Simulation run-time for wave components number of $N = 25, 50, 100, 200$

Thus, the conclusion that can be drawn from this discussion is that the wave components that are generated are of crucial importance regarding both the simulation, due to the direct influence on computational cost, as well as the influence on the quality of the provided wave spectrum. For the present work, $50 - 100$ wave components are considered to be the most efficient and effective choice, with a frequency interval of $\Delta f \approx 0.012$.

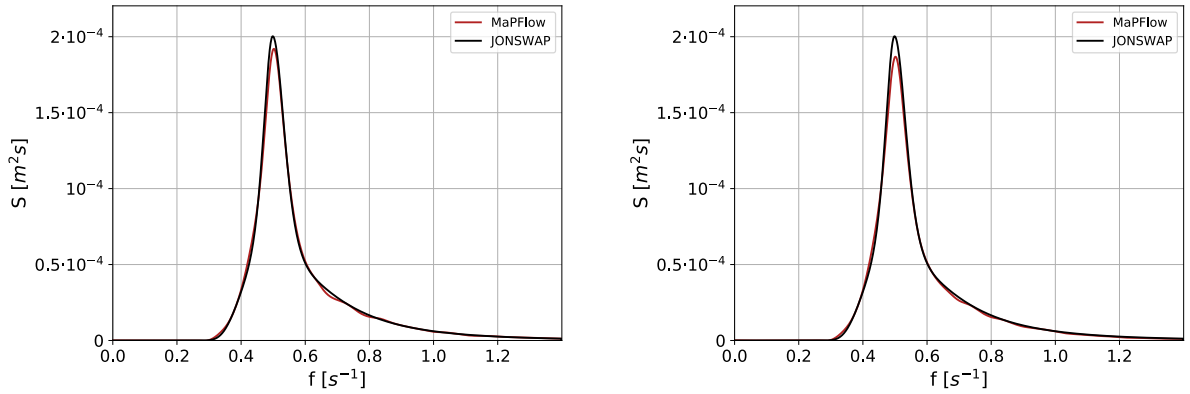

(a) x = 5 m

(b) x = 10 m

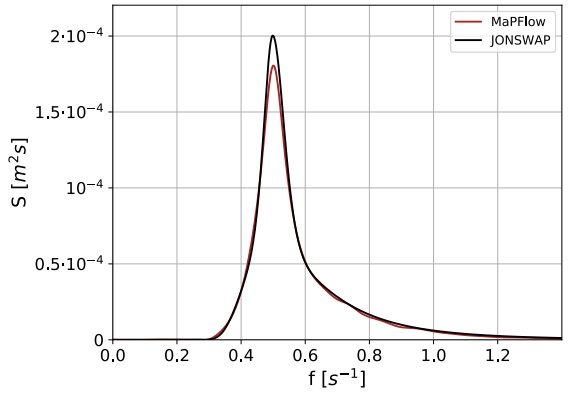

(c) x = 15 m

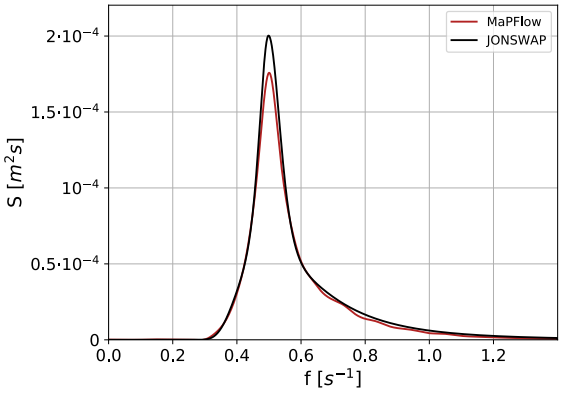

(d) x = 20 m

Figure 6.6: Wave energy density spectra for a wave component number of $N = 25$

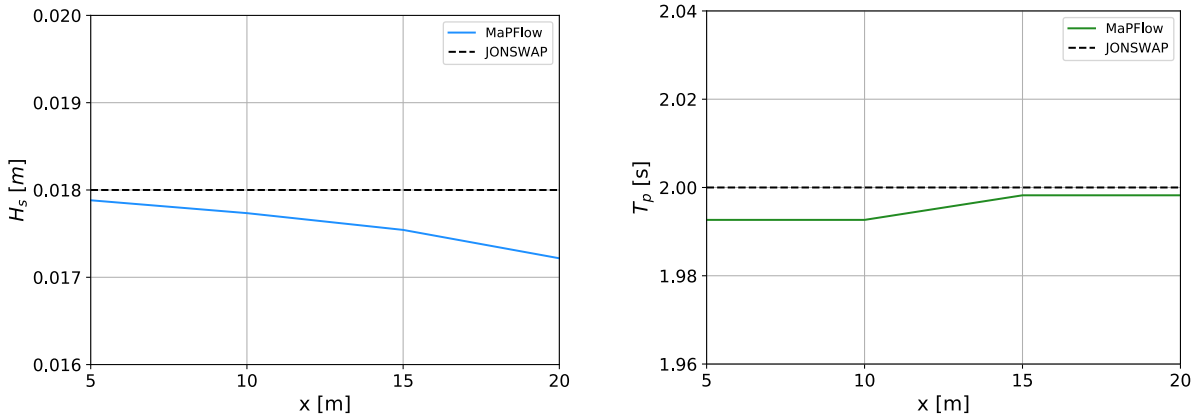

Figure 6.7: Evolution of significant wave height (left) and peak period (right) for a wave component number of $N = 25$

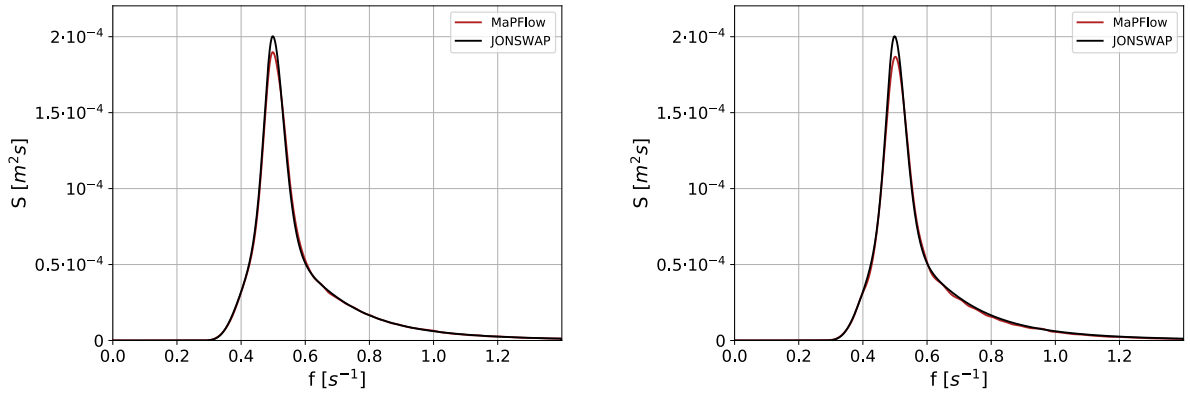

(a) x = 5 m

(b) x = 10 m

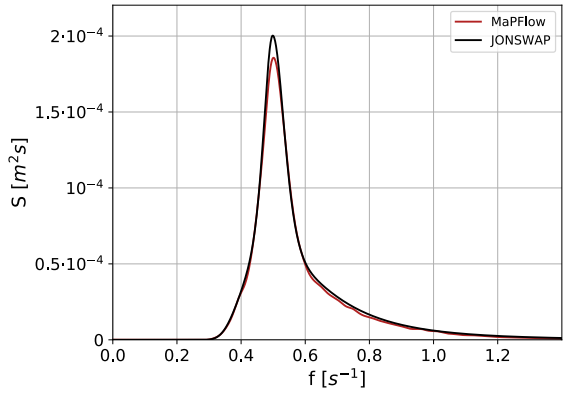

(c) x = 15 m

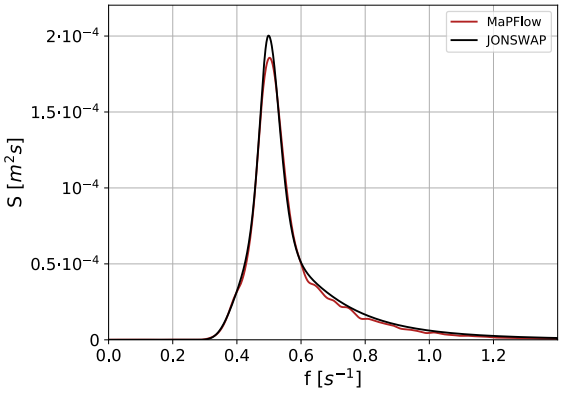

(d) x = 20 m

Figure 6.8: Wave energy density spectra for a wave component number of $N = 50$

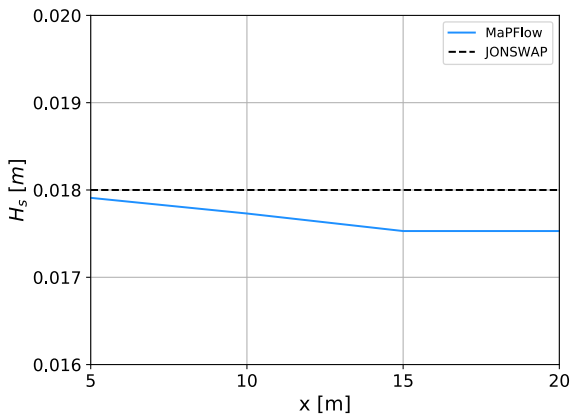

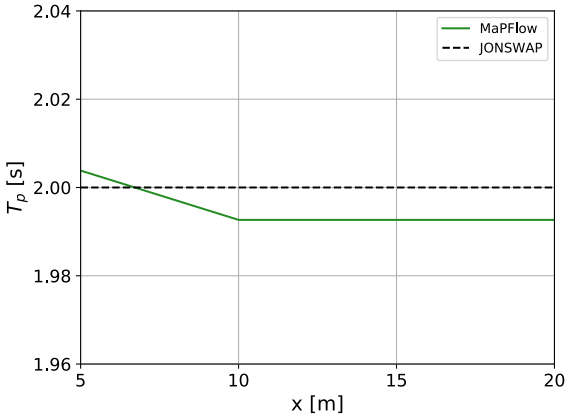

Figure 6.9: Evolution of significant wave height (left) and peak period (right) for a wave component number of $N = 50$

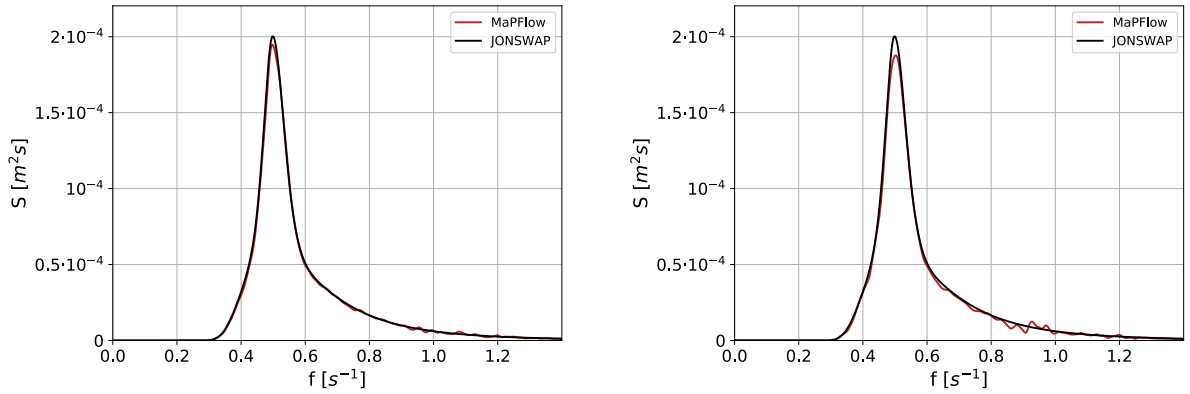

(a) x = 5 m

(b) x = 10 m

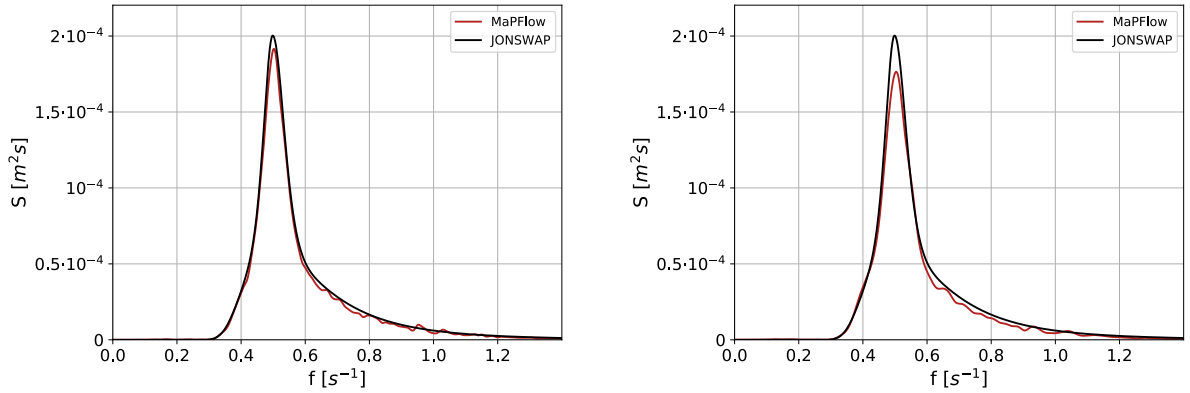

(c) x = 15 m

(d) x = 20 m

Figure 6.10: Wave energy density spectra for a wave component number of $N = 100$

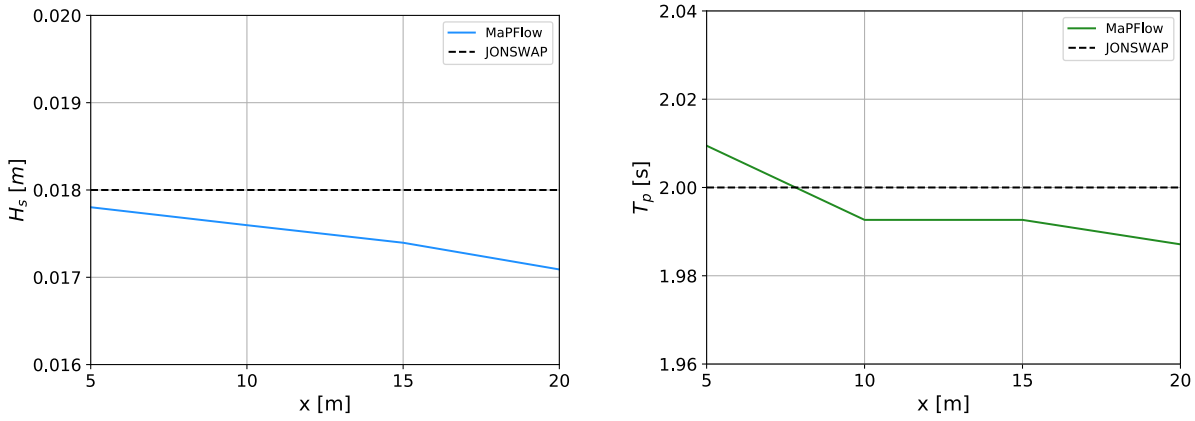

Figure 6.11: Evolution of significant wave height (left) and peak period (right) for a wave component number of $N = 100$

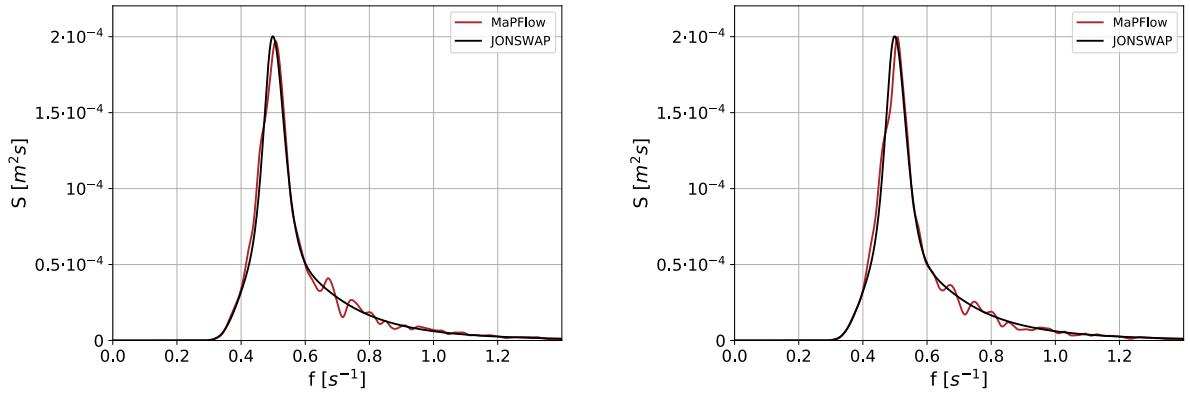

(a) x = 5 m

(b) x = 10 m

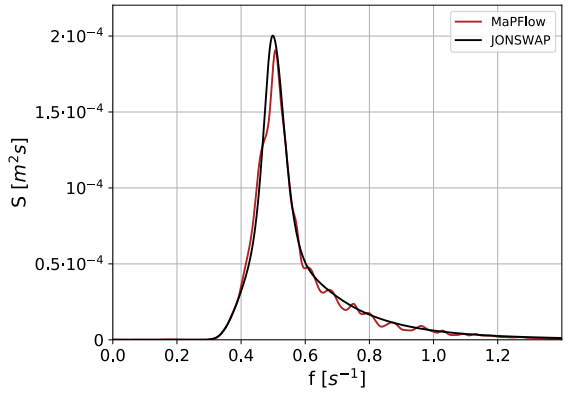

(c) x = 15 m

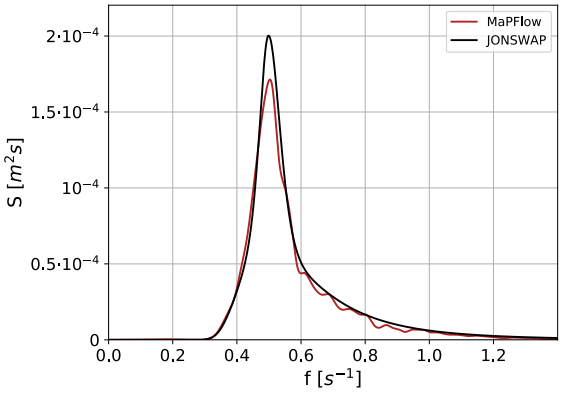

(d) x = 20 m

Figure 6.12: Wave energy density spectra for a wave component number of $N = 200$

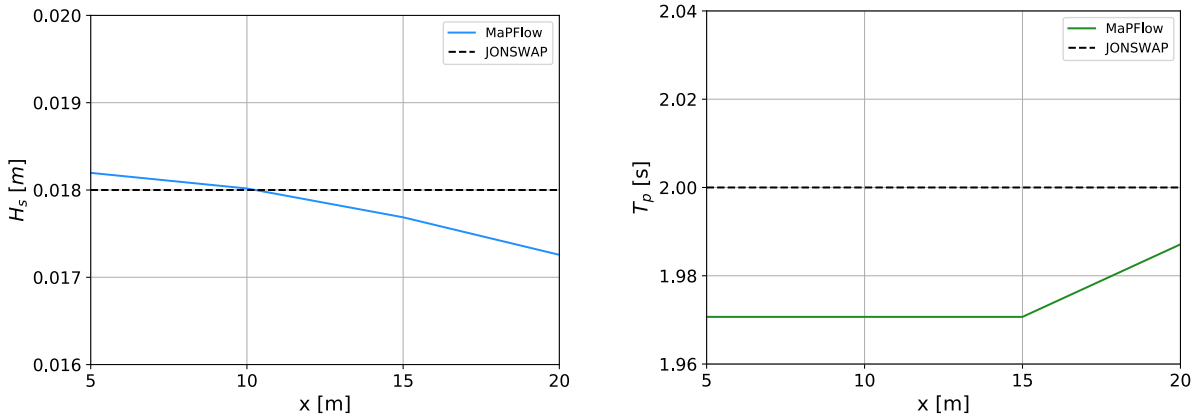

Figure 6.13: Evolution of significant wave height (left) and peak period (right) for a wave component number of $N = 200$

6.4.3 Effect of simulation length

The influence of the simulation length on the obtained results becomes more clear, if someone considers that this duration, coincides with the record length of the spectral estimation process. Hence, longer runtime, will sure provide a more abundant time history, which is necessary in order to derive the desired frequency spectrum. For the purpose of investigating the influence of this parameter, lengths of $75T_p$, $150T_p$ and $250T_p$ are considered, the second of which is not presented here, as it is identical with the case of $N = 100$ in the previous subsection. During the post-processing, the windowing length has been set to be proportional with the simulation length, so as to eliminate differences in the results caused by the parameters of the Welch method.

In Fig. 6.14 and 6.16 the spectral representations, at the different stations of the numerical wave tank and for $L = 75T_p$ and $250T_p$ respectively are illustrated. The corresponding deviations between the simulated significant wave height and peak period with the imported values are shown in Fig. 6.15 and 6.17. Regarding the first case with the shortest duration and hence a limited dataset provided to conduct the spectral estimation, it is clear that the spectrum follows the general trend of JONSWAP, but is subject to a lot of disturbances in the higher frequencies' region. In contrast, for the other case and having under consideration also the results for $L = 150T_p$, it is concluded that the length of the simulation directly affects the success of the Welch method to provide a smooth and accurate spectrum. This conclusion is illustrated also by the evolution of the significant wave height and the peak period, as a gradual convergence to the desired values is observed with the increase of the simulation length.

Thus, it is crucial to make a compromise between computational cost and accuracy, depending on the case under consideration. In the present study, taking into account that the main focus area is the wave transformation and the spectral evolution over variable bathymetry regions, precision is a significant aspect, thus a requirement for long recordings emerges.

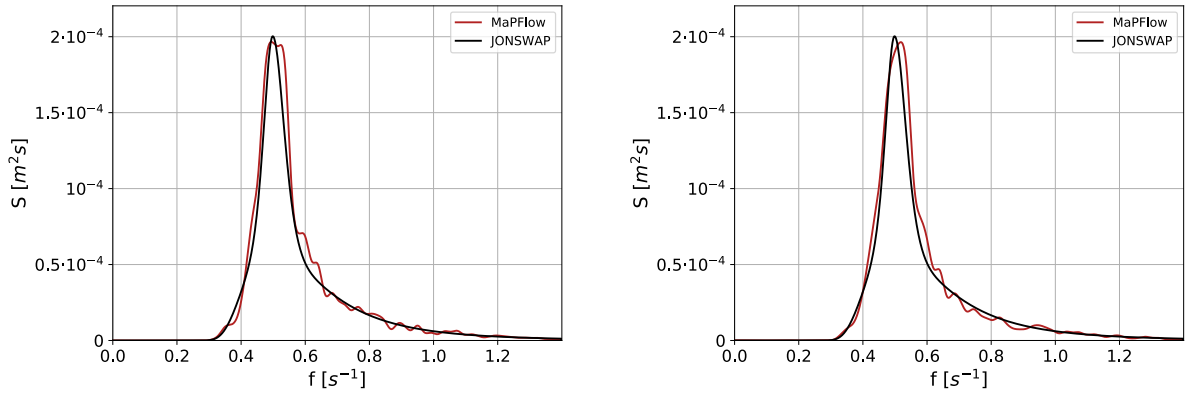

(a) x = 5 m (b) x = 10 m

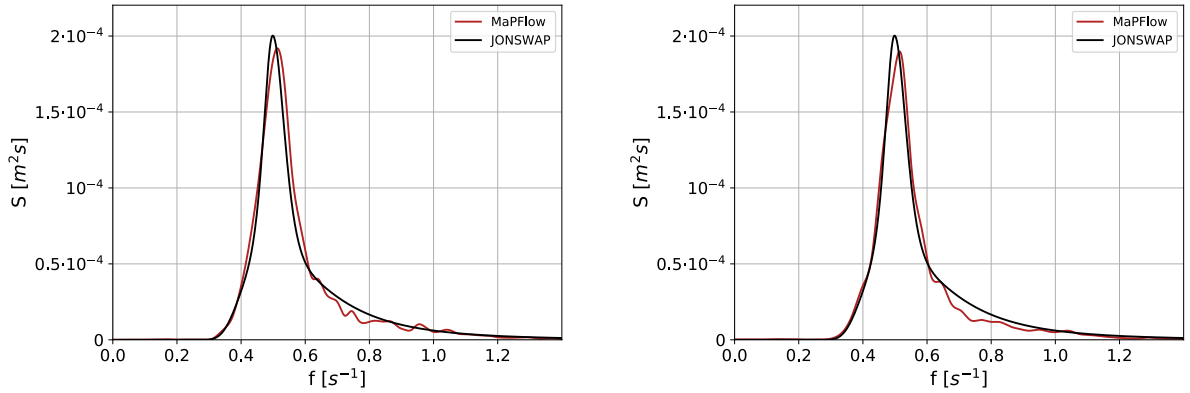

(c) x = 15 m (d) x = 20 m

Figure 6.14: Wave energy density spectra for a simulation length of $75T_p$

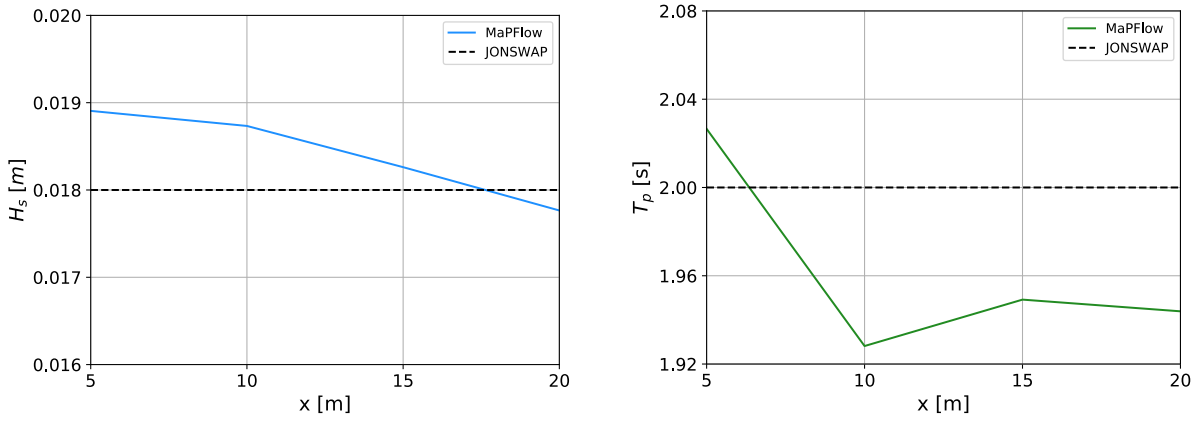

Figure 6.15: Evolution of significant wave height (left) and peak period (right) for a simulation length of $75T_p$

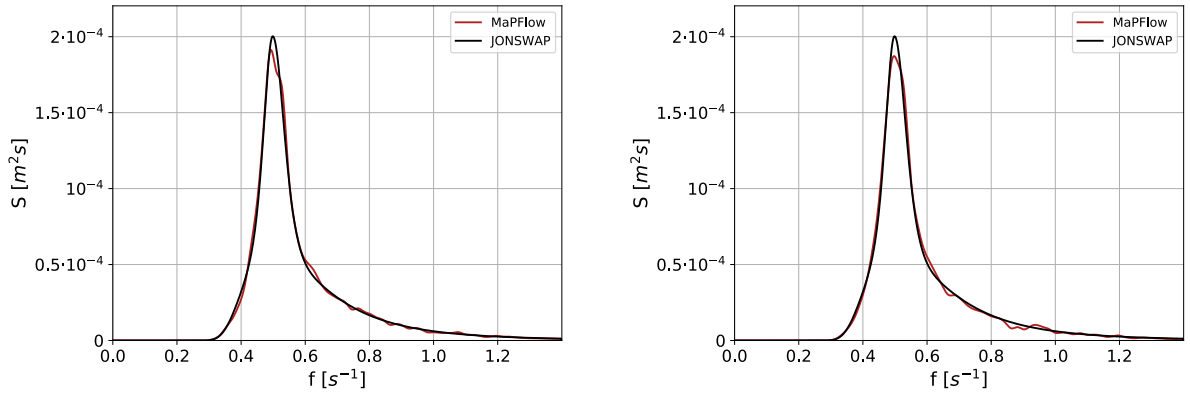

(a) x = 5 m (b) x = 10 m

(c) x = 15 m (d) x = 20 m

Figure 6.16: Wave energy density spectra for a simulation length of $250T_p$

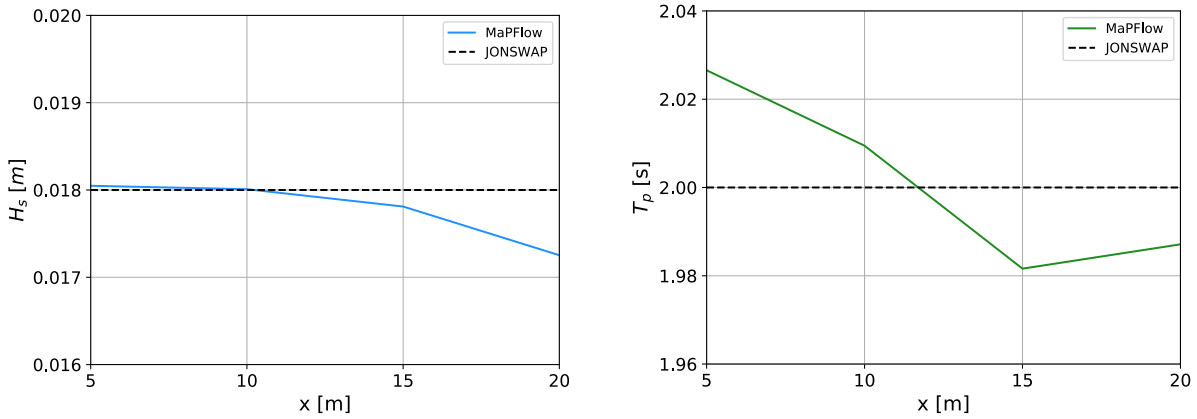

Figure 6.17: Evolution of significant wave height (left) and peak period (right) for a simulation length of $250T_p$

6.5 FSRA Validation

For the validation of the ability of *MaPFlow* to accurately reproduce irregular waves using the Free Surface Reconstruction Algorithm, it was tested for the generation and propagation of a focused wave group. To this end, the numerical model, is compared with the experimental results of Fang & Guo [59]. A similar approach has been examined by Aggarwal et al. [60] for the propagation of breaking irregular waves over a submerged breaker bar.

The configuration of the numerical wave tank that was created for the simulation is shown in Fig. 6.18. The length of the generation and the damping zone correspond as previously prescribed to the maximum wavelength among all the imported wave components, which were set to $N = 100$. The measurements available in the experimental work are provided by a wave gauge at $x = 8\ m$.

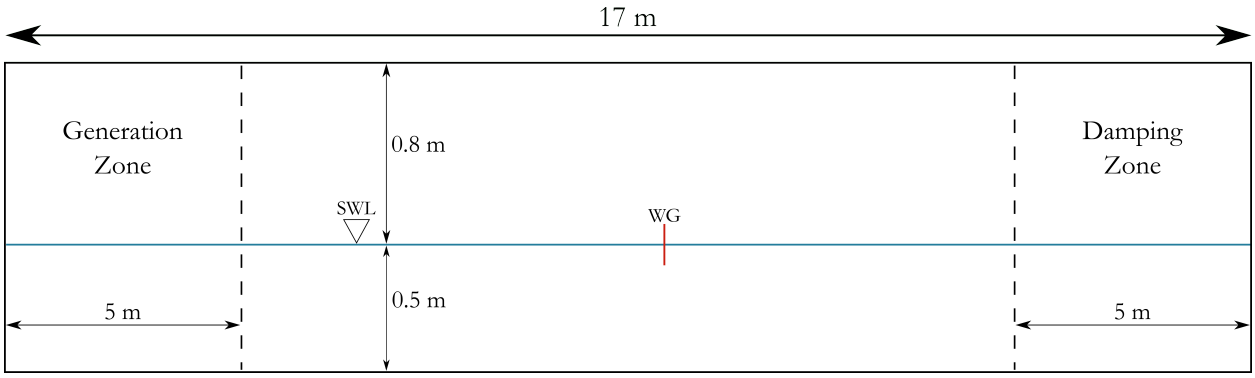

Figure 6.18: Configuration of the numerical wave tank for the focused wave group case

First, the effect of the grid and timestep on the application of the FSRA was examined and the simulation was carried out for the three grid resolutions shown in Table 6.3 and for timestep intervals of $dt = T_p/400, T_p/800, T_p/1600$. The results are presented in Fig. 6.19, in which it is evident that the deviations among the different cases are similar to those of the grid and timestep sensitivity study of the previous section. Thus, it is deduced that the influence of these parameters on the applicability of the FSRA method is of little significance.

	Nodes	dx (m)	Cells per H_s
G1	79000	0.020	20
G2	140000	0.015	30
G3	286000	0.010	38

Table 6.3: Grid resolutions for focused wave propagation case

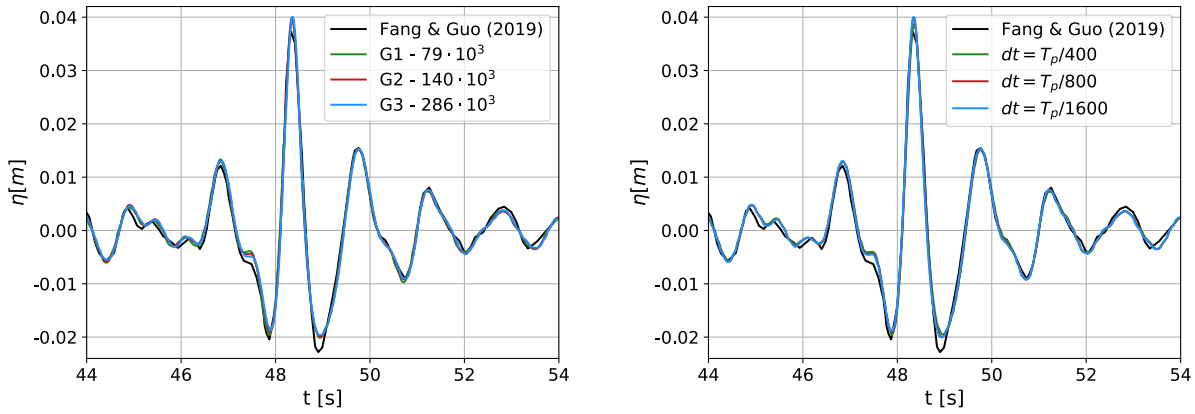

Figure 6.19: Effect of grid (left) and timestep (right) selection on the implementation of the FSRA

The grid resolution $G2$ and the timestep of $dt = T_p/800$ provide results that are both satisfying and computationally affordable, hence it was selected for the conduction of the analysis. Having isolated the influence of the FSRA method on the quality of the results, the total time history is shown in Fig. 6.20. It may be seen that the results are very promising and the free surface is reproduced quite accurately, however a deviation is observed in the extreme crests and troughs, highlighting a defect of the method.

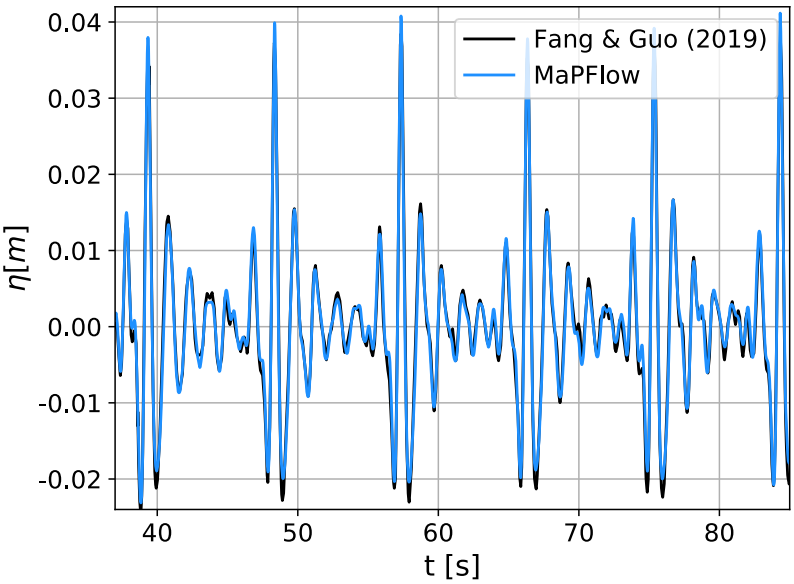

Figure 6.20: Reconstructed free surface elevation time history of the focused wave group against the experimental

Chapter 7

Irregular Wave Propagation Over Regions of Variable Bathymetry

7.1 Propagation Over a Breaker Bar

7.1.1 Numerical Setup

In this section, the numerical model validated above is implemented to study the transformation and spectral evolution of an irregular wave over a submerged breaker bar. A schematic approach of the numerical wave tank is shown in Fig. 7.1, which emulates the physical wave tank of the experimental work of Beji & Battjes [61], against which the numerical results are also compared. The beach that is used in the experiment for the damping of the waves is omitted here, as it is replaced with the forcing zone.

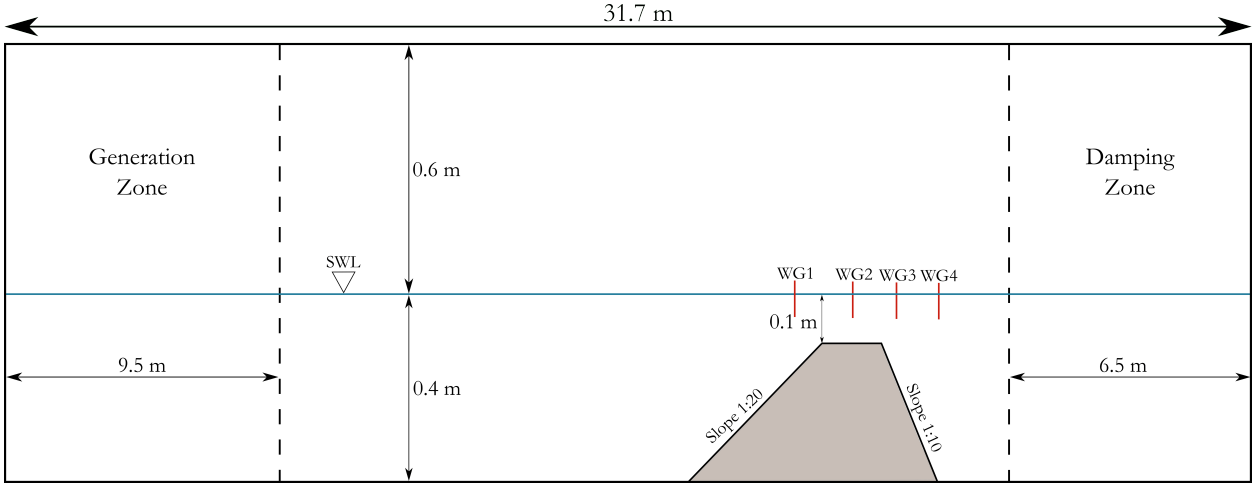

Figure 7.1: Configuration of the numerical wave tank for the case of an irregular wave propagation over a bar

The positions of the wave gauges are chosen to coincide with the experimental gauges for which spectral density results are provided and they are $x_{WG1} = 11\ m$, $x_{WG2} = 13\ m$, $x_{WG3} = 15\ m$ and $x_{WG4} = 17\ m$. Moreover, two different irregular waves are generated with peak period of $T_p = 2.5\ s$ and $T_p = 1\ s$ and signifcant wave heights of $H_s = 0.029\ m$ and $H_s = 0.041\ m$ respectively. Following the terminology of the work of Beji & Battjes, the first wave pattern is characterized as long waves, due to their relatively large wavelength and the second as short waves. In the present case study, shoaling is the main phenomenon under consideration and wave breaking is quite indirect and limited, in terms of occurring only when the crests of several waves are superposed, so as to increase the local water elevation. Hence, by using the conclusions drawn from the grid and timestep sensitivity study of the previous chapter, as well as the one from Ntouras & Papadakis [16] for the regular wave propagation of the same problem, a timestep of $dt = T_p/800$ is selected. Regarding mesh selection, a grid with a uniform cell size in the flat-bottom region of $dx_1 = 0.015\ m$ which becomes denser and reaches $dx_2 = 0.01\ m$ in the region of the bar was created for long waves. However, in order to maintain the philosophy that connects grid properties with the wave features, a much finer mesh was constructed in order to satisfy this condition for the short waves, with the aforementioned cell sizes to be $dx_1 = 0.0085\ m$ and $dx_2 = 0.005\ m$. In the vertical direction, the mesh is relatively dense in the vicinity of the free-surface and it gradually coarsens towards the upper boundary and the lower boundary, while it is also denser in the boundary layer region. The grid sizes for the two wave conditions described above was $335 \cdot 10^3$ and $570 \cdot 10^3$ cells respectively.

Regarding the effect of turbulence, the simulations were carried out for the cases of a Buoyancy Modified $k-\omega$ SST model and Stabilized $k-\omega$ SST model, but little difference in the spectral representations was observed. Thus, considering that the Stabilized $k-\omega$ SST model captures more accurately the turbulent effects and the eddy viscosity, it was chosen for the illustration of the results. The selected reconstruction scheme was HRIC, as in the case of regular breaking waves, due to the fact that BICS was not capable of capturing the abrupt changes of the free surface that occurred in breaking, especially when turbulence was included. Finally, it shall be mentioned that the time history is not matching the one in the experiment due to lack of data for the phase angle distribution, hence the soundness of the results is based on the principle that irregular waves generated from the same spectrum will contain the same amount of energy. The number of generated wave components was $N = 120$, with a frequency interval of $\Delta f \approx 0.0092\ s^{-1}$ and the distribution of the phase angles used in the present analysis is shown in Fig. 7.2.

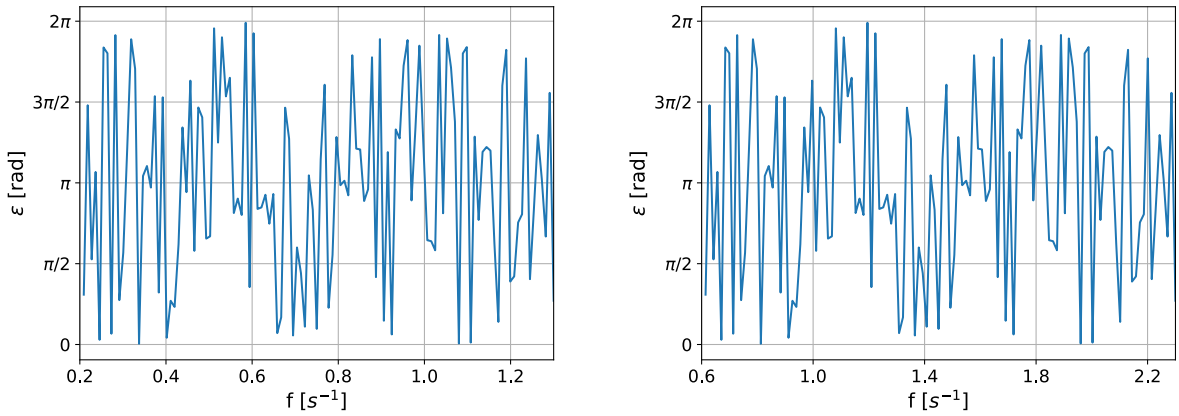

(a) $T_p = 2.5\ s$, $H_s = 0.029\ m$ (b) $T_p = 1.0\ s$, $H_s = 0.041\ m$

Figure 7.2: Phase angle distribution along the range of generated frequency components for the irregular wave propagation over a breaker bar

7.1.2 Results and Discussion

In Fig. 7.3 the normalized energy density spectrum of the simulated long waves in the four stations of interest is presented. The normalization is made so that the area below the spectrum equals to unity and it allows direct comparison between spectra for different wave conditions. Considering that breaking is not widely observed, there is ground to make the assumption that the dissipated energy is negligible and the wave-wave interaction is conservative. In the first gauge, which is located in the upslope side of the bar, the spectral energy has increased due to shoaling and the spectrum has started becoming broader. In the second station, which is located in the horizontal crest of the bar, a decrease in the height of the peak is noticed and higher harmonics have been generated with spectral density spreading towards them, in a way that the total amount of energy is maintained. According to Beji & Battjes, that horizontal region plays a significant role in the transfer of energy to higher harmonics, as it creates a non-dispersive regime for the wave. Hence, that process occurs further in the next station, which is also in the top of the breaker bar, with a quite large portion of energy being distributed to higher frequencies. Finally, in the last gauge, which is located in the downslope side of the bar and the de-shoaling process is dominant, the formation of secondary peaks is observed, while the initial spectral peak further decreases. In that region, wave decomposition takes place, from waves of a certain amplitude into several smaller amplitude waves of similar frequencies and the spectral shape takes its final form, from a narrow-banded to a broad-banded spectrum. From a numerical point of view, this process facilitates the damping of the propagating waves before they reach the boundary of the domain.

The simulated results, are generally in a good agreement with the experimental, thus MaPFlow, seem to capture dispersive and shoaling phenomena for the irregular waves. A

quite significant deviation is depicted in the region of shoaling (in the first subfigure) which is also observed by Aggarwal et al. [14]. A reason for that might be the selected means of spectral density estimation, as Beji & Battjes use a raw FFT to transit from time to frequency domain. Apart from that, the reallocation of the spectral energy to the different frequency ranges is captured accurately and the formation of the secondary peaks is also evident.

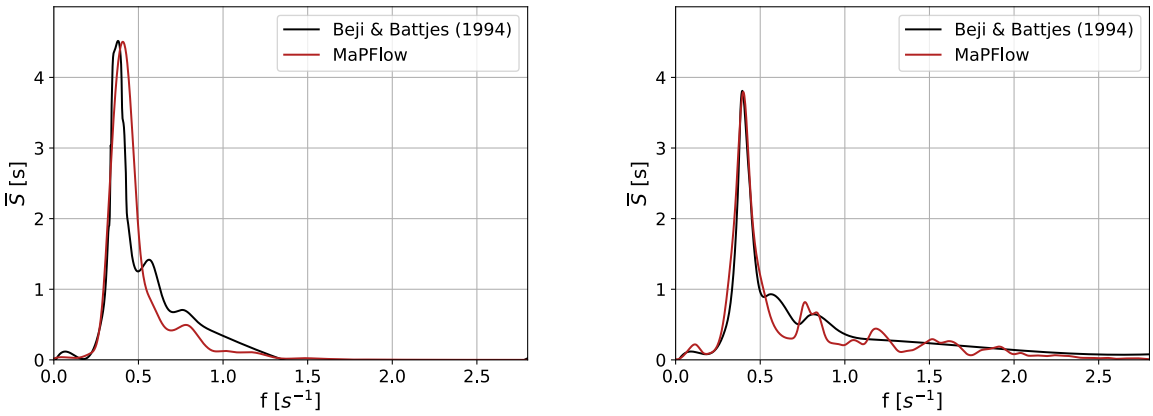

(a) WG1: x = 11 m

(b) WG2: x = 13 m

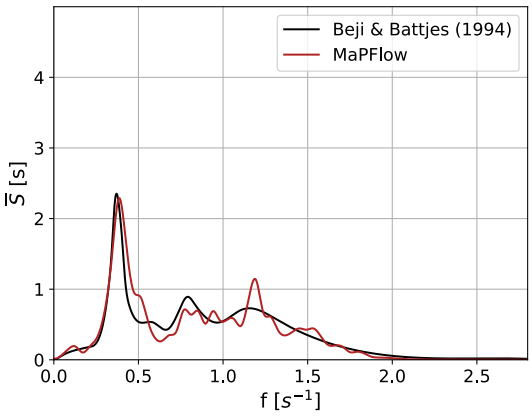

(c) WG3: x = 15 m

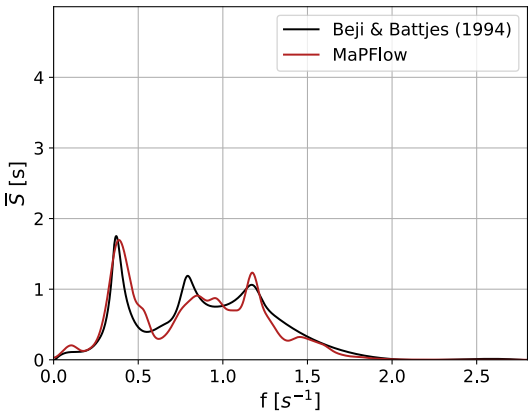

(d) WG1: x = 17 m

Figure 7.3: Normalized wave energy density spectra for the case of irregular wave propagation over a breaker bar for $T_p = 2.50\ s$ and $H_s = 0.029\ m$

In Fig. 7.3 the normalized energy density spectrum of the simulated short waves in the four stations of interest is presented. In contrast with the long waves, the spectral evolution in this case shows shape reformations in a much smaller scale, whereas higher harmonics are not induced on a primary base. This feature is captured well by *MaPFlow* and the numerical spectrum maintains its initial narrow-banded shape, similar to the experimental.

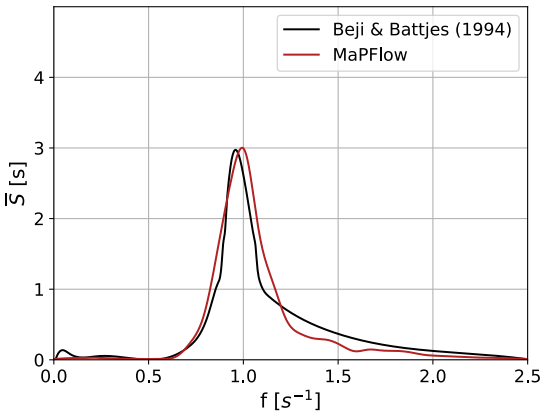

(a) WG1: x = 11 m

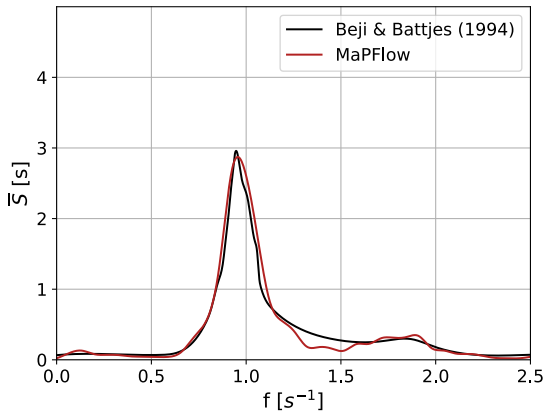

(b) WG2: x = 13 m

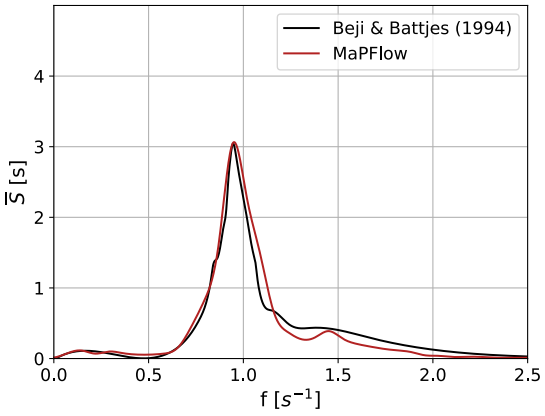

(c) WG3: x = 15 m

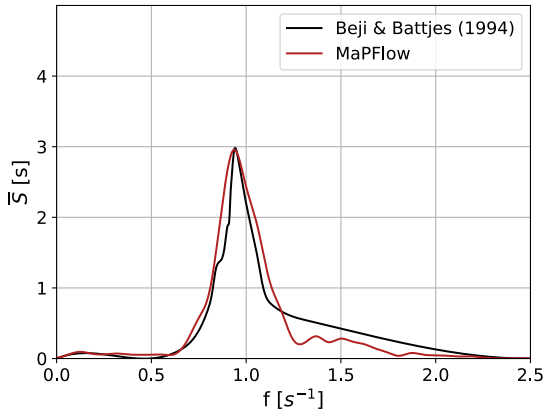

(d) WG1: x = 17 m

Figure 7.4: Normalized wave energy density spectra for the case of irregular wave propagation over a breaker bar for $T_p = 1.0\ s$ and $H_s = 0.041\ m$

Finally, the eddy viscosity for the case of the long and short waves respectively, is presented in Fig. 7.5. Due to the random character of the propagating waves, the evolution of this variable in time is also chaotic and random. However, the success of the Stabilized $k-\omega$ SST model for the simulation of irregular wave shoaling is quite evident by observing that there is no turbulence production in the region before the bar, while the turbulent viscosity tends to fade during the de-shoaling process. This trend is noticed in both cases, however in the short wave simulation, the production of turbulence is limited compared to long waves, which may be explained by the also limited redistribution of spectral energy to adjacent frequencies.

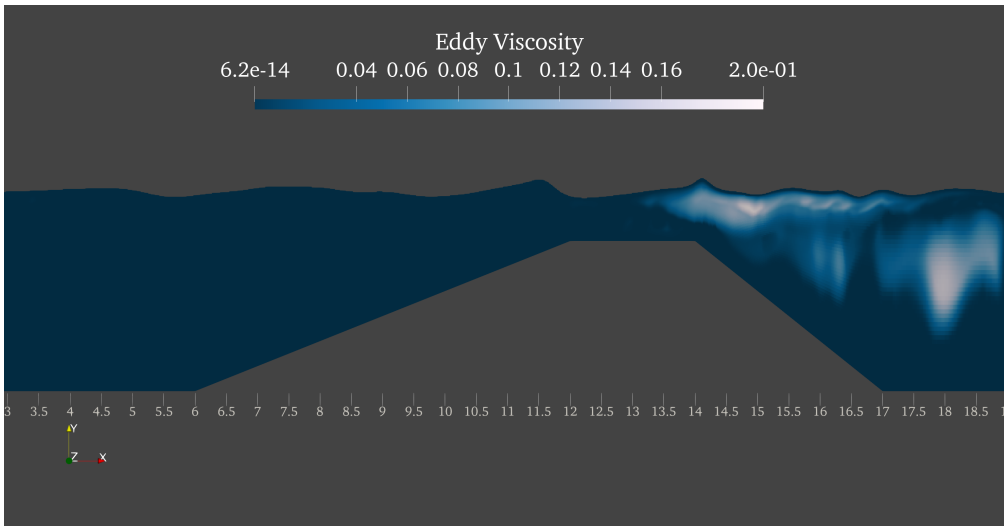

(a) $T_p = 2.5\ s$ and $H_s = 0.029\ m$

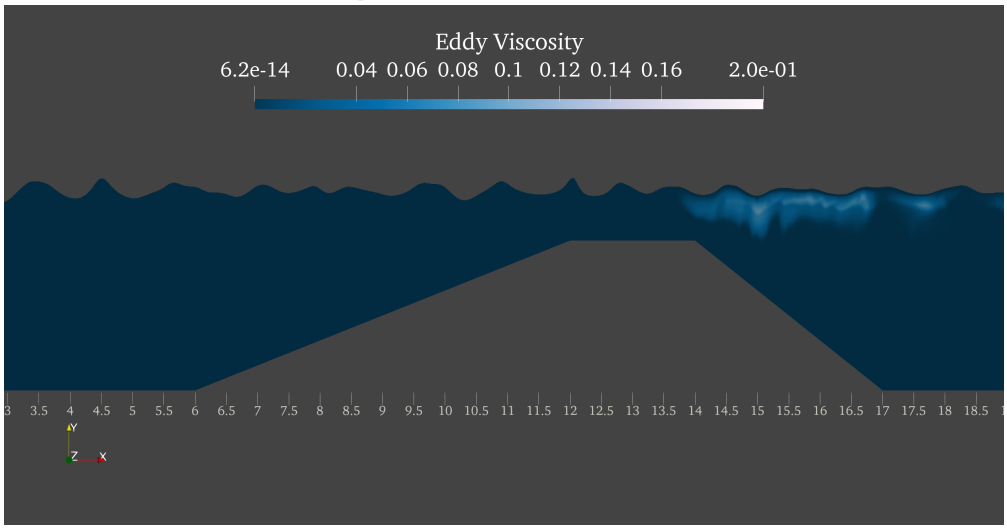

(b) $T_p = 1.0\ s$ and $H_s = 0.041\ m$

Figure 7.5: Snapshots of the eddy viscosity for the case of the submerged breaker bar

7.2 Propagation Over a Sloped Bottom

7.2.1 Numerical Setup

The analysis of the previous section has been conducted using an arbitrary phase angle distribution and the soundness of the comparison of the results is derived from the fact that both the experimental and numerical irregular waves have been generated according to the same exact spectrum. On the contrary, in this section, the Free Surface Reconstruction Algorithm is used, in order to attempt to reproduce the exact free-surface time history of the experiments of Adytia et al. [62] and assess whether the numerical results are in accordance with the experimental wave transformation. The numerical wave tank under considerations is presented in Fig. 7.6 and the wave spectrum is of JONSWAP-type with a peak period of $T_p = 2.5\ s$ and a significant wave height of $H_s = 0.2\ m$. The locations of the wave gauges are identical with the experimental stations at $x_{WG1} = 13.65\ m$, $x_{WG2} = 21.98\ m$ and $x_{WG3} = 24\ m$.

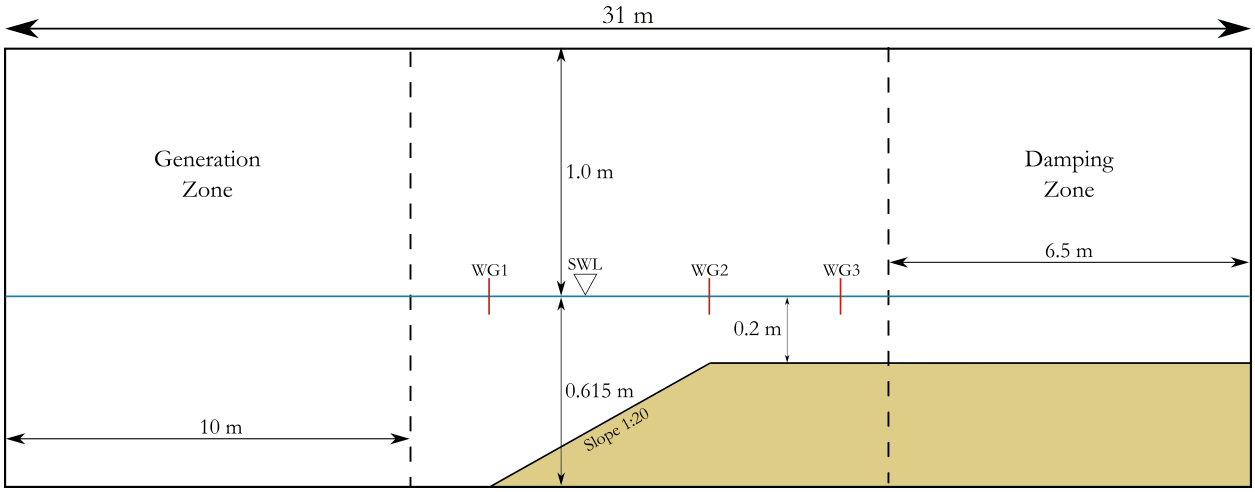

Figure 7.6: Configuration of the numerical wave tank for the case of an irregular wave propagation over a sloped bottom

In this case, the breaking is much more strong than the previous, since the ratio of the significant wave height to the depth at the most shallow point is $H_s/d = 1$. Thus, the starting point of the analysis consists of a grid and timestep independence study. Three grid resolutions of ascending order of refinement were examined, the features of which are shown in Table 7.1. The term dx_1 denotes the uniform cell size in the x-direction in the area of the incident spectrum, where the depth is equal to $0.615\ m$, while dx_2 is the cell size in the flat region after the slope.

In Fig. 7.7 the free-surface elevation at the three stations and for the three studied mesh resolutions is presented, in comparison with the corresponding experimental elevation. The simulations were conducted with a timestep of $dt = T_p/2000$ and the Buoyancy Modified

	Nodes	Cells per H_s	dx_1 (m)	dx_2 (m)
G1	140000	18	0.03	0.02
G2	240000	28	0.02	0.01
G3	356000	34	0.015	0.075

Table 7.1: Grid resolutions for the case of irregular wave propagation over sloped bottom

$k-\omega$ SST model was used for the turbulence closure. In the first gauge, where the incident wave spectrum is depicted, the differences between the three cases is negligible. In the other two gauges, the effect of the grid refinement becomes more perceivable, with $G3$ giving the best result, with little difference however from $G2$.

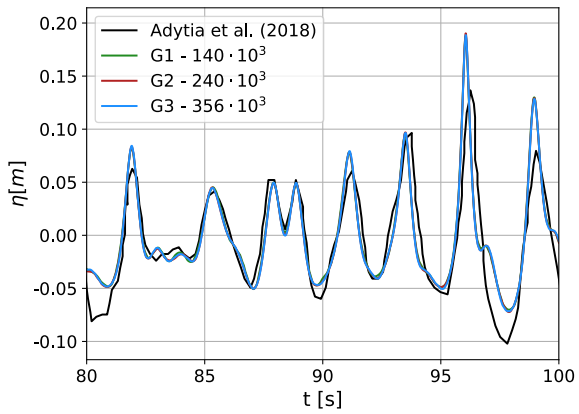

(a) WG1: x = 13.65 m

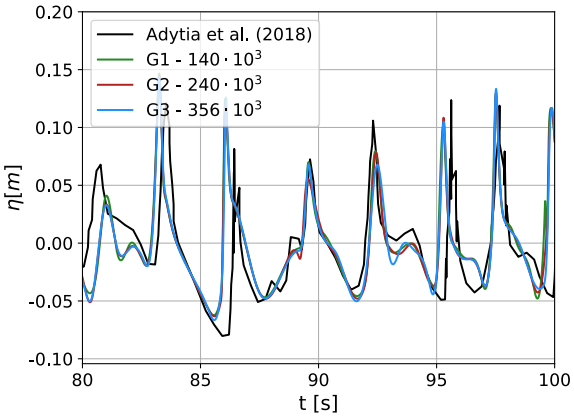

(b) WG2: x = 21.98 m

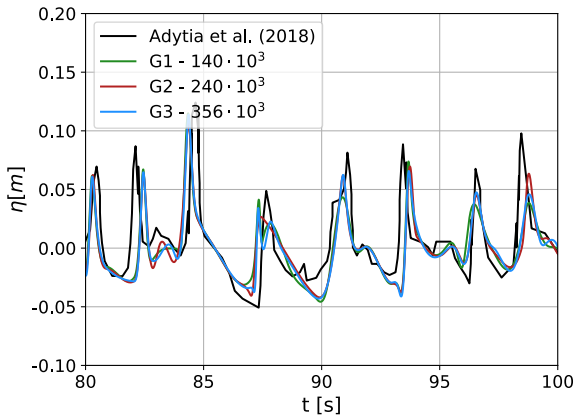

(c) WG3: x = 24 m

Figure 7.7: Reconstructed free-surface elevation profiles for grid resolutions $G1, G2, G3$

For the grid resolution case $G2$ and the same solver settings as above, the simulation was carried out for the timesteps $dt = T_p/1000, T_p/4000$, the results of which are shown in

Fig. 7.8. Again, in the first station the deviation between the three simulations is negligible, which was expected considering that it illustrates the time history of the incident spectrum. In the other two gauges, a growth is observed in the differences between the three cases, with the case of $dt = T_p/2000$ raising the level of accuracy significantly, in comparison with $dt = T_p/4000$.

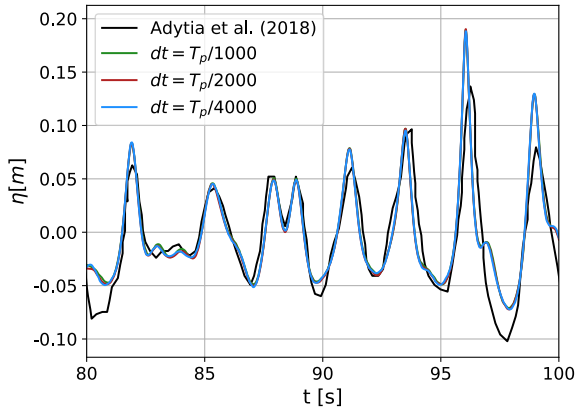

(a) WG1: x = 13.65 m

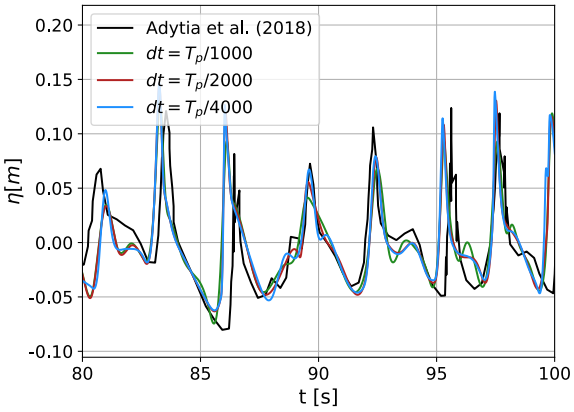

(b) WG2: x = 21.98 m

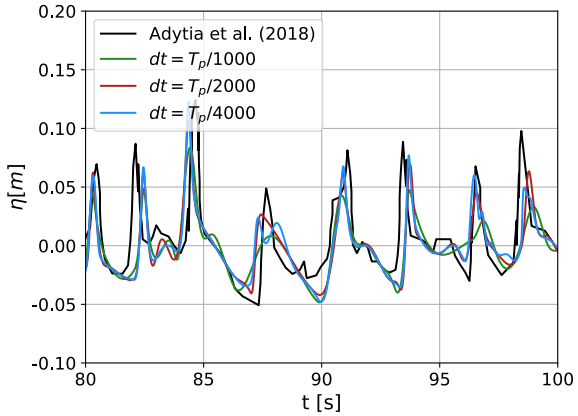

(c) WG3: x = 24 m

Figure 7.8: Reconstructed free-surface elevation profiles for $dt = T_p/1000, T_p/2000, T_p/4000$

Thus, the analysis that follows is conducted using the grid resolution $G2$ and a timestep of $dt = T_p/2000$. Again, both the Buoyancy Modified $k-\omega$ SST model and the Stabilized $k-\omega$ SST model were tested and the discrepancies between the two of them were rather insignificant. As in the previous case, due to more effective representation of the eddy viscosity and turbulent kinetic energy field, the Stabilized model is chosen for the illustration of the final results. The reconstruction scheme is HRIC for the reasons mentioned in the previous test case. The number of generated wave components is $N = 100$, with a frequency interval of $\Delta f \approx 0.011 s^{-1}$.

7.2.2 Results and Discussion

In Fig. 7.9 the reproduced free surface elevation history for the three stations is presented against the experimental. The first subfigure corresponds to the location where the slope begins and contains the time history used for the free surface reconstruction. The accuracy of the reconstruction is quite satisfactory, however several discrepancies are observed again in the troughs and crests. In the second and third subfigures the wave transformation and breaking are depicted and the results are very promising. If someone considers the inherent error of the FSRA method, it is evident that the wave's transformation due to shoaling and eventually breaking, follows the general trend of the experimental, despite this relative error. The fact that the elevations follow the periodic profile of the experimental irregular wave, highlights the ability of *MaPFlow* in capturing the dispersive phenomena of the problem.

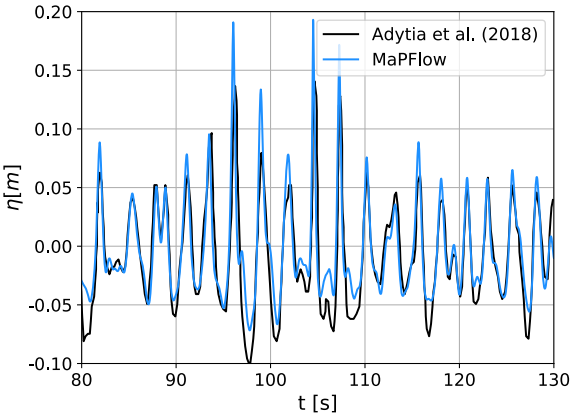

(a) WG1: x = 13.65 m

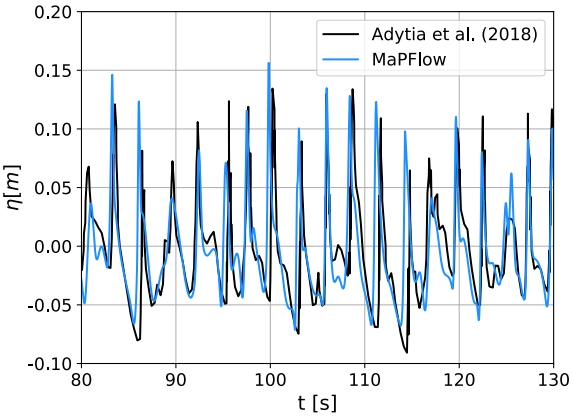

(b) WG2: x = 21.98 m

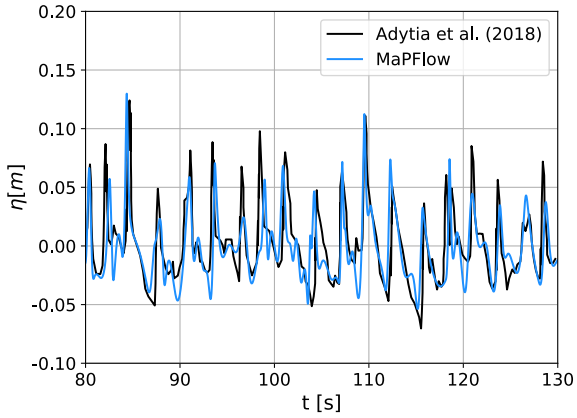

(c) WG3: x = 24 m

Figure 7.9: Reconstructed free-surface elevation profiles for the case of irregular wave propagation over a sloped bottom

In Fig. 7.10 the spectral evolution of the reconstructed irregular wave along the three stations and in normalized form is presented. In the first gauge, where the incident spectrum is illustrated, apart from the primary peak at the respective frequency, a spread of energy in higher frequencies is observed. In the numerical spectrum, the formation of a secondary peak is also observed, which also exists in the experimental, but in a smaller scale. This is probably caused by the effect of the seabed on the propagation of the irregular waves, since the significant wave height is relatively large compared to the still water depth. In contrast with the previous case, where essentially non-breaking waves were considered, an appreciable portion of energy is lost here due to breaking. This fact can be graphically evaluated by the significant reduction of the area under the spectrum between the second and first gauges. In the last station, which is in the flat bottom area after the slope, further reduction of the wave energy is observed due to the strong interaction of the wave with the seabed topography, as prescribed by shallow water dynamics.

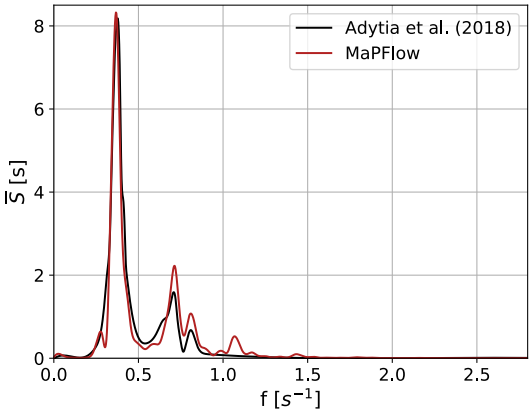

(a) WG1: x = 13.65 m

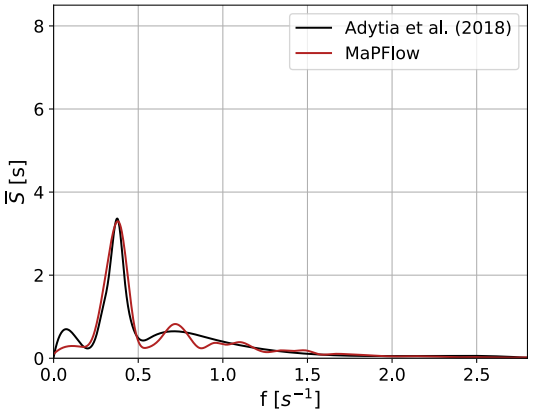

(b) WG2: x = 21.98 m

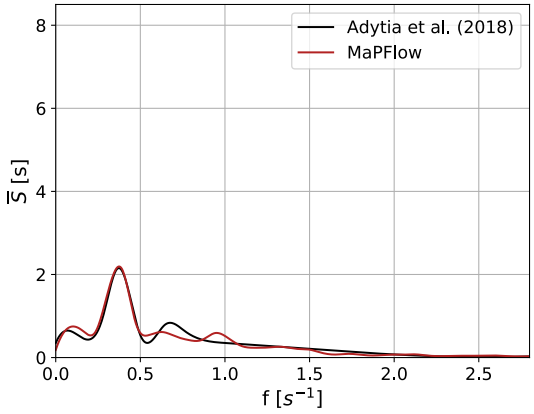

(c) WG3: x = 24 m

Figure 7.10: Normalized wave energy density spectra for the case of irregular wave propagation over a sloped bottom

In Fig. 7.11 snapshots of the eddy viscosity in the region of the slope for a formed plunging wave before breaking, as well as for a post-breaking field are presented. The effect of the stabilization technique is also evident here and can be extended to the case of irregular wave breaking. In particular, in the region where the wave propagates without deformations, no turbulence production is observed, whereas it is mostly generated after the end of the slope where the breaking tends to occur and the surfzone is formed.

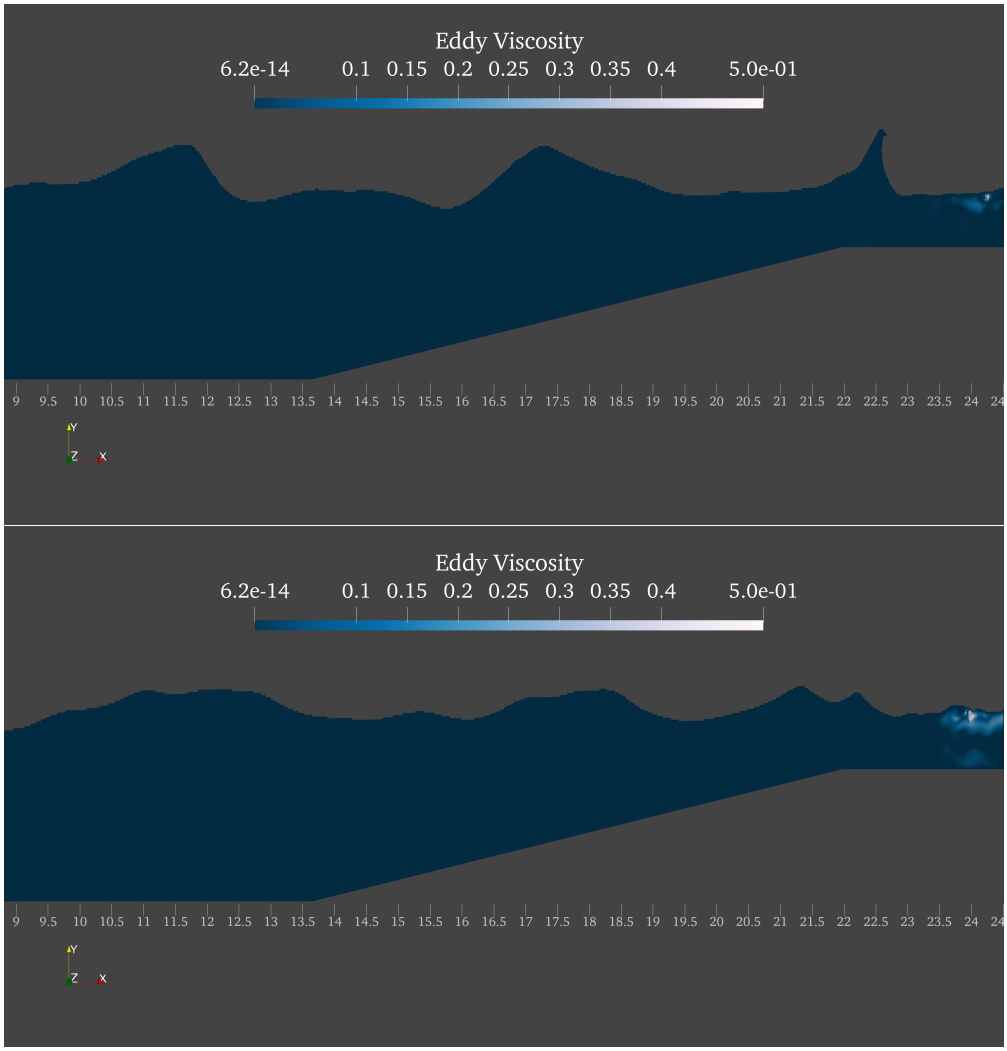

Figure 7.11: Snapshots of the eddy viscosity for the case of the sloped bottom

Chapter 8

Conclusions and Recommendations for Future Research

The intention and purpose of this thesis was twofold. First, the focus was put on the successful implementation of a RANS numerical model coupled with an artificial compressibility method, in an attempt to investigate complex free surface flows, such as wave breaking. A presupposition for this was the study of the propagation of a steep wave over flat bottom, in order to determine the settings of the solver and the numerical wave tank. Secondly, a framework for the efficient and accurate generation and propagation of irregular waves from a given energy density spectrum was developed. In the context of this work, only the JONSWAP spectrum was used, but the parametric analysis presented, not only provides an insight about the solver settings regarding irregular waves by taking into account the forthcoming spectral density estimation, but also allows the extension to any narrow-banded spectrum.

After the above two purposes of the study have been fulfilled, the combination of the two areas was put under the spotlight. Beginning with the investigation of the spectral evolution of a JONSWAP-type spectrum over a submerged breaker bar, the ability of *MaPFlow* to capture dispersive and shoaling phenomena was validated. Following, in an attempt to be capable of comparing free-surface elevation profiles with experimental results, the Free Surface Reconstruction Algorithm was implemented. The validation context of this endeavour was the generation and propagation of a focused wave group over a flat seabed. Finally, this method was applied for the investigation of the irregular wave propagation over a sloped bottom, where *MaPFlow* provided quite promising results for the shoaling, as well as the breaking of the waves.

The area of regular wave breaking without the interference of structures has been covered so far, as well as the irregular wave propagation, shoaling and breaking. Hereby, some recommendations about the different trails that future research on this subject could follow are presented. First of all, as discussed in the relevant part, the effect of turbulence in wave breaking is of three-dimensional nature. Hence, an investigation of the influence of the available turbulence models, in the context of the three-dimensional problem might be an

interesting continuation point. Moreover, considering that the impact of breaking waves on marine structures is of crucial importance for ocean and coastal engineering applications, the analysis of wave-structure interaction using *MaPFlow* and the investigation of the complex turbulent regime that is induced by that interference, is also an option. Apart from those research trails, one of higher computational cost would be to conduct LES for the analysis of wave breaking. On what concerns irregular waves, the first step for further research is to examine the capabilities of *MaPFlow* in fluid-structure interaction, which gives ground for various marine applications, such as the study of the resistance and stability of floating bodies. Finally, the three-dimensional simulation of irregular waves has far more interest aspects than the two-dimensional, since it allows the numerical modelling and analysis of multi-directional sea states, expressed as the product of a frequency and a directional spectral component.

List of Figures

List of Tables

Nomenclature

ACM Artificial Compressibility Method

BICS Blended Interface Capturing Scheme

CFD Computational Fluid Dynamics

CICSAM Compressive Interface Capturing Scheme for Arbitrary Meshes

DNS Direct Numerical Simulation

HRICS High Resolution Interface Capturing Scheme

LES Large Eddy Simulation

MGDS Modified Gamma Discretization Scheme

NTUA National Technical University of Athens

NWT Numerical Wave Tank

PLR Piecewise Linear Reconstruction

RANS Raynolds-Averaged Navier-Stokes

STACS Switching Technique for Advection and Capturing of Surface

TKE Turbulent Kinetic Energy

VOF Volume of Fluid

Bibliography

[1] P. Lin and P. L. Liu. A numerical study of breaking waves in the surf zone. *J. Fluid Mech.*, 359:239–264, 1998.

[2] S. F. Bradford. Numerical simulation of surf zone dynamics. *J. Waterw. Port Coast. Ocean Eng.*, 126:1–13, 2000.

[3] S. Mayer and P. A. Madsen. Simulation of breaking waves in the surf zone using a Navier-Stokes solver. *Coastal Eng.*, pages 928–941, 2000.

[4] A. M. Chella. *Breaking Wave Characteristics and Breaking Wave Forces on Slender Cylinders*. PhD thesis, Norwegian University of Science and Technology, 2016.

[5] S. Brown, D. Greaves, V. Magar, and D. Conley. Evaluation of turbulence closure models under spilling and plunging breakers in the surf zone. *Coastal Eng.*, 114:177–193, 2016.

[6] B. Devolder, P. Troch, and P. Rauwoens. Application of a buoyancy-modified k-ω SST turbulence model to simulate wave run-up around a monopile subjected to regular waves using OpenFOAM®. *Coastal Eng.*, 125:81–94, 2017.

[7] B. E. Larsen and D. R. Fuhrman. On the over-production of turbulence beneath surface waves in Reynolds-averaged Navier Stokes models. *J. Fluid Mech.*, 853:419–460, 2018.

[8] S. Liu, M. Chen Ong, C. Obhrai, I. Gatin, and V. Vukcevic. Influences of free surface jump conditions and different k-ω SST turbulence models on breaking wave modelling. *Ocean Eng.*, 217, 2020.

[9] V. Vukcevic, H. Jasak, and I. Gatin. Implementation of the Ghost Fluid Method for free surface flows in polyhedral Finite Volume framewor. *Computers and Fluids*, 153:1–19, 2017.

[10] P. D. Hieu, T. Katsutoshi, and V. T. Ca. Numerical simulation of breaking waves using a two-phase flow model. *Appl. Math. Model.*, 28:983–1005, 2004.

[11] E. D. Christiansen. Large eddy simulation of spilling and plunging breakers. *Coast. Eng.*, 53:463–485, 2006.

[12] S. Aggarwal, A. M. Chella, H. Bihs, and D. Myrhaug. Properties of breaking irregular waves over slopes. *Ocean Eng.*, 216, 2020.

[13] S. Aggarwal, A. M. Chella, H. Bihs, and D. Myrhaug. Characteristics of breaking irregular wave forces on a monopile. *Appl. Ocean Res.*, 90, 2019.

[14] S. Aggarwal, A. M. Chella, H. Bihs, and A. Kamath. Numerical investigation of breaking irregular waves over a submerged bar with CFD. In *Coastal Engineering Conference*, volume 36, 2018.

[15] I. Gatin, V. Vukcevic, and H. Jasak. A framework for efficient irregular wave simulations using Higher Order Spectral method coupled with viscous two phase model. *J. Ocean Eng. Sci.*, 2017.

[16] G. Papadakis and D. Ntouras. A coupled artificial compressibility method for free surface flows. *J. Mar. Sci. Eng*, 8(8), 2020.

[17] I. A. Svedsen. *Introduction to nearshore hydrodynamics.* World Scientific Publishing, 2005.

[18] C. J. Galvin. Breaker type classification on three laboratory beaches. *J. Geophys. Res.*, 73:3651–3659, 1968.

[19] S. Massel. *Hydrodynamics of Coastal Zones.* Elsevier Science Publishers B.V., 1989.

[20] S. L. Douglass and B. M. Webb. *Highways in the Coastal Environment: Hydraulic Engineering Circular Number 25.* 2020.

[21] C. R. Iribarren and C. Nogales. Protection des ports. In *XVIIth International Navigation Congress*, pages 31–80, 1949.

[22] J. A. Battjes. Surf similarity. In *Coastal Engineering Proceedings*, pages 466–480, 1974.

[23] G. Papadakis. *Development of a hybrid compressible vortex particle method and application to external problems including helicopter flows.* PhD thesis, National Technical University of Athens, 2014.

[24] C. Hirt and B. Nichols. Volume of Fluid (VOF) Method for dynamics of free boundaries. *J. Comput. Phys.*, 39:201–225, 1981.

[25] H. Rusche. *Computational fluid dynamics of dispersed two-phase flows at high phase fractions.* PhD thesis, University of London, 2002.

[26] S. V. Patankar and D. B. Spalding. A calculation procedure for heat, mass and momentum transfer in three-dimensional parabolic flows. *Int. J. Heat Mass Transf.*, 15:1787–1806, 1972.

[27] R. I. Issa, A. D. Gosman, and A. P. Watkings. The computation of compressible and incompressible recirculating flows by a non-iterative implicit scheme. *J. Comput. Phys*, 62:66–82, 1986.

[28] A. J. Chorin. A numerical method for solving incompressible viscous flow problems. *J. Comput. Phys.*, 135:118–125, 1967.

[29] R. F. Kunz, D. A. Boger, D. R Stinebring, T. S. Chyczewski, J. W. Lindau, H. J. Gibeling, S. Venkateswaran, and T. R. Govindan. A preconditioned Navier-Stokes method for two-phase flows with application to cavitation prediction. *Computat. Fluids*, 29:849–875, 2000.

[30] P. Quetey and M. Visonneau. An interface capturing method for free-surface hydrodynamic flows. *Computers and Fluids*, 36:1481–1510, 2007.

[31] F. Moukalled, L. Mangani, and M. Darwish. *The Finite Volume Method in Computational Fluid Dynamics: An Advanced Introduction with OpenFOAM®*. 2015.

[32] V Venkatakrishnan. On the accuracy of limiters and convergence to steady state solutions. *AIAA paper 93-0880*, 1993.

[33] B. P. Leonard. Simple high accuracy resolution program for convective modelling of discontinuities. *Int. J. Numer. Meth. Fluids*, 8:1291–1318, 1988.

[34] S. Muzaferija and M. Peric. Computation of free-surface flows using interface tracking and interface capturing methods. In *Non linear water waves interaction*, pages 59–100, 1999.

[35] O. Ubbink. *Numerical prediction of two fluid systems with sharp interfaces*. PhD thesis, Imperial College of Science, 1997.

[36] B. P. Leonard and H. S. Niknafs. Sharp monotonic resolution of discontinuities without clipping of narrow extrema. *Computers and Fluids*, 19:141–154, 1991.

[37] B. P. Leonard. The ULTIMATE conservative difference scheme applied to unsteady one-dimensional advection. *Computat. Methods Appl. Mech. Eng.*, 88:17–74, 1991.

[38] M. Darwish and F. Moukalled. Convective schemes for capturing interfaces of free-surface flows on unstructured grids. *Numer. Heat Transf. B*, 49, 2006.

[39] M. Darwish. New High-Resolution Scheme based on the Normalized Variable Formulation. *Numer. Heat Transf. B*, 24:353–373, 1993.

[40] J. Wackers, B. Koren, H. C. Rave, A. van der Ploeg, A. R. Starke, B. Deng, P. Quetey, M. Visonneau, T. Hino, and K. Ohashi. Free-surface viscous flow solution methods for ship hydrodynamics. *Arch. Comput. Methods Eng.*, 18:1–41, 2011.

[41] H. Jasak and H. G. Weller. Interface tracking capabilities of the inter-gamma differencing scheme. Technical report, Mechanical Engineering Department, Imperial College of Science, 1995.

[42] H. Jasak. *Error analysis and estimation for the finite volume method with applications to fluid flows*. PhD thesis, University of London, 1996.

[43] P. L. Roe. Approximate riemann solvers, parameter vectors and difference schemes. *J. Comput. Phys.*, 43:357–372, 1981.

[44] R. Biedron, V. Vatsa, and H. Atkings. Simulation of unsteady flows using an unstructured Navier-Stokes solver on moving and stationary grids. In *Proceedings of the 23rd AIAA Applied Aerodynamics Conference*, pages 1–17, 2005.

[45] H. T. Ahn and Y. Kallinderis. Strongly coupled flow/structure interaction with a geometrically conservative ALE scheme on general hybrid meshes. *J. Comput. Phys*, 219:671–696, 2006.

[46] F. R. Menter. Two-equation eddy viscosity turbulence models for engineering applications. *AIAA J.*, 32:1598–1605, 1994.

[47] B. Devolder, P. Troch, and P. Rauwoens. Performance of a buoyancy-modified k-ω and k-ω SST turbulence model for simulating wave breaking under regular waves using openfoam®. *Coastal Eng.*, 138(3), 2018.

[48] C. Windt, J. Davidson, P. Schmitt, and J. V. Ringwood. On the assessment of numerical wave makers in CFD simulations. *J. Mar. Sci. Eng*, 7, 2019.

[49] A. M. Miquel, A. Kamath, M. A. Chella, R. Archetti, and H. Bihs. Analysis of different methods for wave generation and absorption in CFD-based numerical wave tank. *J. Mar. Sci. Eng*, 6, 2018.

[50] N. G. Jacobsen, D. R. Fuhrman, and J. Fredsoe. A wave generation toolbox for the open-source CFD library: OpenFOAM®. *Int. J. Numer. Meth. Fluids*, 70(9), 2011.

[51] N. Newmann, J. *Marine hydrodynamics*. The MIT Press, 1977.

[52] J. D. Fenton. The numerical solution of steady water wave problems. *Computers and Geosciences*, 14(3), 1988.

[53] M. M. Rienecker and J. D. Fenton. A Fourier approximation method for steady water waves. *J. Fluid Mech.*, 104:119–137, 1981.

[54] F. C. K. Ting and J. T. Kirby. Observation of undertow and turbulence in a laboratory surf zone. *Coastal Eng.*, 24, 1994.

[55] Y. Goda. *Random seas and design of maritime structures*. World Scientific, 1985.

[56] K. Hasselmann, T.P. Barnett, E. Bouws, H. Carlson, D.E. Cartwright, K. Enke, J.A. Ewing, H. Gienapp, D.E. Hasselmann, P. Kruseman, A. Meerburg, P. Mller, D.J. Olbers, K. Richter, W. Sell, , and H. Walden. Measurements of wind-wave growth and swell decay during the Joint North Sea Wave Project (JONSWAP). *Ergänzung zur Deut. Hydrogr. Z*, 12, 1973.

[57] P. D. Welch. The use of fast fourier transform for the estimation of power spectra: A method based on time averaging over short, modified periodograms. *IEEE trans. audio electroacoust.*, 17, 1967.

[58] S. T. Grilli, C. A. Guerin, and B. Goldstein. Ocean wave reconstruction algorithms based on spatio-temporal data acquired by a flash LIDAR camera. In *International Offshore and Polar Engineering Conference*, 2011.

[59] Q. Fang and A. Guo. Analytical and experimental study of focused wave action on a partially immersed box. *Math. Probl. Eng.*, 2019.

[60] A. Aggarwal, C. Pakozdi, D. Bihs, H. abd Myrhaug, and M. A. Chella. Free surface reconstruction for phase accurate irregular wave generation. *J. Mar. Sci. Eng*, 2018.

[61] S. Beji and J.A. Battjes. Experimental investigation of wave propagation over a bar. *Coastal Eng.*, 19, 1993.

[62] D. Adytia, S. Husrin, and Adiwijaya. Numerical simulation of breaking regular and irregular wave propagation above a sloping bottom. *J Phys Conf Ser 1090:012065*, 2018.